Targeting Liver Epsins Ameliorates Dyslipidemia in Atherosclerosis through Inhibition of Proprotein Convertase Subtilisin/Kexin Type 9-Mediated Low-density Lipoprotein Receptor Degradation

Bo Zhu[1#], Krishan Gupta[2#], Kui Cui[1#], Beibei Wang[1], Marina V. Malovichko[4], Kathryn Li[1], Hao Wu[1], Kulandai Samy Arulsamy[2], Bandana Singh[1], Jianing Gao[1], Scott Wong[1], Patricia G Yancey[6], Douglas B. Cowan[1], Da-Zhi Wang[4], Sudha Biddinger[5], MacRae F. Linton[6], Wenyi Wei[7], Sanjay Srivastava[3], Chris A. Bashur[8], Changcheng Zhou[9], Kaifu Chen[2*], Hong Chen[1*]

[1] Vascular Biology Program, Boston Children's Hospital, Department of Surgery, Harvard Medical School, Boston, MA
[2] Department of Cardiology, Boston Children's Hospital, Harvard Medical School, Boston, MA
[3] Department of Medicine, Division of Cardiovascular Medicine, University of Louisville, Louisville, KY
[4] Center for Regenerative Medicine, USF Health Heart Institute, University of South Florida, Tampa, FL
[5] Division of Endocrinology, Boston Children's Hospital, Harvard Medical School, Boston, MA
[6] Division of Cardiovascular Medicine, Department of Medicine, Vanderbilt University Medical Center, Nashville, TN

[7] Department of Pathology, Beth Israel Deaconess Medical Center, Harvard Medical School, Boston, MA

[8] Department of Biomedical and Chemical Engineering and Sciences, Florida Institute of Technology, Melbourne, FL

[9] Division of Biomedical Sciences, School of Medicine, University of California, Riverside, CA

* Correspondence: Hong Chen, Ph.D., Vascular Biology Program, 1 Blackfan Circle, Karp 12214, Mailstop: 3137, Boston, MA 02115. E-mail: hong.chen@childrens.harvard.edu

# These authors contributed equally.

Key Words: Low-density lipoprotein receptor, low-density lipoprotein cholesterol, proprotein convertase subtilisin/kexin type 9, epsins, single-cell RNA sequencing, atherosclerosis.

ABSTRACT

Background:

The low-density lipoprotein receptor (LDLR) in the liver plays a crucial role in clearing low-density lipoprotein cholesterol (LDL-C) from the bloodstream. This process takes place mainly in the liver. Under atherogenic conditions, Proprotein Convertase Subtilisin/Kexin Type 9 (PCSK9), secreted by the liver, binds to LDLR on hepatocytes, preventing its recycling and enhancing its lysosomal degradation. This process reduces LDL-C clearance, promoting hypercholesterolemia. Epsins, a family of ubiquitin-binding endocytic adaptors, are key regulators of atherogenesis in lesional cells, including endothelial cells and macrophages. Given epsins' canonical role in regulating endocytosis of cell surface receptors, we aimed to determine whether and how liver epsins contribute to PCSK9-mediated LDLR endocytosis and degradation, thereby impairing LDL-C clearance and accelerating atherosclerosis.

Methods:

Liver-specific epsin knockout (Liver-DKO) atherosclerotic models were generated in ApoE$^{-/-}$ and PCSK9-AAV8-induced atheroprone mice fed on a Western diet. We utilized single-cell RNA sequencing, along with molecular, cellular, and biochemical analyses, to investigate the physiological role of liver epsins in PCSK9-mediated LDLR degradation. Additionally, we explored the therapeutic potential of nanoparticle-encapsulated siRNAs targeting epsins 1 and 2 in ApoE$^{-/-}$ mice with established atherosclerosis.

Results:

Western diet (WD)-induced atherosclerosis was significantly attenuated in ApoE$^{-/-}$/Liver-DKO mice compared with ApoE$^{-/-}$ controls, as well as in PCSK9-AAV8-induced Liver-DKO mice compared with PCSK9-AAV8-induced wild-type (WT) mice accompanied by reductions in blood cholesterol and triglyceride levels. Mechanistically, single-cell RNA sequencing of hepatocytes and aortas isolated from atherosclerotic ApoE$^{-/-}$ and ApoE$^{-/-}$/Liver-DKO mice revealed epsin-deficient Ldlr^{hi} hepatocytes with diminished lipogenic potential. Notably, pathway analysis of hepatocytes showed increased LDL particle clearance and enhanced LDLR-cholesterol interactions under WD treatment in ApoE$^{-/-}$/Liver-DKO mice compared with ApoE$^{-/-}$ controls, correlating with decreased plasma LDL-C levels. Furthermore, pathway analysis of the aortas showed attenuated inflammation and endothelial activation, coupled with reduced lipid uptake, and enhanced cholesterol efflux under WD treatment in ApoE$^{-/-}$/Liver-DKO mice compared with ApoE$^{-/-}$ controls. Moreover, the absence of liver epsins led to an upregulation of LDLR protein expression in hepatocytes. We further demonstrated that epsins bind LDLR via the ubiquitin-interacting motif (UIM), enabling PCSK9-mediated LDLR degradation. Depleting epsins abolished this degradation, thereby preventing atheroma progression. Lastly, targeting liver epsins with nanoparticle-encapsulated epsins siRNAs effectively ameliorates dyslipidemia and inhibits atherosclerosis progression. These results are consistent with findings showing an increased epsin1 and epsin2 expression in atherosclerotic cardiovascular disease patients.

Conclusions:

Liver epsins drive atherogenesis by promoting PCSK9-mediated LDLR degradation, thereby elevating circulating LDL-C levels and heightening lesional inflammation. As such, targeting epsins in the liver represents a promising therapeutic strategy to mitigate atherosclerosis by preserving LDLR and enhancing LDL-C clearance in the liver.

41 **INTRODUCTION**

42 Atherosclerosis is a primary driver of cardiovascular diseases (CVDs), including coronary artery disease,
43 stroke, and peripheral artery disease[1]. CVDs remain the leading cause of mortality worldwide. In the
44 United States alone, heart-related conditions account for approximately 610,000 deaths annually—nearly
45 one-quarter of all deaths[2]. Atherosclerosis begins with low-density lipoprotein cholesterol (LDL-C)
46 accumulation in the subendothelial space, triggering an inflammatory cascade that promotes plaque
47 development and progression[3]. Elucidating the molecular mechanisms underlying plaque initiation,
48 progression, and rupture is critical for identifying therapeutic targets and preventing ischemic events,
49 disability, and death in patients with this chronic disease[4].

50 Modern lifestyles have contributed to the growing global prevalence of hyperlipidemia, and elevated
51 levels of LDL-C are an independent risk factor for atherosclerotic cardiovascular disease (ASCVD).
52 Familial hypercholesterolemia (FH) represents the most common inherited metabolic disorder,
53 characterized by markedly elevated plasma levels of LDL-C[5] and increased risk of premature ASCVD.
54 Mutations in the *Ldlr* gene, encoding the low-density lipoprotein receptor (LDLR), are the primary genetic
55 drivers of LDL-C elevation in FH[6]. Accordingly, therapeutic strategies aimed at lowering LDL-C remain
56 a cornerstone in the prevention and treatment of inflammation-driven atherogenesis.

57 The regulation of circulating LDL-C levels is in large part mediated through its clearance by low-density
58 lipoprotein receptors (LDLRs) that are expressed on hepatocytes. LDLR is a transmembrane protein that
59 facilitates the uptake of circulating LDL-C, serving as the primary mechanism for plasma LDL-C
60 clearance[7]. Proprotein convertase subtilisin/kexin type 9 (PCSK9), also primarily produced by the liver,
61 binds to LDLRs and promotes their lysosomal degradation, thereby reducing receptor recycling and
62 increasing plasma LDL-C levels[8]. Consequently, PCSK9 has emerged as a key therapeutic target. PCSK9
63 inhibitors, which prevent the interaction between PCSK9 and LDLR, have demonstrated potent lipid-
64 lowering effects in clinical trials and real-world use[9,10].

65 Animal models deficient in LDLR, such as LDLR knockout (KO) mice and rabbits, have been
66 instrumental in advancing the understanding of hyperlipidemia and atherosclerosis[11,12]. Furthermore,
67 Keeter et al. demonstrated that liver-specific overexpression of a variant of PCSK9 via adeno-associated
68 virus serotype 8 (AAV8) induces hyperlipidemia and accelerates atherosclerotic plaque formation[13]. More
69 recently, a CRISPR-based gene-editing strategy—VERVE-101—enabled potent and durable inactivation
70 of hepatic PCSK9 expression in nonhuman primates, resulting in substantial and sustained reductions in
71 plasma LDL-C levels[14]. These findings underscore the therapeutic potential of enhancing LDL-C
72 clearance by inhibiting PCSK9-mediated LDLR degradation as a highly effective strategy for treating
73 hyperlipidemia.

74 Despite significant therapeutic advances, the molecular mechanisms underlying PCSK9-mediated LDLR
75 degradation remain poorly understood. In particular, it is unclear whether specific endocytic adaptor
76 proteins facilitate LDLR internalization and degradation in response to PCSK9. Elucidating these
77 molecular processes may uncover novel therapeutic targets, especially for patients who develop resistance
78 or exhibit limited responsiveness to current PCSK9 inhibitors.

79 Epsins, a family of endocytic adaptor proteins, have recently emerged as critical regulators and potential
80 therapeutic targets of atherosclerosis[15]. We previously demonstrated that epsins 1 and 2 are upregulated
81 in atherosclerotic plaques of apolipoprotein E-deficient ($ApoE^{-/-}$) mice fed a Western diet (WD)[4,16,17].

82 Endothelial cell (EC)-specific deletion of epsins markedly attenuated atherogenesis in this model,
83 primarily by reducing arterial inflammation, downregulating adhesion molecule expression, limiting
84 monocyte recruitment, and alleviating endoplasmic reticulum (ER) stress through stabilization of inositol
85 1,4,5-trisphosphate receptor type 1 (IP3R1) in ECs[4].

86 Moreover, we demonstrated that myeloid-specific epsin deficiency in ApoE$^{-/-}$ mice impeded lesion
87 progression by inhibiting foam cell formation and enhancing efferocytosis within the plaque[16,17]. These
88 mice also exhibited improved reverse cholesterol transport and promoted atheroma regression through the
89 stabilization of ATP-binding cassette transporter G1 (ABCG1) in macrophages[16,17]. Despite the central
90 role of epsins in the initiation and progression of atherosclerosis as well as in plaque regression, their
91 potential involvement in hepatic regulation of circulating LDL-C levels via modulation of LDLR stability
92 remains largely unexplored. Addressing this gap may provide mechanistic insights into the biological
93 functions of epsin and unveil a novel therapeutic avenue for the treatment of hyperlipidemia and
94 atherosclerosis.

95 To investigate the physiological role of hepatic epsins in regulating LDLR stability during atherosclerosis,
96 we generated a novel ApoE$^{-/-}$ mouse with liver-specific deletion of epsins 1 and 2 (ApoE$^{-/-}$/Liver-DKO).
97 Here, we demonstrated that these mice exhibit reduced plaque formation compared with ApoE$^{-/-}$ mice on
98 WD. We observed enhanced LDLR proteins in the liver of ApoE$^{-/-}$/Liver-DKO compared with ApoE^{-}
99 $^{/-}$ mice, suggesting that epsins are required for LDLR degradation, and that their loss enhances LDLR
100 stability by preventing its lysosomal degradation. Mechanistically, epsins directly bind LDLR through
101 their ubiquitin-interacting motif (UIM), and PCSK9-induced LDLR degradation is largely abolished in
102 the absence of hepatic epsins.

103 Single-cell RNA sequencing analysis of aorta and liver revealed upregulation of pathways involved in
104 LDL particle clearance in ApoE$^{-/-}$/Liver-DKO mice, consistent with elevated hepatic LDLR expression.
105 Consistently, in mice harboring the gain-of-function human *PCSK9* D374Y mutation, we observed
106 elevated hepatic epsin expression and suppressed LDLR levels. When we introduced *PCSK9* D374Y in
107 WT and Liver-DKO mice via AAV8, we observed striking inhibition of plaque development in Liver-
108 DKO harboring *PCSK9* D374Y transgene—supporting a model in which liver epsins mediate PCSK9-
109 driven LDLR degradation and promote atherogenesis. Furthermore, silencing hepatic epsins via delivery
110 of nanoparticle-encapsulated epsins siRNAs effectively reduced dyslipidemia and atherosclerosis,
111 establishing liver epsins as a promising therapeutic target for hyperlipidemia and cardiovascular disease.

112 **MATERIALS and METHODS**

113 **Animal Models**

114 In this study, all animal procedures were performed in compliance with institutional guidelines and mouse
115 protocols were approved by the Institutional Animal Care and Use Committee (IACUC) of Boston
116 Children's Hospital, MA, USA. Both male and female mice were used. C57BL/6 mice (stock #00664),
117 ApoE $^{-/-}$ mice (stock #002052), and Alb-Cre delete mice (stock #035593) were all purchased from Jackson
118 Research Laboratory. As double knockout mice of Epsin 1 and 2 (Epsin 1$^{-/-}$; Epsin2 $^{-/-}$) led to embryonic
119 lethality, we generated conditional Epsin1 $^{fl/fl}$; Epsin2 $^{-/-}$ mice previously described[18]. ApoE $^{-/-}$ mice, Alb-
120 Cre$^{+/-}$ mice and Epsin1 $^{fl/fl}$; Epsin2 $^{-/-}$ mice were backcrossed to C57BL/6 background. The Alb-Cre$^{+/-}$ mice
121 were used for deletion of *loxP*-flanked Epsin1 in the liver. We bred Epsin1 $^{fl/fl}$; Epsin2 $^{-/-}$ mice with Alb-
122 Cre$^{+/-}$ mice to generate Epsin1 $^{fl/fl}$; Epsin2 $^{-/-}$; Alb-Cre$^{+/-}$ hepatocyte-specific Epsins deficient (Liver-DKO)
123 mice (Figure S1A). In addition, we bred Epsin1 $^{fl/fl}$; Epsin2 $^{-/-}$; Alb-Cre$^{+/-}$ mice with ApoE$^{-/-}$ (C57BL/6)
124 background to generate Epsin1 $^{fl/fl}$; Epsin2 $^{-/-}$; Alb-Cre$^{+/-}$; ApoE $^{-/-}$ mice (ApoE $^{-/-}$/Liver-DKO) (Figure S1B).

125 The control mice for Epsin1 $^{fl/fl}$; Epsin2 $^{-/-}$; Alb-Cre$^{+/-}$ (Liver-DKO) mice were Epsin $^{+/+}$; Epsin2 $^{+/+}$; Alb-
126 Cre $^{+/-}$ mice (WT) (Figure S1A). Western blot and immunofluorescence analyses of Epsins 1 and 2 in
127 hepatocytes isolated from Liver-DKO versus WT mice confirmed that both Epsin1 and Epsin2 were
128 markedly downregulated in livers of Liver-DKO mice (Figures S2A and S2B). The control mice for
129 Epsin1 $^{fl/fl}$; Epsin2 $^{-/-}$; Alb-Cre$^{+/-}$; ApoE $^{-/-}$ mice (ApoE$^{-/-}$/Liver-DKO) were Epsin1 $^{+/+}$; Epsin2 $^{+/+}$; Alb-Cre
130 $^{+/-}$; ApoE$^{-/-}$ (ApoE$^{-/-}$) (Figure S1B). For control mice, in addition to ApoE$^{-/-}$; Epsin 1$^{+/+}$; Epsin 2 $^{+/+}$ mice,
131 we also used ApoE$^{-/-}$; Epsin 1$^{+/+}$; Epsin 2 $^{+/+}$ mice with a single copy of Alb-Cre, and ApoE $^{-/-}$ mice; Epsin1
132 $^{fl/fl}$; Epsin2 $^{-/-}$ littermates lacking the single copy of Alb-Cre. To simplify the terminology, we refer to these
133 control mice as ApoE$^{-/-}$, as results were not different in any of the analyses we performed.

134 To induce atherosclerosis, mice were fed a Western diet (WD, Protein 17% kcal, Fat 40% kcal,
135 Carbohydrate 43% kcal; D12079B, Research Diets, New Brunswick, USA) starting at the age of 6–8
136 weeks for 8–20 weeks. Mice were sacrificed at different time points based on experimental design and
137 the liver, blood, heart, and aorta were harvested. For each experimental model and time point, 6–10 mice
138 were analyzed and both male and female mice were used in separate groups. In the current study, we did
139 not exclude any mice when analyzing the data.

140 **Liver and Aorta Single-cell Preparation and Single-cell RNA Sequencing**

141 For liver cell isolation, the ApoE$^{-/-}$ and ApoE$^{-/-}$/Liver-DKO mice (n=3) were anesthetized and restrained,
142 and the skin sprayed with 70% ethanol. The liver and other inner organs were revealed by cutting through
143 the skin and peritoneum. A 24G needle was carefully inserted into the inferior vena cava and secured
144 with a clamp, and chelating solution (0.05M 4-(2-hydroxyethyl)-1-piperazineethanesulfonic acid
145 (HEPES), pH 7.2, 10 mM ethylene glycol-bis(β-aminoethyl ether)-N, N, N', N'-tetraacetic acid (EGTA)
146 in Hank's balanced salt solution (HBSS) without $CaCl_2$ and $MgCl_2$) was run at a low speed (1.5–2
147 mL/minute). The portal vein was then cut, and perfusion speed was increased to a flow rate of 7 mL/minute.
148 After that, the diaphragm was cut and the anterior vena cava clamped. The chelating perfusion was run
149 for 7 minutes and then switched to collagenase solution (0.05 M HEPES, pH 7.2, 4.7 mM $CaCl_2$, 20 μg/mL
150 Liberase, Sigma LIBTM-RO) at a flow rate of 7 mL/minute for 7 minutes. The liver was then removed
151 and passed through a 70 μm cell strainer with 10 ml ice-cold HBSS without $CaCl_2$ and $MgCl_2$. The
152 resulting single-cell suspension was centrifuged at 300 g for 5 minutes at 4 °C and washed ice-cold HBSS.

153 The liver cell pellet was suspended in phosphate-buffered saline (PBS) buffer containing 0.04% bovine
154 serum albumin (BSA).

155 For the aortic sample preparation, we used our previously reported protocol with minor modification[19].
156 Briefly, mouse aortas isolated from the ApoE$^{-/-}$ and ApoE$^{-/-}$/Liver-DKO mice (n=3) were cut into small
157 pieces and placed in 6.5 mL of enzyme solution at 37 °C for 1.5 hours (5 mL of Dulbecco's Modified
158 Eagle Medium (DMEM), 1 mL of trypsin, 10 mg/mL collagenase type I, 10 mg/mL collagenase type IV,
159 50 µL elastin [stock:2.5 mg/mL], 200 µL of collagenase type II [stock: 1 mg/mL], 200 µL of collagenase
160 XI [stock: 1 mg/mL], 200 µL of hydrolase [stock: 1 mg/mL], 100 µL of Liberase [stock: 3.85 mg/mL,
161 Roche], 10 µL of DNase I [stock: 5 U/ µL, Sigma]). This solution was then filtered with a 40 µm cell
162 strainer, centrifuged (400 g for 5 minutes), and the cell pellet was suspended in a PBS buffer containing
163 0.04% BSA. The isolated liver and aorta cells were counted and diluted into 1000 cells/ µL. The single-
164 cell RNA-seq library construction was performed according to the 10x genomics protocol (GEMs, Single
165 cell 3' Reagent Kits v3.1, 10x Genomics). The prepared libraries were sequenced on the HiSeq 2500
166 Sequencing System (Illumina, San Diego, CA) with 100-bp paired end reads.

167 **Single-cell Transcriptome Data Analysis**

168 First, we employed Cell Ranger (version 7.1.0) to map the raw reads of RNA sequencing data to the mouse
169 genome (version mm10) and count the unique molecular identifier (UMI) for each gene. We then
170 proceeded with the resulting UMI count matrix using the Seurat R package (version 4.3.0)[20]. We retained
171 high-quality cells expressing between 200 and 2500 genes, excluding those with over 20% mitochondrial
172 reads in the liver datasets and 5% mitochondrial reads in the aorta datasets. Additionally, we filtered out
173 rarely expressed genes detected in fewer than 3 cells. After filtering, the high-quality data was normalized,
174 cell-level scaled with 10k reads, and natural-log transformed by adding 1. The normalized data underwent
175 further processing steps: scaling (ScaleData function), principal component analysis (PCA) (RunPCA
176 function, npcs =30), Uniform Manifold Approximation and Projection (UMAP) (RunUMAP function,
177 reduction = "pca", dims = 1:30), shared nearest neighbor graph (SNNG) construction (FindNeighbors
178 function, reduction = "pca", dims = 1:30), and cell clustering (FindCluster function, resolution=0.1).

179 We conducted differentially expressed gene (DEG) analyses in one cluster versus other clusters using the
180 FindAllMarkers function. The Wilcoxon test method was used by default, with a minimum percentage of
181 expressed cells set to 25% and a minimum log2 fold change of 0.25. Cell types were annotated based on
182 known marker genes from PanglaoDB[21], cell-Taxonomy[22], disco[23] databases, and relevant literature.
183 Marker gene expressions were visualized by DotPlot and VlnPlot functions. For cell rank for directed
184 single-cell transition mapping, we utilized cellrank (version 2.0.4)[24] with default parameters. The
185 metabolite-mediated cell-cell communication was analyzed by MEBOCOST (version 1.0.0)[25]. The data
186 were analyzed combined for both conditions following the tutorial on the MEBOCOST website
187 (https://github.com/zhengrongbin/MEBOCOST). The prediction of sender-metabolite-sensor-receiver
188 communication events was visualized by the bar and lollypop plots, using the ggplot2 library. Additionally,
189 we performed cell-cell communication analysis using Cellchat (version 1.5.0)[26]. The communication
190 probability of each condition was analyzed to highlight differences between conditions, and
191 communication events were visualized using bar, flow, and circle plots. Furthermore, Gene Ontology (GO)
192 functional enrichment analysis was performed using the clusterProfiler R package (version 3.18.1)[27], and
193 visualized by bar, lollipop, and cnet plots.

194 Finally, our research involved a comprehensive approach to quantifying the cardioprotective potential
195 based on gene expression. We began by compiling a curated list of genes associated with the clearance of
196 low-density lipoprotein cholesterol (LDL-C) in the liver that were mapped to the risk genes of coronary
197 artery disease (CAD) identified by a genome-wide association study (GWAS), such as *Ldlr*, *Apoe*[28]. The
198 risk genes for coronary artery disease are listed in Table S1. We then computed a CAD protective score
199 for each sample. First, we extracted normalized expression values of the selected CAD protective genes.
200 This process involved collecting data on the expression levels of these genes from each sample, which
201 was then normalized to account for any variations in the data collection process. The CAD protective
202 score was then calculated as the average expression of these genes chosen across each sample, providing
203 a single composite metric representing overall protective gene activity. We employed violin plots to
204 evaluate differences in CAD protective scores between experimental groups. These plots visualized the
205 distribution of scores across conditions, allowing both the spread and central tendency to be assessed. The
206 statistical significance of these differences was then rigorously evaluated using a t-test, a crucial step in
207 our analysis. In addition to data analysis from ApoE$^{-/-}$ and ApoE$^{-/-}$/Liver-DKO mice, we reanalyzed the
208 scRNA-seq data from PCSK9 D374Y mutant with C57BL/6 genetic background (GSE254971) and
209 compared with our healthy control C57BL/6 mice using the methods described above.

210 **Human Samples**

211 The healthy controls and diseased aortic arch samples from atherosclerosis patients were purchased from
212 Maine Medical Center Biobank. The medical information details of the atherosclerotic patients and
213 healthy people samples are listed in Table S1. The paraffin sections were deparaffinized, and we
214 performed antigen retrieval to unmask the antigenic epitope with 10 mM Sodium Citrate, pH 6.0, with
215 0.5% Tween 20 at 95 °C for 30 minutes. Then the slides were allowed to cool for 30 minutes before
216 staining.

217 **Oil Red O Staining**

218 Whole aortas were dissected symmetrically, pinned to parafilm to allow the *en face* to be exposed and
219 fixed in formalin for 12 hours. Aortas were washed in PBS 3 times and rinsed in 100% propylene glycol
220 followed by staining with 0.5% Oil Red O solution for 20 minutes at 65 °C. Aortas were then put in 85%
221 propylene glycol for 2 minutes, followed by three washes in DD Water. Imaging was performed using a
222 Nikon SMZ1500 stereomicroscope, SPOT Insight 2Mp Firewire digital camera, and SPOT Software 5.1.
223 The *en-face* Oil Red O-stained areas were manually traced and further quantified by NIH ImageJ software
224 with n=3 or more. Hearts were embedded in O.C.T compound and sectioned at 8 microns. Cryostat
225 sections of mouse aortic root were fixed in 4% paraformaldehyde for 15 minutes. Slices were washed in
226 PBS followed by staining with freshly prepared 0.5% Oil Red O solution in isopropanol for 10 minutes at
227 37 °C. Slices were then put in 60% isopropanol for 30 seconds, followed by 3 washes in water. Slices
228 were mounted with 90% Glycerin. The Oil Red O (ORO)-stained aortic root lesion areas were quantified
229 by NIH ImageJ software with n=3 or more.

230 **Periodic Acid-Schiff's Staining**

231 Periodic acid-Schiff's staining was performed according to manufacturer's instructions. In brief, paraffin
232 sections of mouse liver samples were deparaffinized by xylene (2 changes, each for 5 minutes) and
233 followed by rinsing in absolute alcohol for 3 changes (each for 1 minute) and were rehydrated by running

234 distilled water for 1 minute. The slides were immersed in 0.5% Periodic acid for 7 minutes and followed
235 by rinsing in running distilled water for 10 seconds. The slides were further immersed into Optimized
236 Schiff's Water for 15 minutes and followed by rinsing in running tap water for 5 minutes. For nuclear
237 staining, the slides were immersed in Modified Mayer's Hematoxylin for 2 minutes and then rinsed in
238 running tap water for 1 minute. The slides were further immersed into Light Green to counterstain until
239 the desired background intensity is reached. The stained slides were dehydrated by absolute alcohol (3
240 changes, each for 1 minute) and cleared by xylene (3 changes, each for 1 minute) and mounted using
241 Permount (ThermoFisher). The quantification of glycogen-stained areas in the liver samples was
242 performed by NIH ImageJ software with n=3 or more.

243 **Immunofluorescence Staining**

244 The liver samples and aortas from both ApoE$^{-/-}$ and ApoE$^{-/-}$/Liver-DKO mice were subjected for
245 cryosections, and sections were further fixed in 4% paraformaldehyde for 15 minutes. The slides were
246 blocked by blocking buffer (PBS/3% BSA/3% donkey serum/0.3% triton) for 30 minutes, and were further
247 incubated by primary antibodies (antibody list is shown in Major Resource Table) for overnight at 4°C.
248 The slides were washed 3 times for 10 minutes each wash in PBS/0.3% triton buffer and were then
249 incubated with secondary antibodies at room temperature for 1 hour. Next, the slides were washed 3 times
250 for 10 minutes, each washed in PBS/0.3% triton buffer. After the second wash, DAPI was used for nuclei
251 staining. The slides were mounted using a Fluoroshield mounting medium. Imaging was performed using
252 Zeiss LSM 880 Confocal Acquisition & Analysis. Samples stained without the primary antibody were
253 obtained using the same settings as negative controls (Figure S14). Mean fluorescence intensity (MFI) of
254 antibody staining was determined using NIH ImageJ software with n=3 or more.

255 **Synthesis of siRNA Nanoparticles (NPs)**
256
257 In this study, a robust self-assembly method was used to prepare the polymer-lipid hybrid NPs for siRNA
258 delivery[29]. In brief, G0-C14 and PLGA were dissolved separately in anhydrous dimethylformamide (DMF)
259 to form a homogeneous solution at concentrations of 2.5 mg/mL and 5 mg/mL, respectively. DSPE-PEG-
260 OCH_3 (DSPE-mPEG) was dissolved in HyPure water (GE Healthcare Life Sciences, catalog no. SH30538)
261 at a concentration of 0.1 mg/mL. 1 nmole Epsin1 siRNA and 1 nmole Epsin2 siRNA were gently mixed
262 with 100 μL of the G0-C14 solution. The mixture of siRNA and G0-C14 was incubated at room
263 temperature for 15 minutes to ensure the full electrostatic complexation. Next, 500 μL of PLGA polymers
264 were added and mixed gently. The resultant solution was subsequently added dropwise into 10 mL of
265 HyPure water containing 1 mg DSPE-mPEG under magnetic stirring (1,000 rpm) for 30 minutes. The
266 siRNA NPs were purified by an ultrafiltration device (EMD Millipore, MWCO 100 kDa) to remove the
267 organic solvent and free excess compounds via centrifugation at 4 °C. After washing 3 times with HyPure
268 water, the siRNA NPs were collected and finally resuspended in pH 7.4 PBS buffer. The NPs were used
269 freshly or stored at -80 °C for further use.

270 **RNA Isolation and Real-time Quantitative PCR**

271 Total RNA was extracted from the liver tissue with the RNeasy Mini Kit (Qiagen) according to the
272 manufacturer's instructions, including the optional step to eliminate genomic DNA. The extracted RNA
273 was used for RT-qPCR according to the experimental designs. For the RT-qPCR, mRNA was reverse-
274 transcribed to cDNA with the iScript cDNA Synthesis Kit (Bio-Rad Laboratories). 2 μL of 5-fold diluted

275 cDNA product was subjected to the RT-qPCR in StepOnePlus Real-Time PCR System (Applied
276 Biosystems) using SYBR Green PCR Master Mix reagent as the detector. PCR amplification was
277 performed in triplicate on 96-well optical reaction plates and replicated in at least three independent
278 experiments. The Delta-Delta Ct (ΔΔCt) method was used to analyze qPCR data. The Ct of β-actin cDNA
279 was used to normalize all samples. Primers are listed in the Major Resource Table.

280 **Analysis of Plasma Cholesterol and Triglyceride Levels**

281 Blood was removed from the right atrium of the mouse heart after sacrifice with isoflurane. Blood was
282 allowed to clot for 30 minutes at room temperature followed by centrifugation at 3000 g at 4 °C for 20
283 minutes. Serum was transferred to a new tube and stored at -20 °C. Serum cholesterol and lipid levels
284 were determined using the Cholesterol Assay Kit and Triglyceride Assay Kit (Abcam).

285 **Immunoprecipitation and Western Blotting**

286 For immunoprecipitation, HepG2 cells were lysed with radioimmunoprecipitation assay (RIPA) buffer
287 (50 mM Tris, pH 7.4, with 150 mM NaCl, 1% Nonidet P-40, 0.1% sodium dodecyl sulfate (SDS), 0.5%
288 sodium deoxycholic acid, 0.1% sodium dodecyl sulfate, 5 mM N-ethylmaleimide and protease inhibitor
289 cocktail). For LDLR ubiquitination experiments, HepG2 cells were lysed using a denaturing buffer (1%
290 SDS in 50 mM Tris, pH 7.4) and boiled at 95 °C for 10 minutes to denature protein complexes. Lysates
291 were re-natured using nine volumes of ice-cold RIPA buffer, then prepared for immunoprecipitation as
292 follows. Cell lysates were pre-treated with Protein A/G Sepharose beads at 4 °C for 2 hours to remove
293 nonspecific protein followed by centrifugation at 12000 rpm for 5 minutes at 4 °C. Supernatant was
294 transferred to a new tube, incubated with Protein A/G Sepharose beads and antibodies against Epsin1 or
295 LDLR or ubiquitin at 4 °C overnight. Mouse IgG was used as a negative control. Protein A/G beads were
296 washed with RIPA buffer 2 times, followed by PBS once. Then, beads were suspended with an 80 μL 2x
297 loading buffer and heated at 95 °C for 10 minutes. After centrifugation, precipitated proteins were
298 visualized by Western blot. Proteins were resolved by SDS-PAGE gel and electroblotted to nitrocellulose
299 membranes. NC membranes were blocked with 5% milk (w/v) and blotted with antibodies. Western blots
300 were quantified using NIH Image J software with n=3 or more. The raw films for western blots exposure
301 were submitted in Supplemental Material.

302 **PCSK9 Adeno-associated Virus 8 (AAV8) Tail Vein Injection**

303 Eight-week-old male C57BL/6 mice, both WT and Liver-DKO mice (n=6), were intravenously injected
304 via tail vein with a single dose of 2 x 10^{11} viral PCSK9-AAV8 and fed a WD for 20 weeks. The serum
305 samples collected from both WT and Liver-DKO mice were subjected for triglyceride and cholesterol
306 measurements. The aortas were isolated for *en face* ORO staining and histology analysis, and the liver
307 tissue from both WT and Liver-DKO mice was collected for further histology analysis and protein lysate
308 preparation.

309 **Nanoparticle-encapsulated Epsin1 and Epsin2 siRNAs Tail Vein Injection**

310 Eight-week-old male C57BL/6 mice, ApoE $^{-/-}$ mice were fed a WD for 8 weeks and further divided into
311 two groups (n=6). The control group mice were intravenously injected via tail vein with control siRNA
312 NPs, and the experimental group mice were injected with 1 nmoles[29] epsin1 and epsin2 siRNA NPs for
313 continuous three weeks. Two injections per week. After injection, the serum samples collected from both

314 control siRNA and epsin 1 and 2 siRNA NPs injected groups were subjected to triglyceride and cholesterol
315 measurement. The aortas were isolated *en face* ORO staining and histology analysis, and the liver tissue
316 from both control siRNA and epsin 1 and 2 siRNA NPs were collected for protein lysate preparation.

317 **Cell Culture and Plasmids Transfection**

318 The HepG2 cell line (ATCC no. HB-8065) was used for plasmid transfection to map the binding sites of
319 Epsin1 to LDLR. Flag-tagged Epsin1WT, Epsin1ΔUIM, Epsin1ΔENTH, Epsin1-DPW/NPF truncation
320 constructs, and pcDNA vector were prepared previously in our laboratory. HepG2 cells were cultured in
321 DMEM (10% fetal bovine serum (FBS) and 1% Pen-Strep) at 37°C in humidified air containing 5% CO_2
322 atmosphere and transfected using Lipofectamine 2000 as instructed by the manufacturer.

323 **Epsin1 and Epsin2 siRNAs Transfection, PCSK9-AAV8 Infection**

324 HepG2 cells were cultured in DMEM (10% FBS and 1% Pen-Strep) at 37°C in humidified air containing
325 5% CO_2 atmosphere. One day before transfection, plate cells in 1 mL of growth medium without
326 antibiotics such that they will be 30-50% confluent at the time of transfection. The transfection of epsin1
327 and epsin2 siRNAs was performed according to the manufacturer's instructions. The preparation of RNAi
328 duplex-Lipofectamine RNAiMAX complexes by mixture of either control siRNA or epsin1 and epsin2
329 siRNAs (Dharmacon, Horizon Discovery) and Lipofectamine RNAiMAX, maintaining the mixture at
330 room temperature for 20 minutes, and then adding the complexes to each well containing cells. The cells
331 were incubated for 48 hours at 37°C in a CO_2 incubator. The PCSK9-AAV8 stock (10^{13} GC/ml) was
332 diluted by culture media into 10^{10} GC for the infection. The original cell culture media were removed and
333 added to the PCSK9-AAV8 containing media for cell culture. The cells were collected 3 days after the
334 PCSK9-AAV8 infection.

335 **Hepatocyte Primary Culture, MG132 Treatment, PCSK9-AAV8 Infection**

336 The methods of perfusion and digestion of liver were reported in liver single-cell preparation part above.
337 The digested liver was transferred to a 10 cm plate with plating media (DMEM low glucose, 5% FBS, 1%
338 Penicillin-Streptomycin Solution), and the liver cells were gently released with fine tip forceps. The liver
339 cell suspension was filtered through a 70 μm cell strainer into a 50 mL tube and then spun at 50 g for 2
340 minutes at 4 °C. While the samples were spinning, a fresh Percoll solution (90% Percoll in 1xHBSS) was
341 prepared. The supernatant was aspirated, and 10 mL of plating media was added and resuspend by gentle
342 swirling. Next, 10 mL Percoll solution was added and mixed thoroughly by inverting the tube several
343 times. After spinning at 200 g for 10 minutes at 4 °C, the supernatant was aspirated, 20 mL of plating
344 media was added, and then spun at 50 g for 2 minutes at 4 °C. The supernatant was aspirated, and 20 mL
345 of plating media was added. Hepatocytes were counted and plated on collagen-coated cell culture 6-well
346 plates. After 3 hours, the medium was changed to warm maintenance media (Williams E media, 1%
347 Glutamine, 1% Penicillin-Streptomycin Solution). Three hours after plating, the proteasome inhibitor
348 MG132 solution was added to the cultured primary hepatocytes. After 6 hours, the primary hepatocytes
349 were subjected to PCSK9-AAV8 infection as mentioned above. The primary hepatocytes were collected
350 and lysed for protein preparation.

351 **DiI-LDL Uptake Assay**

352 Hepatocytes isolated from WT and Liver-DKO mice were seeded plated in black clear bottom 96-well
353 plates and further subjected to PCSK9-AAV8 infection. During the last 5 hours of PCSK9-AAV8
354 infection, hepatocytes were exposed to DiI-LDL (10 μg/ml) and then washed with two changes of PBS.
355 The intracellular fluorescence intensity of DiI-LDL was then quantified using the SpectraMax Gemini
356 XPS/EM Microplate Readers (Molecular Devices; ex 554/em 571). In addition, isolated hepatocytes were
357 seeded in plated 12-well plates with sterilized coverslips, and hepatocytes were subjected to PCSK9-
358 AAV8 infection and were further exposed to DiI-LDL (10 μg/ml). The hepatocytes were washed with
359 two changes of PBS and were further fixed by 4% PFA for 10 minutes. DAPI was used for nuclei staining
360 after PBS washing. The coverslips were mounted using a Fluoroshield histology mounting medium
361 (Sigma-Aldrich). Imaging was performed using Zeiss LSM 880 Confocal Acquisition & Analysis. Mean
362 fluorescence intensity (MFI) of DiI-LDL fluorescence was determined using NIH ImageJ software with
363 n=3 or more.

364 **Avoiding Bias in Quantitative Analysis**

365 We had two blinded observers select representative images from a panel of images collated from all
366 experiments performed on any given sample. Representative images of immunofluorescence, Oil Red O
367 and Periodic acid-Schiff's staining were selected based on the most accurate representation of similarity
368 with the mean value for each experimental group. The way to select a representative image would be an
369 image that is most similar to all the other images in the set. Representative images from
370 immunofluorescence, Oil Red O and Periodic acid-Schiff's stains were selected based on high quality,
371 resolution, and accurate representation of similarity with the mean value of each experimental group.

372 **Statistical Analysis**

373 Gene expression was assessed by quantifying mRNA levels of target genes via qPCR, with normalization
374 to the internal control, β-actin. The images of western blotting, immunofluorescence, aortic lesion sizes,
375 Oil Red O, and Periodic acid-Schiff's-stained images were quantified by ImageJ software (NIH, Bethesda,
376 MD) running on Apple OS X. Statistical analysis of samples including Oil Red O, IF, and Periodic acid-
377 Schiff's stains were performed by blinding in which each animal was assigned a number and data was
378 collected based on the assigned number with genotype and experimental condition unknown to the data
379 collector. Quantitative data were analyzed by 2-tailed, unpaired, or paired Student's t-test or two-way
380 ANOVA with post hoc test, using Prism 8.0 (GraphPad Software) running on Apple OS X. All data are
381 presented as are the mean ± SEM.

382 **Data Availability**

383 The liver and aorta scRNA-seq data (GSE273386) in ApoE$^{-/-}$ and ApoE$^{-/-}$ /Liver-DKO mice are available
384 in the Gene Expression Omnibus. The scRNA-seq data (GSE254971) for D374Y mCherry-APOB mice
385 are available in the published paper entitled "Kupffer cells dictate hepatic responses to the atherogenic
386 dyslipidemic insult" (https://doi.org/10.1038/s44161-024-00448-6). Source data is provided with this
387 paper.

388 **RESULTS**

389 **Elevated Epsin1 and Epsin2 Expression in the Aortic Biopsies of Atherosclerotic Cardiovascular**
390 **Disease Patients.**

391 We measured the protein expression of epsin1 and epsin2 between healthy controls and atherosclerotic
392 cardiovascular disease (ASCVD) patients by immunofluorescence staining. Intriguingly, we found 98%
393 and 68% increases of epsin1 and epsin2 protein levels, respectively, in diseased aortic samples (Figure
394 S3A-S3C). As expected, we found remarkably elevated macrophage marker CD68 protein expression in
395 the aortic biopsies of ASCVD patients (Figure S3A-S3C), indicating more macrophage accumulation and
396 increased atherosclerotic lesions in ASCVD patients. Importantly, we discovered a substantially higher
397 percentage of colocalization between epsin1 and CD68, and a higher overlay percentage between epsin2
398 and CD68 in the macrophages in ASCVD patients than in healthy controls (Figure S3A-S3C).

399 **Depletion of Epsins in the Liver Decreases Atherosclerotic Lesion, Macrophage Accumulation, and**
400 **Plasma Lipid Levels.**

401 We explored the physiological role of hepatic epsins in lipoprotein metabolism and atherosclerosis by
402 employing liver-specific epsins-deficient mice (ApoE$^{-/-}$/Liver-DKO) and compared their phenotypic
403 outcomes with ApoE$^{-/-}$ controls. Notably, in ApoE$^{-/-}$/Liver-DKO mice fed a WD, plasma cholesterol and
404 triglycerides were dramatically reduced by 55% and 34%, respectively vs ApoE$^{-/-}$ controls (Figure 1A).
405 *En face* Oil Red O staining of aortas from ApoE$^{-/-}$ and ApoE$^{-/-}$/Liver-DKO mice fed a WD revealed a 69%
406 reduction in atherosclerotic lesion area in ApoE$^{-/-}$/Liver-DKO mice compared with ApoE$^{-/-}$ controls
407 (Figure 1B). The lesion areas of the aortic roots in ApoE$^{-/-}$/Liver-DKO mice revealed a 67% reduction in
408 mean atherosclerotic lesion area compared with ApoE$^{-/-}$ controls (Figure 1C). These findings indicate that
409 liver epsins likely play crucial roles in lipoprotein metabolism with a major impact on the pathogenesis of
410 atherosclerosis.

411 **Reduced Inflammatory Macrophages, Attenuated Endothelial Inflammation, Enriched Contractile**
412 **Vascular Smooth Muscle Cells, and Reduced Proportion of Fibroblasts in the Aortas in ApoE$^{-/-}$**
413 **/Liver-DKO Mice.**

414 We investigated cellular alterations in the aortas of ApoE$^{-/-}$ and ApoE$^{-/-}$/Liver-DKO mice by single-cell
415 RNA sequencing (Figure S4A). The UMAP visualization uncovered 10 major cell types annotated
416 according to the expression patterns of cell type-specific marker genes (Figure 1D, Figure S4B).
417 Additional analyses revealed a reduced proportion of macrophages expressing CD68 in the aortas of
418 ApoE$^{-/-}$/Liver-DKO mice that had diminished expression of inflammatory pathway genes involving
419 complement, leukocyte, and lymphocyte activation (Figure 1D, 1F, 1H, Figure S5D). In addition, the
420 proportion of endothelial cells with no significant difference in expression of endothelial cell marker genes
421 in the aortas in ApoE$^{-/-}$/Liver-DKO mice, such as Pecam1/CD31, was increased (Figure 1D, Figure S4C,
422 S4D). Importantly, the mRNA levels of the inflammatory monocytic adhesion molecules, including
423 VCAM-1 and ICAM-1, were decreased in the endothelial layer of aortas in ApoE$^{-/-}$/Liver-DKO versus
424 ApoE$^{-/-}$ mice (Figure 1H). Further analyses identified upregulated pathways involved in regulation of
425 endothelial cell differentiation, endothelial cell development, vascular endothelial growth factor receptor
426 signaling pathway, regulation of fatty acid metabolic process, and triglyceride metabolic process and
427 downregulated pathways of regulation of endothelial cell apoptotic process, regulation of endothelial cell
428 migration, and endothelial cell activation in endothelial cells in the aortas of ApoE$^{-/-}$/Liver-DKO mice

429 (Figure 1E, 1G, Figure S5A, S5C, Figure S6C, S6E). Intriguingly, the percentage of vascular smooth
430 muscle cells (VSMCs) with elevated expression of contractile VSMC marker genes in the aortas in ApoE-
431 /-/Liver-DKO mice, such as Acta2/α-SMA and Tagln/SM22, was increased (Figure 1D, 1H, Figure S4C,
432 S4D). In contrast, the proportion of fibroblasts (FB) with diminished expression of fibroblasts marker
433 genes in the aortas in ApoE$^{-/-}$/Liver-DKO mice, such as Col1a1/Collagen I, was reduced (Figure 1D, 1H,
434 Figure 2D, Figure S4C, S4D). In addition, pathways of cell-matrix adhesion, extracellular matrix
435 organization, and inflammatory response in both fibroblasts and VSMCs in the aortas of ApoE$^{-/-}$/Liver-
436 DKO mice are downregulated (Figure S5B, S5D, S5E, Figure S6F, S6G). Correspondingly, the *Pecam1*-
437 associated pathway was upregulated in endothelial cells, and collagen-associated pathways were
438 downregulated in the aortas of ApoE$^{-/-}$/Liver-DKO mice compared with ApoE$^{-/-}$ controls (Figure S6A,
439 S6B).

440 Consistent with the single-cell RNA sequencing analyses, we discovered remarkably diminished CD68
441 protein expression in the aortas in ApoE$^{-/-}$/Liver-DKO mice compared with ApoE$^{-/-}$ controls,
442 demonstrating impeded macrophage accumulation in the atherosclerotic lesions (Figure 2A). Importantly,
443 we detected attenuated inflammatory scavenger receptors including CD36 and LOX-1 in the aortas of
444 ApoE$^{-/-}$/Liver-DKO versus ApoE$^{-/-}$ control mice (Figure 2B, 2C). In addition, the protein levels of α-SMA
445 and SM22 were markedly increased in the aortas of ApoE$^{-/-}$/Liver-DKO mice compared with ApoE$^{-/-}$
446 controls which is consistent with increased contractile SMCs (Figure 2A, 2D). Furthermore, in keeping
447 with the decreased number of fibroblasts in the aortas of ApoE$^{-/-}$/Liver-DKO mice versus ApoE$^{-/-}$ controls
448 (Figure 1D), the collagen-1 protein levels were reduced (Figure 2D). Furthermore, the aortic endothelial
449 layer in ApoE$^{-/-}$/Liver-DKO versus ApoE$^{-/-}$ mice had markedly decreased ICAM-1 and P-Selectin protein
450 levels which is consistent with reduced endothelial cell activation and macrophage accumulation (Figures
451 2E, 2F).

452 **Depletion of Epsins in the Liver Negates the Effects of PCSK9 Overexpression on Atherosclerotic**
453 **Lesion Formation, Macrophage Accumulation, and Plasma Lipid Levels.**

454 As overexpression of PCSK9 promotes atherosclerosis and elevates plasma lipids[13], we further explored
455 the role of hepatic epsins in lipoprotein metabolism and atherosclerosis by employing PCSK9-AAV8-
456 induced Liver-DKO mice and compared their phenotypic outcomes with PCSK9-AAV8-injected WT
457 controls. Mean plasma cholesterol and triglyceride (TG) levels showed striking 66% and 63% decreases
458 resulting from loss of hepatic epsins in mice injected with PCSK9-AAV8 ($2x10^{11}$ genomes) and fed a WD
459 for 20 weeks (Figure S7A). In addition, low-density lipoprotein cholesterol (LDL-C) levels were reduced
460 by 75% in 20 weeks WD-fed Liver-DKO mice after PCSK9-AAV8 injection (Figure S7A). Importantly,
461 PCSK9-AAV8-induced Liver-DKO mice exhibited a 91% reduction in *en face* aortic lesion areas and a
462 92% reduction in lesions of the aortic roots compared with WT controls injected with PCSK9-AAV8 after
463 20 weeks WD treatment (Figure S7B, S7C). In addition, we found markedly attenuated CD68 expression
464 in the aortas in PCSK9-AAV8-injected Liver-DKO mice compared with PCSK9-AAV8-injected WT
465 controls (Figure S7D). Furthermore, the protein levels of α-SMA were markedly increased in the aortas
466 of in PCSK9-AAV8-injected Liver-DKO mice versus PCSK9-AAV8-injected WT controls (Figure S7D).
467 Importantly, the protein levels of the inflammatory endothelial cell adhesion molecules, such as ICAM-1
468 and P-Selectin, in the endothelial layer of aortas in PCSK9-AAV8-induced Liver-DKO mice (Figure S7E,
469 S7F).

470 **Effects of Hepatic Deletion of Epsins 1 and 2 on Alb^{hi} and Ldlr^{hi} Hepatocyte Subpopulations and**
471 **Lipoprotein Clearance Gene Expression**

472 We show that deletion of Epsins1/2 markedly decreased plasma cholesterol and triglyceride. Therefore,
473 we performed single-cell RNA sequencing on liver tissue derived from WD-fed ApoE$^{-/-}$ and ApoE$^{-/-}$
474 /Liver-DKO mice to investigate the underlying mechanisms of the observed phenotypic changes (Figure
475 S8A). The UMAP visualization revealed six different cell types based on the expression patterns of cell
476 type-specific marker genes in the livers (Figure S8B, S8C). Analysis of the hepatocyte data revealed four
477 distinct hepatocyte populations (Figure 3A, 3B, Figures S8B-8D), including HC1 Alb^{hi}, HC2 Alb^{hi}, HC3
478 Alb^{hi} and HC Ldlr^{hi}, which are characterized by the expression levels of both *Alb* and *Ldlr* genes in
479 hepatocytes. The expression of *Ldlr* gene is elevated from HC1 Alb^{hi} towards HC3 Alb^{hi}, while with their
480 lower *Ldlr* expression level compared with HC Ldlr^{hi}. Notably, the proportion of Ldlr^{hi} hepatocytes
481 increased by 59%, and the total proportions of HC2 Alb^{hi} and HC3 Alb^{hi} hepatocytes decreased by 25%
482 and 20%, respectively, in ApoE$^{-/-}$/Liver-DKO mice compared with the ApoE$^{-/-}$ controls (Figure 3B).

483 Hepatocyte-derived data analysis revealed upregulated pathways or genes of LDL particle clearance and
484 downregulated pathways genes of hepatic lipogenesis and plasma lipoprotein particle assembly in
485 different types of hepatocytes in ApoE$^{-/-}$/Liver-DKO mice compared with the ApoE$^{-/-}$ controls (Figure 3C-
486 3E), e.g., *Ldlr*, suggesting improved LDL-C clearance in the absence of hepatic epsins. Consistent with
487 the increased number of Ldlr^{hi} hepatocytes, there was overall elevated Ldlr expression in the livers from
488 ApoE$^{-/-}$/Liver-DKO versus ApoE$^{-/-}$ mice as measured by both single-cell analysis and real-time
489 quantitative PCR (Figure 3F). The hepatocyte subpopulations, particularly the Ldlr^{hi} and HC3 Alb^{hi}
490 hepatocytes exhibited increased Ldlr expression (Figure 3G). Intriguingly, RNA velocity analysis
491 supported an increased propensity for Alb^{hi} hepatocyte differentiation towards Ldlr^{hi} hepatocytes in the
492 absence of hepatic epsins (Figure 3H). Importantly, we found elevated coronary artery disease (CAD)
493 protective scores from Alb^{hi} hepatocytes towards Ldlr^{hi} hepatocytes that are positively associated with
494 Ldlr expression (Figures 3G, 3H, 3I).

495 The livers from ApoE$^{-/-}$/Liver-DKO mice exhibited elevated expression of other genes related to
496 LDL/VLDL particle clearance including the VLDLr and Lrp1 (Figure 3C, 3D, Figure S9A). Importantly,
497 the ApoE$^{-/-}$/Liver-DKO mouse livers exhibited increased gene expression of proteins relevant to hepatic
498 HDL cholesterol uptake including Scarb1 and LIPG[30] (Figure 3C, 3D, Figure S9A). In addition, other
499 genes operating in lipoprotein metabolism such as apoC3, apoC2, apoM, and LCAT were significantly
500 downregulated in ApoE$^{-/-}$/Liver-DKO hepatocytes (Figure 3C, 3E, Figure S9B).

501 We examined the relationship between Epsins1/2 expression and the protein levels of Ldlr in WT
502 hepatocytes (Figures 4A-4D). Immunofluorescence and western blotting analyses of the effects of
503 Epsins1/2 expression on Ldlr receptor levels in hepatocytes from Liver-DKO versus WT mice consuming
504 a chow diet revealed modest increases in Ldlr protein (Figure 4A,4B). In contrast, the hepatocytes from
505 Liver-DKO versus WT mice consuming a western diet had markedly increased Ldlr levels (Figures
506 4C,4D) that was likely due to the substantial upregulation of both Epsin1 and Epsin 2 in hepatocytes from
507 WT mice consuming a western versus a chow diet (Figures 4E,4F). As apoE accelerates LDL/VLDL
508 uptake via LDLr, VLDLr, Lrp1, and SR-BI[31,32],we examined the effects of hepatic deletion of Epsins1/2
509 on apoE levels in WT mice and found that deletion of hepatic Epsins1/2 markedly increased hepatocyte
510 apoE protein levels (Figures 4G,4H). In addition, both single cell and real-time quantitative PCR analyses
511 revealed that deletion of Epsins1/2 remarkably increased expression of the apoAIV gene in hepatocytes

512 from ApoE$^{-/-}$/Liver-DKO versus ApoE$^{-/-}$ mice (Figures 4I), which is highly relevant as studies have shown
513 that apoAIV facilitates LDL clearance as well as reduces liver fat and gluconeogenesis [33-35]. Indeed,
514 deletion of hepatic Epsins1/2 increased the expression of apoAIV in all Alb^{hi} hepatocyte populations
515 (Figure S9C). Studies with hepatocytes from Liver-DKO versus WT mice confirmed a marked increase
516 in apoAIV protein (Figures 4J, 4K).

517 **Decreased Hepatic Lipogenesis and Strengthened Glycogen Biosynthesis in the Livers of Hepatic**
518 **Epsin1/2 Deficient Mice**

519 A closer examination by single cell or real-time quantitative PCR analysis of the effects of hepatic
520 Epsins1/2 deletion on lipogenesis in ApoE$^{-/-}$ mice demonstrates that the expression of genes known to
521 suppress lipogenesis including Hnf4α, Sdc4, Rorα, LIPA, and PPARα (Figures 5A, Figures S9A, S10A,
522 S10C) were markedly increased in livers of ApoE$^{-/-}$/Liver-DKO versus ApoE$^{-/-}$ mice. Correspondingly,
523 detailed analyses revealed upregulated *Ror*α- (i.e., DHCR24) and *Sdc4*- (Fn1) associated anti-lipogenic
524 signaling pathways in ApoE$^{-/-}$ /Liver-DKO mice (Figure S10A)[36]. Importantly, ApoE$^{-/-}$/Liver-DKO versus
525 ApoE$^{-/-}$ mouse livers exhibited diminished mRNA levels of genes that enhance hepatic lipogenesis
526 including *Acaca*, *Scd1*, *Acly*, *Hmgcr,* and *Fasn* (Figures 5B-5C). In addition, the *Scd1* and *Acaca* mRNA
527 levels decreased across all hepatocyte subpopulations (Figure S9C, Figure 5B). Furthermore, there was
528 corresponding downregulation of prolipogenic Ppia-Bsg signaling pathway (Figures S10B). Importantly,
529 western blotting and immunofluorescence analyses demonstrate that the levels of the fatty acid and
530 cholesterol synthetic enzymes, Fasn and Hmgcr, were decreased in the livers of Liver-DKO versus WT
531 mice (Figures 5D-5F). It is also worth noting that some genes linked to the suppression of lipogenesis
532 such as *Nr1h4* and apoM were downregulated in ApoE$^{-/-}$/Liver-DKO versus ApoE$^{-/-}$ mouse livers [37]
533 (Figure S9B, S10B). However, the overall effect of hepatic Epsins1/2 deletion was to markedly reduce
534 liver fat as demonstrated by decreased Oil-Red-O staining of livers from ApoE$^{-/-}$/Liver-DKO versus ApoE^{-}
535 $^{/-}$ mice fed a western diet (Figure 5G).

536 Cell-cell communication analysis using the MEBOCOST algorithm[25] showed enhanced communication
537 mediated by the cholesterol/Ldlr pathway in Ldlr^{hi} hepatocytes in ApoE$^{-/-}$/Liver-DKO mice (Figure S10C,
538 S10D) and resulted in lowered mean abundance of cholesterol in ApoE$^{-/-}$/Liver-DKO mice (Figure S10E).
539 Interestingly, single cell and real-time quantitative PCR analyses also revealed enhanced expression of
540 key genes that facilitate hepatic glycogenesis including Gck, Gys2, and Pgm1 in livers of ApoE$^{-/-}$/Liver-
541 DKO versus ApoE$^{-/-}$ mice (Figures 5H, 5I). Intriguingly, the expression of glycogenesis genes (Pgm1 and
542 Ugp2) was relatively more abundant in Ldlr^{hi} and HC3 Alb^{hi} versus HC1 Alb^{hi} and HC2 Alb^{hi} hepatocyte
543 (Figure S9C). Importantly, we observed a strengthened abundance of uridine diphosphate glucose (UDPG)
544 as an intermediate metabolite for glycogenesis in Ldlr^{hi} hepatocytes in ApoE$^{-/-}$/Liver-DKO mice (Figure
545 S10E), which is consistent with elevated glycogenesis gene expression in the livers of ApoE$^{-/-}$/Liver-DKO
546 mice. Indeed, Periodic acid-Schiff's staining of livers in WT and Liver-DKO mice revealed a 39%
547 increase in mean glycogen-stained areas in Liver-DKO mice compared with WT controls (Figure 5J).
548 Overall, our data suggest that Alb^{hi} hepatocytes are prone to lipogenesis in the liver, while Ldlr^{hi}
549 hepatocytes prefer glycogenesis, and that increased Epsins1/2 expression markedly impacts these
550 processes in part by decreasing the propensity for hepatocyte conversion to Ldlr^{hi} cells.

551 **LDLR is Resistant to PCSK9-induced Proteasomal Degradation, Resulting in Elevated LDL Uptake**
552 **in Liver-DKO mice, and LDLR Directly Binds to Epsin1 UIM Domain.**

553 We show that deletion of hepatic Epsins dramatically increases Ldlr protein levels (Figures 4A-4D) in
554 comparison to Ldlr gene expression (Figures 3F-3G) suggesting that the Epsins impact Ldlr
555 posttranslationally. As epsins are ubiquitin-binding endocytic adaptors, we hypothesized that epsins are
556 required for PCSK9-mediated LDLR degradation. Indeed, western blot (WB) analyses of liver tissue
557 harvested from WT and Liver-DKO mice injected with PCSK9-AAV8 ($2x10^{11}$ genomes) revealed that
558 the LDLR was markedly degraded by PCSK9 administration in WT mice, but not in the livers of Liver-
559 DKO mice, with 3.2-fold more hepatic LDLR protein levels in Liver-DKO mice compared with WT
560 controls (Figure 6A). In addition to liver tissue lysate analysis, we also performed WB analysis of lysates
561 from primary hepatocytes isolated from WT and Liver-DKO mice, treated with PCSK9, cycloheximide
562 (CHX) or MG132. We found PCSK9-induced LDLR degradation occurred independent of new protein
563 synthesis (in the presence of CHX) but was blocked by either loss of epsins or the proteasomal inhibitor
564 MG132 (Figure 6B). The protein levels of LDLR were quantified, with significantly higher LDLR
565 expression in the hepatocytes from Liver-DKO mice either with or without MG132 treatment (Figure 6B).

566 Next, we examined the effects of Epsin1/2 expression on the uptake of DiI-LDL by fluorescence
567 spectrophotometer (Figure 6C) or by confocal microscopy analyses (Figure 6D). There was a 31%
568 increase in mean DiI-LDL uptake in Liver-DKO hepatocytes compared with WT controls (Figure 6C).
569 Consistent with the PCSK9-AAV8-induced LDLR degradation, a 78% decrease DiI-LDL uptake was
570 observed in PCSK9-AAV8-infected WT control hepatocytes versus WT controls (Figure 6C) by
571 spectrophotometer analysis. Moreover, the analysis revealed a 4.9-fold more uptake of DiI-LDL in
572 PCSK9-AAV8-infected Liver-DKO hepatocytes compared with PCSK9-AAV8-infected WT controls
573 (Figure 6C). In addition, confocal microscopy analysis revealed a 51% increase in uptake of DiI-LDL in
574 the hepatocytes in Liver-DKO mice compared with WT controls (Figure 6D). Importantly, confocal
575 microscopy analysis demonstrates that PCSK9-AAV8-infected Liver-DKO hepatocytes had 5.8-fold more
576 uptake of DiI-LDL compared with PCSK9-AAV8-infected WT controls (Figure 6D). Taken together, the
577 hepatocytes in Liver-DKO mice possessed elevated capacity for LDL-C clearance compared with
578 hepatocytes in WT controls.

579 To study the interaction between LDLR and Epsin1, we performed an anti-epsin1 co-immunoprecipitation
580 (co-IPs) analysis. We found LDLR directly binds epsin1 in WT, but not in Liver-DKO primary
581 hepatocytes (Figure 6E). In addition, we discovered that levels of ubiquitinated LDLR were significantly
582 diminished in the liver lysate from Liver-DKO mice by testing ubiquitin expression after LDLR antibody
583 for immunoprecipitation (IP) (Figure 6F). To study which epsin1 motif can bind to LDLR, we transfected
584 different FLAG-tagged epsin1 deletion mutants' plasmids into HepG2 cells (Figure 6G), including
585 pcDNA (empty plasmid), full- length epsin1 plasmid, epsin1-ΔENTH plasmid, epsin1-ΔUIM plasmid,
586 epsin1-DPW/NPF plasmid. Intriguingly, we found that LDLR can specifically bind to both the full-length
587 epsin1 and epsin1-ΔENTH but does not bind to epsin1-ΔUIM and epsin1-DPW/NPF, indicating the
588 epsin1-UIM domain is the binding motif for the interaction between epsin1 and LDLR (Figure 6H).

589 **Inhibited Low-density Lipoprotein Particle Clearance, High-density Lipoprotein Assembly, and**
590 **Glycogen Biosynthesis in the Liver of PCSK9-D374Y Mutant Mice.**

591 Overexpression of PCSK9 induces hyperlipidemia and accelerates atherosclerotic plaque formation[13]. We
592 show that deletion of hepatic Epsins1/2 negates the effects of PCSK9 overexpression on atherosclerosis
593 (Figure 6). In addition, deletion of Epsins 1/2 negates hepatic PCSK9 mediated proteasomal degradation
594 of the LDLr. Therefore, we further explored the underlying hepatic signaling pathways in relation to

595 PCSK9 and Epsins by analyzing liver single-cell RNA-seq data from PCSK9-D374Y mutation mice.
596 PCSK9-D374Y gain-of-function mutant has a markedly increased affinity for LDLR and promotes its
597 degradation[38]. UMAP visualization showed two distinct hepatocyte subclusters between control and
598 PCSK9-D374Y mutant (Figure S11A), namely, HC Alb^{hi} hepatocytes and HC Ldlr^{hi} hepatocytes, based
599 on the expression of hepatocyte markers (Figure S12A). As expected, we identified diminished Ldlr
600 expression in all hepatocytes in PCSK9-D374Y mutant (Figure S11B, S11K). Furthermore, we discovered
601 elevated epsin1 expression in all hepatocytes in PCSK9-D374Y mutant (Figure S11C). Subsequent
602 analyses revealed the downregulated pathways of low-density lipoprotein particle clearance and the
603 upregulated pathways of the glycolytic process in PCSK9-D374Y mutant (Figure S11D-S11F, S13A,
604 S13B). Moreover, we found elevated expression of lipogenic genes, e.g., *Acly*, *Fasn*, and diminished
605 expression of glycogenic genes, e.g., *Gys2*, *Ugp2*, in PCSK9-D374Y mutant (Figure S12E). Importantly,
606 almost all the apolipoprotein genes and genes that control HDL assembly (*Abca1* and *Apoa1*), cholesterol
607 efflux (*Apoa1*, *Apoa2* and *Apoa4*) and the final step of reverse cholesterol transport (*Abcg5*, *Abcg8*) are
608 dramatically inhibited in PCSK9-D374Y mutant (Figure S12C, Figure S12D), implying diminished HDL
609 assembly and curtailed cholesterol clearance.

610 Further RNA velocity analysis demonstrated an inhibited propensity for hepatocyte differentiation from
611 HC Alb^{hi} hepatocytes towards HC Ldlr^{hi} hepatocytes in the presence of elevated hepatic epsins in PCSK9-
612 D374Y mutant (Figure S11G, Figure S12B). Consequently, we discovered lowered CAD protective scores
613 in both HC Alb^{hi} and HC Ldlr^{hi} hepatocytes in PCSK9-D374Y mutants (Figure S11H). Metabolite
614 analyses using the MEBOCOST algorithm showed weakened communication interactions for
615 cholesterol/Ldlr pathway in all hepatocytes in PCSK9-D374Y mutant (Figure S11I). Subsequently, we
616 found a lowered mean abundance of uridine diphosphate glucose (UDPG) as an intermediate metabolite
617 for glycogenesis in all hepatocytes in PCSK9-D374Y mutant (Figure S11J).

618 **Nanoparticle-mediated Delivery of Epsins siRNAs Potently Inhibits Lesion Development, Reduces**
619 **Foam Cell Formation, and Decreases Cholesterol and TG Levels in ApoE$^{-/-}$ Mice.**

620 To explore the therapeutic potential of targeting hepatic epsins, we employed nanoparticle-encapsulated
621 siRNAs specifically targeting epsins in the liver. Therapeutically, we applied nanoparticles (NPs)
622 encapsulated epsin1 and epsin2 siRNAs (Figure 7A) to inject ApoE $^{-/-}$ mice under WD-treatment. Control
623 siRNA NPs were injected into WD-fed ApoE $^{-/-}$ mice as the control. Western blots of liver lysates isolated
624 from WD-fed ApoE $^{-/-}$ mice (8 weeks) that were treated with control or epsins siRNA NPs revealed
625 dramatically diminished epsin1 and epsin2 protein expression, indicating the high efficiency of epsins
626 siRNA NPs for knockdown of epsin1 and epsin2 proteins (Figure 7B). Mean serum cholesterol and
627 triglyceride (TG) levels showed striking 31% and 22% decreases in epsin1 and epsin2 siRNAs NPs treated
628 WD-fed ApoE $^{-/-}$ mice compared with control siRNA NPs treated WD-fed ApoE $^{-/-}$ mice (Figure 7C,7D).
629 Importantly, epsin1 and epsin2 siRNAs NPs treated WD-fed ApoE $^{-/-}$ mice exhibited a 60% reduction in
630 *en face* aortic lesion areas and a 62% reduction in lesions of the aortic roots compared with control siRNA
631 NPs treated WD-fed ApoE $^{-/-}$ mice (Figure 7E, 7F). In addition, we discovered remarkably diminished
632 mean fluorescence intensity (MFI) of CD68 in epsin1 and epsin2 siRNAs NPs treated WD-fed ApoE $^{-/-}$
633 mice compared with control siRNA NPs treated WD-fed ApoE $^{-/-}$ mice, indicating lowered macrophage
634 accumulation in the atherosclerotic lesions in epsin1 and epsin2 siRNAs NPs treated ApoE $^{-/-}$ mice (Figure
635 7G). These findings suggest that targeting liver epsins presents a novel and promising therapeutic strategy
636 for the treatment of atherosclerosis.

637 **DISCUSSION**

638 In this study, we found that epsin1 and epsin2 expression dramatically increased by 98% and 68%,
639 respectively, in the aortas in ASCVD patients compared with healthy controls (Figure S3A-S3C),
640 suggesting the expression of epsin1 and epsin2 is positively correlated with atherosclerosis. Our previous
641 studies have elucidated an atheroprone function of epsins in endothelial cells[4], macrophages[16,17], and
642 vascular smooth muscle cells[39] due to significantly elevated inflammation in the atherosclerotic plaque.
643 However, atherosclerosis is initiated by the abnormal accumulation of LDL-C in the subendothelial layer
644 of the arterial wall due to hyperlipidemia[40]. The liver is the central organ for the control of cholesterol
645 homeostasis[41] and controls blood levels of LDL-C by regulating LDLR expression, which mediates
646 hepatic clearance of circulating LDL-C. Lowering LDL-C remains the most effective approach for
647 prevention of ASCVD[12]. PCSK9 is dominantly expressed in the liver, and PCSK9 binds to LDLR and
648 targets the LDLR for degradation[42]. Monoclonal antibody and interference-RNA therapies that target
649 PCSK9 are extremely effective in reducing circulating levels of LDL-C [9,10]; however, the mechanistic
650 details of PCSK9-mediated LDLR degradation remain insufficiently understood.

651 In this study, our scRNA-seq data analyses in the context of aortas revealed 22% decrease in cell
652 proportion of macrophages in the aortas in ApoE$^{-/-}$/Liver-DKO mice strongly supports that attenuated
653 inflammation ameliorates atherosclerosis[43] (Figure S4C, Figure 2A). Furthermore, a 45% decrease in cell
654 proportion of fibroblasts in the aortas in ApoE$^{-/-}$/Liver-DKO mice as compelling evidence of reduced
655 collagen accumulation that is consistent with the dramatic reduction in atherosclerotic lesion size[44] (Figure
656 S4C, Figure 2D). In addition, a 91% increase in endothelial cell proportion in the aortas in ApoE$^{-/-}$/Liver-
657 DKO mice is consistent with the upregulation of endothelial cell differentiation and downregulation of
658 endothelial cell activation and migration and downregulated pathways involved in inflammation in
659 macrophages likely reduce the progression of atherosclerosis[45,46] (Figure S4C, Figure S5A, Figure 1E-
660 1G). Notably, a 63% increase in vascular smooth muscle cells (VSMCs) proportion in the aortas in ApoE^{-}
661 $^{/-}$/Liver-DKO mice with substantially elevated expression of markers of the contractile VSMCs that
662 inhibited phenotypic switching into synthetic VSMCs that impeded atherosclerosis[47] (Figure S4C, S4D,
663 Figure 2A, 2D). Hence, the markedly impeded atheroma in the aortas in ApoE$^{-/-}$ /Liver-DKO mice is
664 partially attributed to increased cell proportion of healthy endothelial cells, reduced cell proportion of
665 inflammatory macrophages, attenuated extracellular matrix and collagen production, and the enrichment
666 of contractile VSMCs.

667 Hepatic loss of epsins resulted in lower plasma cholesterol and triglyceride levels in both WD-fed ApoE^{-}
668 $^{/-}$/Liver-DKO mice and PCSK9-AAV8 injected Liver-DKO mice compared with their controls (Figure 1A,
669 Figure S7A). Importantly, the plasma cholesterol and triglyceride levels are not impacted by epsins
670 deficiency cell types, including endothelial cells, macrophages, and vascular smooth muscle cells[4,16,17,39].
671 Taken together, these findings indicate that epsins in the hepatocytes participate in lipoprotein metabolism.
672 The liver is the main organ that regulates circulating LDL-C levels, in large part by regulating LDLR-
673 mediated LDL-C clearance[41]. In this study, we identified higher LDLR expression in the livers of Liver-
674 DKO mice than WT controls (Figure 4A-4D). Our single-cell RNA sequencing data showed upregulated
675 pathway of low-density lipoprotein particle clearance and downregulated pathway of plasma lipoprotein
676 particle assembly in the hepatocytes in ApoE$^{-/-}$/Liver-DKO mice (Figure 3C-3E), which is consistent with
677 their reduced plasma cholesterol and triglycerides. Subsequently, we exhibited evidence of enhanced
678 communication score between LDLR and cholesterol in the hepatocytes in ApoE$^{-/-}$/Liver-DKO mice by
679 MEBOCOST analysis (Figure S10C-S10E), indicating boosted capacity of low-density lipoprotein

680 cholesterol (LDL-C) clearance by LDLR in ApoE$^{-/-}$/Liver-DKO mice. In addition, hepatic Epsins
681 deficiency impacted lipogenesis, which is substantiated by markedly diminished expression of genes and
682 proteins that are involved in lipogenesis in ApoE$^{-/-}$/Liver-DKO mice (Figure 5A-5F). Furthermore,
683 hepatocyte Epsins deficiency was associated with increased differentiation of Alb^{hi} hepatocytes towards
684 Ldlr^{hi} hepatocytes in ApoE$^{-/-}$/Liver-DKO mice compared with ApoE$^{-/-}$ controls (Figure 3H), resulting in a
685 59% increase in the proportion of Ldlr^{hi} hepatocytes (Figure 3B). Consequently, we found a dramatically
686 reduced atherosclerotic lesion area in ApoE$^{-/-}$/Liver-DKO mice compared with ApoE$^{-/-}$ controls (Figure
687 1B, 1C). In addition to enhanced LDL-C clearance, we found the elevated UDPG metabolite level further
688 promotes hepatic glycogenesis in Ldlr^{hi} hepatocytes in ApoE$^{-/-}$/Liver-DKO mice (Figure S10E). Chen *et*
689 *al.* recently reported that hepatic glycogenesis inhibits lipogenesis[48]. Accordingly, the enhanced glycogen
690 level in the liver inhibits fatty acid synthesis that could also contribute to reduced cholesterol and
691 triglyceride in plasma in ApoE$^{-/-}$ /Liver-DKO mice.

692 Currently, no single-cell transcriptomics study of human livers from patients in the context of coronary
693 artery disease is available, and most single-cell RNA sequencing studies for patients in the context of
694 coronary artery disease are for exploring the transcriptome differences of atherosclerotic plaques[49,50].
695 Therefore, it is impossible to compare our liver single-cell transcriptome data with counterparts from
696 coronary artery disease patients. However, a recently published article explored the liver transcriptome by
697 single-cell RNA sequencing for PCSK9-D374Y mice with an emphasis on the analysis of Kupffer cells[51];
698 this dataset empowered us to analyze the heterogeneity of hepatocytes in the livers between PCSK9-
699 D374Y mice and controls. The PCSK9-D374Y mutation potently elevates the affinity between PCSK9
700 and LDLR interaction, and further promotes the degradation of the LDLR[52]. In this study, we reanalyzed
701 the liver single-cell transcriptome dataset by emphasizing the analysis on hepatocytes in PCSK9-D374Y
702 mice[51]. Intriguingly, we found an inhibited propensity for differentiation of Alb^{hi} hepatocytes towards
703 Ldlr^{hi} hepatocytes in PCSK9-D374Y mice compared with controls that cause weakened glycogenesis,
704 enhanced lipogenesis, and lowered CAD protective score (Figure S11G, S11H, Figure S12E).
705 Accordingly, there are a number of phenotypic similarities between WD-fed PCSK9-AAV8-injected
706 control mice and WD-fed ApoE$^{-/-}$ mice (Figure 1A-1C, Figure S7A-S7C). Mechanistically, we identified
707 an elevated epsin1 expression level by 69% in Ldlr^{hi} hepatocytes that might cause impeded clearance of
708 LDL particles and VLDL particles by curtailment of LDLR expression level by 72% in Ldlr^{hi} hepatocytes
709 in PCSK9-D374Y mice (Figure S11B, S11C). Subsequently, MEBOCOST analysis revealed a diminished
710 communication score between LDLR and cholesterol in the hepatocytes in PCSK9-D374Y mice (Figure
711 S11I-S11K), which is compatible with serum cholesterol accumulation due to reduced hepatic LDLR
712 levels in PCSK9-D374Y mice[53]. Similar to the phenotype in ApoE$^{-/-}$ mice, decreased UDPG expression
713 in hepatocytes in PCSK9-D374Y mice (Figure S11J) and curbed glycogenesis further contribute to
714 elevated lipogenesis[48]. In summary, two different mouse models of atherosclerosis, ApoE$^{-/-}$ and PCSK9-
715 D374Y mice, shared similar hepatocyte heterogeneity and common pathological signaling pathways for
716 inducing atherosclerosis or dyslipidemia, which might be highly correlated with epsins-mediated LDLR
717 degradation in the liver.

718 We demonstrated how liver epsins regulate PCSK9-mediated LDLR degradation in the liver (Figure 8).
719 In liver epsins-deficient mice, LDLR expression is markedly increased in the membrane of hepatocytes,
720 promoting enhanced LDL-C clearance (Figure 8). PCSK9 protein mediates LDLR protein degradation,
721 reducing hepatic uptake of LDL-C[54]. In this study, when PCSK9 is overexpressed by injection of PCSK9-
722 AAV8 into WT controls and Liver-DKO mice, the LDLR is remarkably degraded in WT controls;
723 however, the degradation of LDLR is significantly inhibited in Liver-DKO mice, with a 2.2-fold increase

724 in LDLR expression level (Figure 6A), which demonstrates that liver epsins are essential for PCSK9-
725 mediated LDLR degradation. In studies of primary hepatocytes isolated from WT and Liver-DKO mice
726 were treated with PCSK9, cycloheximide (CHX) or proteasomal inhibitor MG132, we discovered that
727 PCSK9-induced LDLR degradation occurred independent of new protein synthesis, and LDLR
728 degradation was blocked by loss of epsins in the liver (Figure 6B). Importantly, 3.9- or 4.8-fold increase
729 in the uptake of DiI-LDL in mean by the PCSK9-treated hepatocytes in Liver-DKO mice compared with
730 PCSK9-treated WT controls is associated with the inhibition of PCSK9-mediated degradation of LDLR,
731 which is consistent with elevated capacity for LDL particle clearance identified by single cell RNA-
732 sequencing (Figure 6C, 6D). Subsequently, we discovered that epsin1 can directly bind to LDLR protein,
733 which further triggers its degradation (Figure 6E). Our previous studies revealed that epsins are critical
734 adaptor proteins that are involved in endocytosis[15,18,55]. To explore which motifs in epsin1 can specifically
735 bind to LDLR, such as ENTH, UIM, DPW and NPF (Figure 6G), FLAG-tagged epsin1 deletion mutants'
736 plasmids have been transfected into HepG2 cells. Importantly, the LDLR binds specifically to the
737 ubiquitin-interacting motif (UIM) motif but does not bind to other motifs (Figure 6H). The UIM in epsins
738 facilitates ubiquitination-mediated protein degradation[56]. Consequently, diminished LDLR expression in
739 the liver is due to the interaction between LDLR and the epsin1 UIM motif, which activates ubiquitination
740 of LDLR, facilitating its degradation in WT controls, but not in Liver-DKO mice. In addition, the
741 ubiquitinated LDLR was decreased in the liver lysate from Liver-DKO mice; consequently, LDLR
742 expression was increased in the input lysate in Liver-DKO mice compared with WT controls (Figure 6F),
743 demonstrating that the loss of epsins enhances the stability of LDLR. MG132 proteasome inhibitors
744 blocked the degradation of LDLR by inhibition of ubiquitination[57]. In summary, epsins play gatekeeping
745 roles in the PCSK9-mediated ubiquitination-driven LDLR degradation mediated by the interaction
746 between epsin1 UIM motif and LDLR. Therefore, the liver epsins are potentially attractive targets for the
747 treatment of dyslipidemia and atherosclerosis by protecting hepatic LDLRs from degradation.

748 The liver is the primary organ for lipid nanoparticle accumulation following intravenous administration[58],
749 and lipid nanoparticle-mediated RNAs or siRNAs delivery holds great potential for treating liver
750 diseases[59,60]. In this study, targeting liver epsins with lipid nanoparticle encapsulated siRNAs was highly
751 efficacious at inhibiting dyslipidemia and impeding atherosclerosis. We discovered notably 31% reduced
752 cholesterol and a 22% reduction of triglyceride levels in the epsin1 and epsin2 siRNA NPs injected group
753 compared with the control NPs group (Figure 7C, 7D). In addition, we found a 60% reduction in *en face*
754 aortic lesion areas and a 62% reduction in lesions of aortic roots in epsin1 and epsin2 siRNA NPs-injected
755 mice compared with the control NPs group (Figure 7E, 7F). These results support hepatic epsins as novel
756 therapeutic targets for the treatment of hyperlipidemia and the prevention of atherosclerosis.

757 **Conclusions**

758 Here, we discovered markedly diminished atherosclerotic lesions and reduced serum cholesterol levels in
759 both WD-fed ApoE$^{-/-}$/Liver-DKO mice and WD-fed PCSK9-AAV8 injected Liver-DKO mice. We
760 demonstrated that the loss of epsins in the liver inhibits atherosclerosis by enhancing LDLR stability.
761 Mechanistically, epsins bind LDLR via the ubiquitin-interacting motif (UIM), and PCSK9-triggered
762 LDLR degradation was abolished by depletion of epsins, dramatically lowering plasma cholesterol levels
763 and preventing atheroma progression. Additionally, in the liver, the increased propensity of hepatocyte
764 differentiation from Alb^{hi} towards Ldlr^{hi} hepatocytes in the absence of hepatic epsins inhibits atheroma
765 progression by enhancing LDL-C clearance. Targeting liver epsins with nanoparticle-encapsulated epsins
766 siRNAs, was highly efficacious at reducing plasma lipid levels and impeding atherosclerosis. These

767 findings provide us with a novel therapeutic strategy for the treatment of hyperlipidemia to combat
768 atherosclerosis.

769 **Acknowledgments**

770 We thank Dr. Jinjun Shi's lab at Brigham and Women's Hospital for the synthesis of epsin1 and espin2
771 siRNA nanoparticles. We thank the imaging core at Boston Children's Hospital, and the Biopolymers
772 Facility at Harvard Medical School for quality control analysis of DNA libraries prepared for scRNA-
773 sequencing. We thank the animal core facility for the daily maintenance at Boston Children's Hospital.

774 **Sources of Funding**

775 This work was supported in part by NIH grants Nos. R01HL137229, R01HL1563626, R01HL158097,
776 and R01HL158097 to HC.

777 **Author contributions**

778 B.Z., K.C., and H.C. conceived and designed the experiments. B.Z., K.C. performed most of the
779 experiments. B.W. contributed to animal experiments. K.G. and K.C. analyzed the scRNA-seq data and
780 performed bioinformatic work. M.M. and S.S. measured plasma cholesterol and triglycerides. S.W.
781 performed the mouse genotyping and colony maintenance. B.Z., K.G., K.L., D.W., S.B., P.G.Y., D.B.C.,
782 M.F.L, W.W, C.A.B, K.C. and H.C. wrote and edited the article. All the authors reviewed and provided
783 feedback on the article.

784 **Disclosure**

785 None.

786 **Supplemental Material**

787 WB Raw Films

788 Major Resources Table

789 Nonstandard Abbreviations and Acronyms

790 Clinical Perspective

791 Supplemental Figure 1-14

792 Table S1-S2

References

1 Libby, P. *et al.* Atherosclerosis. *Nat Rev Dis Primers* **5**, 56, doi:10.1038/s41572-019-0106-z (2019).

2 Pahwa, R. & Jialal, I. in *StatPearls* (2024).

3 Zhu, B. *et al.* Two sides of the same coin: Non-alcoholic fatty liver disease and atherosclerosis. *Vascul Pharmacol* **154**, 107249, doi:10.1016/j.vph.2023.107249 (2024).

4 Dong, Y. *et al.* Epsin-mediated degradation of IP3R1 fuels atherosclerosis. *Nat Commun* **11**, 3984, doi:10.1038/s41467-020-17848-4 (2020).

5 Benito-Vicente, A. *et al.* Familial Hypercholesterolemia: The Most Frequent Cholesterol Metabolism Disorder Caused Disease. *Int J Mol Sci* **19**, doi:10.3390/ijms19113426 (2018).

6 Schaefer, J. R., Kurt, B., Sattler, A., Klaus, G. & Soufi, M. Pharmacogenetic aspects in familial hypercholesterolemia with the special focus on FHMarburg (FH p.W556R). *Clin Res Cardiol Suppl* **7**, 2-6, doi:10.1007/s11789-012-0041-y (2012).

7 Goldstein, J. L. & Brown, M. S. The LDL receptor. *Arterioscler Thromb Vasc Biol* **29**, 431-438, doi:10.1161/ATVBAHA.108.179564 (2009).

8 Bao, X. *et al.* Targeting proprotein convertase subtilisin/kexin type 9 (PCSK9): from bench to bedside. *Signal Transduct Target Ther* **9**, 13, doi:10.1038/s41392-023-01690-3 (2024).

9 Robinson, J. G. *et al.* Efficacy and safety of alirocumab in reducing lipids and cardiovascular events. *N Engl J Med* **372**, 1489-1499, doi:10.1056/NEJMoa1501031 (2015).

10 Sabatine, M. S. *et al.* Evolocumab and Clinical Outcomes in Patients with Cardiovascular Disease. *N Engl J Med* **376**, 1713-1722, doi:10.1056/NEJMoa1615664 (2017).

11 Lu, R. *et al.* Spontaneous severe hypercholesterolemia and atherosclerosis lesions in rabbits with deficiency of low-density lipoprotein receptor (LDLR) on exon 7. *EBioMedicine* **36**, 29-38, doi:10.1016/j.ebiom.2018.09.020 (2018).

12 Zhao, H. *et al.* In Vivo AAV-CRISPR/Cas9-Mediated Gene Editing Ameliorates Atherosclerosis in Familial Hypercholesterolemia. *Circulation* **141**, 67-79, doi:10.1161/CIRCULATIONAHA.119.042476 (2020).

13 Keeter, W. C., Carter, N. M., Nadler, J. L. & Galkina, E. V. The AAV-PCSK9 murine model of atherosclerosis and metabolic dysfunction. *Eur Heart J Open* **2**, oeac028, doi:10.1093/ehjopen/oeac028 (2022).

14 Lee, R. G. *et al.* Efficacy and Safety of an Investigational Single-Course CRISPR Base-Editing Therapy Targeting PCSK9 in Nonhuman Primate and Mouse Models. *Circulation* **147**, 242-253, doi:10.1161/CIRCULATIONAHA.122.062132 (2023).

15 Chen, H. *et al.* Epsin is an EH-domain-binding protein implicated in clathrin-mediated endocytosis. *Nature* **394**, 793-797, doi:10.1038/29555 (1998).

16 Brophy, M. L. *et al.* Myeloid-Specific Deletion of Epsins 1 and 2 Reduces Atherosclerosis by Preventing LRP-1 Downregulation. *Circ Res* **124**, e6-e19, doi:10.1161/CIRCRESAHA.118.313028 (2019).

17 Cui, K. *et al.* Epsin Nanotherapy Regulates Cholesterol Transport to Fortify Atheroma Regression. *Circ Res* **132**, e22-e42, doi:10.1161/CIRCRESAHA.122.321723 (2023).

18 Chen, H. *et al.* Embryonic arrest at midgestation and disruption of Notch signaling produced by the absence of both epsin 1 and epsin 2 in mice. *Proc Natl Acad Sci U S A* **106**, 13838-13843, doi:10.1073/pnas.0907008106 (2009).
19 Dong, Y. *et al.* Targeting Epsins to Inhibit Fibroblast Growth Factor Signaling While Potentiating Transforming Growth Factor-beta Signaling Constrains Endothelial-to-Mesenchymal Transition in Atherosclerosis. *Circulation* **147**, 669-685, doi:10.1161/CIRCULATIONAHA.122.063075 (2023).
20 Hao, Y. *et al.* Integrated analysis of multimodal single-cell data. *Cell* **184**, 3573-3587 e3529, doi:10.1016/j.cell.2021.04.048 (2021).
21 Franzen, O., Gan, L. M. & Bjorkegren, J. L. M. PanglaoDB: a web server for exploration of mouse and human single-cell RNA sequencing data. *Database (Oxford)* **2019**, doi:10.1093/database/baz046 (2019).
22 Jiang, S. *et al.* Cell Taxonomy: a curated repository of cell types with multifaceted characterization. *Nucleic Acids Res* **51**, D853-D860, doi:10.1093/nar/gkac816 (2023).
23 Li, M. *et al.* DISCO: a database of Deeply Integrated human Single-Cell Omics data. *Nucleic Acids Res* **50**, D596-D602, doi:10.1093/nar/gkab1020 (2022).
24 Lange, M. *et al.* CellRank for directed single-cell fate mapping. *Nat Methods* **19**, 159-170, doi:10.1038/s41592-021-01346-6 (2022).
25 Rongbin Zheng, Y. Z., Tadataka Tsuji, Xinlei Gao, Allon Wagner, Nir Yosef, Hong Chen, Lili Zhang, Yu-Hua Tseng, Kaifu Chen. MEBOCOST: Metabolite-mediated Cell Communication Modeling by Single Cell Transcriptome. doi: 10.1101/2022.05.30.494067 (2022).
26 Jin, S. *et al.* Inference and analysis of cell-cell communication using CellChat. *Nat Commun* **12**, 1088, doi:10.1038/s41467-021-21246-9 (2021).
27 Wu, T. *et al.* clusterProfiler 4.0: A universal enrichment tool for interpreting omics data. *Innovation (Camb)* **2**, 100141, doi:10.1016/j.xinn.2021.100141 (2021).
28 Aragam, K. G. *et al.* Discovery and systematic characterization of risk variants and genes for coronary artery disease in over a million participants. *Nat Genet* **54**, 1803-1815, doi:10.1038/s41588-022-01233-6 (2022).
29 Tao, W. *et al.* siRNA nanoparticles targeting CaMKIIgamma in lesional macrophages improve atherosclerotic plaque stability in mice. *Sci Transl Med* **12**, doi:10.1126/scitranslmed.aay1063 (2020).
30 Strauss, J. G. *et al.* Endothelial cell-derived lipase mediates uptake and binding of high-density lipoprotein (HDL) particles and the selective uptake of HDL-associated cholesterol esters independent of its enzymic activity. *Biochem J* **368**, 69-79, doi:10.1042/BJ20020306 (2002).
31 Marais, A. D. Apolipoprotein E in lipoprotein metabolism, health and cardiovascular disease. *Pathology* **51**, 165-176, doi:10.1016/j.pathol.2018.11.002 (2019).
32 Hu, L. *et al.* The hepatic uptake of VLDL in lrp-ldlr-/-vldlr-/- mice is regulated by LPL activity and involves proteoglycans and SR-BI. *J Lipid Res* **49**, 1553-1561, doi:10.1194/jlr.M800130-JLR200 (2008).
33 Li, X. *et al.* Apolipoprotein A-IV reduces hepatic gluconeogenesis through nuclear receptor NR1D1. *J Biol Chem* **289**, 2396-2404, doi:10.1074/jbc.M113.511766 (2014).
34 Kuo, H. N. *et al.* Apolipoprotein A4 Elevates Sympathetic Activity and Thermogenesis in Male Mice. *Nutrients* **15**, doi:10.3390/nu15112486 (2023).

35 Qu, J., Ko, C. W., Tso, P. & Bhargava, A. Apolipoprotein A-IV: A Multifunctional Protein Involved in Protection against Atherosclerosis and Diabetes. *Cells* **8**, doi:10.3390/cells8040319 (2019).
36 Kim, K. *et al.* RORalpha controls hepatic lipid homeostasis via negative regulation of PPARgamma transcriptional network. *Nat Commun* **8**, 162, doi:10.1038/s41467-017-00215-1 (2017).
37 Clifford, B. L. *et al.* FXR activation protects against NAFLD via bile-acid-dependent reductions in lipid absorption. *Cell Metab* **33**, 1671-1684 e1674, doi:10.1016/j.cmet.2021.06.012 (2021).
38 Lagace, T. A. *et al.* Secreted PCSK9 decreases the number of LDL receptors in hepatocytes and in livers of parabiotic mice. *J Clin Invest* **116**, 2995-3005, doi:10.1172/JCI29383 (2006).
39 Beibei Wang, K. C., Bo Zhu, Yunzhou Dong, Donghai Wang, Bandana Singh, Yao Wei Lu, Hao Wu, Sudarshan Bhattacharjee, Eisa-Beygi Shahram, Scott Wong, Douglas B. Cowan, Mulong Du, Hong Chen. Epsins promote atherosclerosis through VSMC phenotypic modulation. doi: 10.1101/2024.01.08.574714 (2024).
40 Linton, M. F. *et al.* in *Endotext* (eds K. R. Feingold *et al.*) (2000).
41 Duan, Y. *et al.* Regulation of cholesterol homeostasis in health and diseases: from mechanisms to targeted therapeutics. *Signal Transduct Target Ther* **7**, 265, doi:10.1038/s41392-022-01125-5 (2022).
42 Lagace, T. A. PCSK9 and LDLR degradation: regulatory mechanisms in circulation and in cells. *Curr Opin Lipidol* **25**, 387-393, doi:10.1097/MOL.0000000000000114 (2014).
43 Kong, P. *et al.* Inflammation and atherosclerosis: signaling pathways and therapeutic intervention. *Signal Transduct Target Ther* **7**, 131, doi:10.1038/s41392-022-00955-7 (2022).
44 Rekhter, M. D. Collagen synthesis in atherosclerosis: too much and not enough. *Cardiovasc Res* **41**, 376-384, doi:10.1016/s0008-6363(98)00321-6 (1999).
45 Davignon, J. & Ganz, P. Role of endothelial dysfunction in atherosclerosis. *Circulation* **109**, III27-32, doi:10.1161/01.CIR.0000131515.03336.f8 (2004).
46 Moore, K. J. & Tabas, I. Macrophages in the pathogenesis of atherosclerosis. *Cell* **145**, 341-355, doi:10.1016/j.cell.2011.04.005 (2011).
47 Bennett, M. R., Sinha, S. & Owens, G. K. Vascular Smooth Muscle Cells in Atherosclerosis. *Circ Res* **118**, 692-702, doi:10.1161/CIRCRESAHA.115.306361 (2016).
48 Chen, J. *et al.* Hepatic glycogenesis antagonizes lipogenesis by blocking S1P via UDPG. *Science* **383**, eadi3332, doi:10.1126/science.adi3332 (2024).
49 Li, Y. *et al.* Single-Cell Transcriptome Analysis Reveals Dynamic Cell Populations and Differential Gene Expression Patterns in Control and Aneurysmal Human Aortic Tissue. *Circulation* **142**, 1374-1388, doi:10.1161/CIRCULATIONAHA.120.046528 (2020).
50 Chou, E. L. *et al.* Aortic Cellular Diversity and Quantitative Genome-Wide Association Study Trait Prioritization Through Single-Nuclear RNA Sequencing of the Aneurysmal Human Aorta. *Arterioscler Thromb Vasc Biol* **42**, 1355-1374, doi:10.1161/ATVBAHA.122.317953 (2022).
51 Di Nunzio, G., Hellberg, S., Zhang, Y. et al. Kupffer cells dictate hepatic responses to the atherogenic dyslipidemic insult. . *Nat Cardiovasc Res* **3**, 356–371, doi: 10.1038/s44161-024-00448-6 (2024).
52 Timms, K. M. *et al.* A mutation in PCSK9 causing autosomal-dominant hypercholesterolemia in a Utah pedigree. *Hum Genet* **114**, 349-353, doi:10.1007/s00439-003-1071-9 (2004).

53 Herbert, B. *et al.* Increased secretion of lipoproteins in transgenic mice expressing human D374Y PCSK9 under physiological genetic control. *Arterioscler Thromb Vasc Biol* **30**, 1333-1339, doi:10.1161/ATVBAHA.110.204040 (2010).

54 Maxwell, K. N., Fisher, E. A. & Breslow, J. L. Overexpression of PCSK9 accelerates the degradation of the LDLR in a post-endoplasmic reticulum compartment. *Proc Natl Acad Sci U S A* **102**, 2069-2074, doi:10.1073/pnas.0409736102 (2005).

55 Chen, H. & De Camilli, P. The association of epsin with ubiquitinated cargo along the endocytic pathway is negatively regulated by its interaction with clathrin. *Proc Natl Acad Sci U S A* **102**, 2766-2771, doi:10.1073/pnas.0409719102 (2005).

56 Oldham, C. E., Mohney, R. P., Miller, S. L., Hanes, R. N. & O'Bryan, J. P. The ubiquitin-interacting motifs target the endocytic adaptor protein epsin for ubiquitination. *Curr Biol* **12**, 1112-1116, doi:10.1016/s0960-9822(02)00900-4 (2002).

57 Yan, H. *et al.* MG132, a proteasome inhibitor, enhances LDL uptake in HepG2 cells in vitro by regulating LDLR and PCSK9 expression. *Acta Pharmacol Sin* **35**, 994-1004, doi:10.1038/aps.2014.52 (2014).

58 Bottger, R. *et al.* Lipid-based nanoparticle technologies for liver targeting. *Adv Drug Deliv Rev* **154-155**, 79-101, doi:10.1016/j.addr.2020.06.017 (2020).

59 Han, X. *et al.* Ligand-tethered lipid nanoparticles for targeted RNA delivery to treat liver fibrosis. *Nat Commun* **14**, 75, doi:10.1038/s41467-022-35637-z (2023).

60 Zhang, J. *et al.* Liver-Targeted siRNA Lipid Nanoparticles Treat Hepatic Cirrhosis by Dual Antifibrotic and Anti-inflammatory Activities. *ACS Nano* **14**, 6305-6322, doi:10.1021/acsnano.0c02633 (2020).

Figure 1

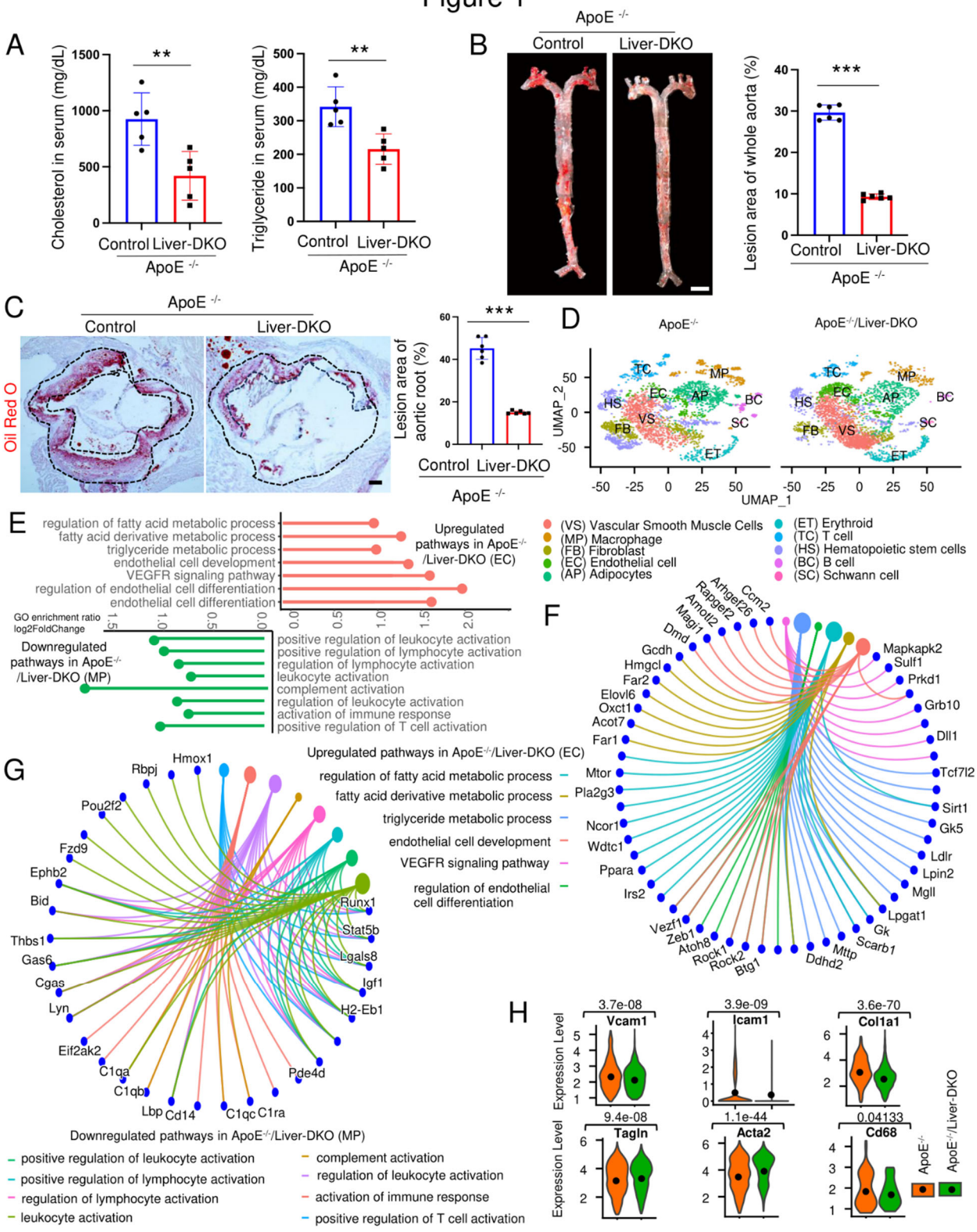
A
Cholesterol in serum (mg/dL)
Triglyceride in serum (mg/dL)
Control
Liver-DKO
ApoE -/-
B
Lesion area of whole aorta (%)
C
Oil Red O
Lesion area of aortic root (%)
D
ApoE-/-
ApoE-/-/Liver-DKO
UMAP_1
UMAP_2
TC
MP
EC
AP
BC
HS
VS
FB
SC
ET
E
Upregulated pathways in ApoE-/-/Liver-DKO (EC)
regulation of fatty acid metabolic process
fatty acid derivative metabolic process
triglyceride metabolic process
endothelial cell development
VEGFR signaling pathway
regulation of endothelial cell differentiation
endothelial cell differentiation
GO enrichment ratio
log2FoldChange
Downregulated pathways in ApoE-/-/Liver-DKO (MP)
positive regulation of leukocyte activation
positive regulation of lymphocyte activation
regulation of lymphocyte activation
leukocyte activation
complement activation
regulation of leukocyte activation
activation of immune response
positive regulation of T cell activation
(VS) Vascular Smooth Muscle Cells
(MP) Macrophage
(FB) Fibroblast
(EC) Endothelial cell
(AP) Adipocytes
(ET) Erythroid
(TC) T cell
(HS) Hematopoietic stem cells
(BC) B cell
(SC) Schwann cell
F
Upregulated pathways in ApoE-/-/Liver-DKO (EC)
regulation of fatty acid metabolic process
fatty acid derivative metabolic process
triglyceride metabolic process
endothelial cell development
VEGFR signaling pathway
regulation of endothelial cell differentiation
G
Downregulated pathways in ApoE-/-/Liver-DKO (MP)
positive regulation of leukocyte activation
positive regulation of lymphocyte activation
regulation of lymphocyte activation
leukocyte activation
complement activation
regulation of leukocyte activation
activation of immune response
positive regulation of T cell activation
H
Expression Level
3.7e-08
Vcam1
3.9e-09
Icam1
3.6e-70
Col1a1
9.4e-08
Tagln
1.1e-44
Acta2
0.04133
Cd68
ApoE-/-
ApoE-/-/Liver-DKO

Figure 1: Liver-deficiency of epsins reduces plasma lipids and inhibits atherosclerotic lesion formation by altering the inflammatory cellular landscape of plaques in ApoE$^{-/-}$ mice. A: Serum cholesterol and triglyceride (TG) levels in ApoE$^{-/-}$ and ApoE$^{-/-}$ /Liver-DKO mice after 8 weeks on a WD (n=5, p**<0.01). B: *En face* ORO staining of aortas (left) from ApoE$^{-/-}$ or ApoE$^{-/-}$/Liver-DKO mice fed a WD for 8 weeks, and unpaired t-test (right) for the lesion areas (n=6, ***p< 0.001). Scale bar, 5 mm. C: Aortic roots from WD-fed ApoE$^{-/-}$ or ApoE$^{-/-}$/Liver-DKO mice stained with ORO (left), and unpaired t-test (right) for the lesion areas (right) (n=6, ***p< 0.001). Scale bar, 200 µm. D: UMAP visualization illustrating the heterogeneity of cell populations indicating distinct clustering patterns of Macrophages (MP), Vascular Smooth Muscle Cells (VS), Endothelial Cells (EC) and Fibroblasts (FB) and other cells in ApoE$^{-/-}$/Liver-DKO mice compared to ApoE$^{-/-}$ controls. E: Gene Ontology (GO) analysis showing significantly enriched pathways for the regulation of triglyceride and fatty acid metabolic process, endothelial cell differentiation, vascular endothelial growth factor receptor (VEGFR) signaling pathways are upregulated in endothelial cells (EC) (top) and downregulated pathways of activation of inflammation in the macrophages (MP) (bottom) in ApoE$^{-/-}$/Liver-DKO mice relative to ApoE$^{-/-}$ controls. F: Circular cnetplot representing downregulated pathways and corresponding genes in macrophages (MP). G: Circular cnetplot illustrating significantly upregulated pathways and corresponding genes in endothelial cells (EC). H: Violin plots showing diminished expression of inflammation genes, such as CD68, Vcam1, Icam1, and downregulated expression of FB markers, such as Col1a1, and elevated expression of VS markers, such as Acta2 and Tagln. Statistical analysis (A, B, C, H) in ApoE$^{-/-}$ and ApoE$^{-/-}$/Liver-DKO comparison is conducted by the Student's t-test.

Figure 2

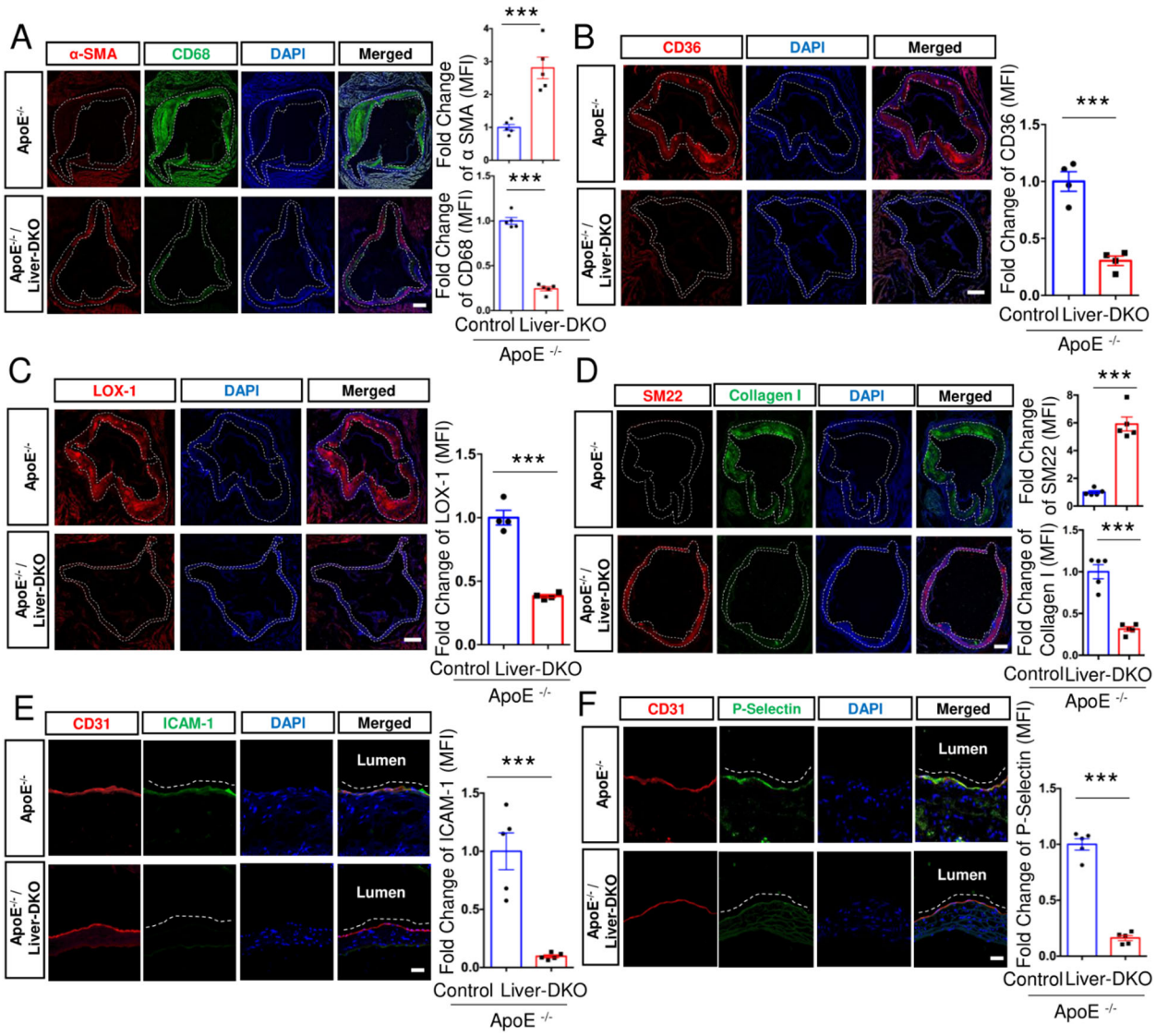
A
α-SMA
CD68
DAPI
Merged
ApoE-/-
ApoE-/- / Liver-DKO
Fold Change of α SMA (MFI)
Fold Change of CD68 (MFI)
***
Control
Liver-DKO
ApoE -/-
B
CD36
DAPI
Merged
Fold Change of CD36 (MFI)
C
LOX-1
Fold Change of LOX-1 (MFI)
D
SM22
Collagen I
Fold Change of SM22 (MFI)
Fold Change of Collagen I (MFI)
E
CD31
ICAM-1
Lumen
Fold Change of ICAM-1 (MFI)
F
P-Selectin
Fold Change of P-Selectin (MFI)

Figure 2: Liver-deficiency of epsins increases smooth muscle contractility, and inhibits inflammatory macrophage accumulation and endothelial cell activation in atherosclerotic plaques of ApoE$^{-/-}$ mice. A: Immunofluorescence (IF) staining of vascular smooth muscle cell marker α-SMA and macrophage marker CD68 in the aortas of ApoE$^{-/-}$ and ApoE$^{-/-}$/Liver-DKO mice (left). The fold change of mean fluorescence intensity (MFI) for α-SMA and CD68 proteins were quantified (right) (n=5, ***p<0.001). Scale bar, 200 μm. Elevated expression of α-SMA protein and diminished expression of CD68 protein in the aortas in ApoE$^{-/-}$/Liver-DKO. B-C: IF staining of scavenger receptors, such as CD36 (B) and LOX-1 (C), in the aortas of ApoE$^{-/-}$ and ApoE$^{-/-}$/Liver-DKO mice (left). The fold changes of CD36 (MFI) (B) and LOX-1 (MFI) (C) were quantified (right) (n=4, ***p<0.001). Scale bar, 200 μm. Diminished expression of CD36 and LOX-1 proteins in the aortas in ApoE$^{-/-}$/Liver-DKO. D: IF staining of vascular smooth muscle cell marker SM22 and collagen marker Collagen I in the aortas of ApoE$^{-/-}$ and ApoE$^{-/-}$/Liver-DKO mice (left). The fold changes of SM22 (MFI) and Collagen I (MFI) were quantified (right) (n=5, ***p<0.001). Scale bar, 200 μm. Elevated expression of SM22 protein and diminished expression of Collagen I protein in the aortas in ApoE$^{-/-}$/Liver-DKO. E-F: IF staining of endothelial cell marker CD31 and endothelial cell adhesion molecules, such as ICAM-1 (E) (left) and P-Selectin (F) (left), in the aortas between ApoE$^{-/-}$ and ApoE$^{-/-}$/Liver-DKO mice. The fold changes of ICAM-1 (MFI) (E) and P-Selectin (MFI) (F) were quantified (right) (n=5, ***p<0.001). Scale bar, 20 μm. Diminished expression of ICAM-1 and P-Selectin proteins in the aortas in ApoE$^{-/-}$/Liver-DKO. All statistical analysis (A-F) in ApoE$^{-/-}$ and ApoE$^{-/-}$/Liver-DKO comparison is conducted by the Student's t-test.

Figure.3

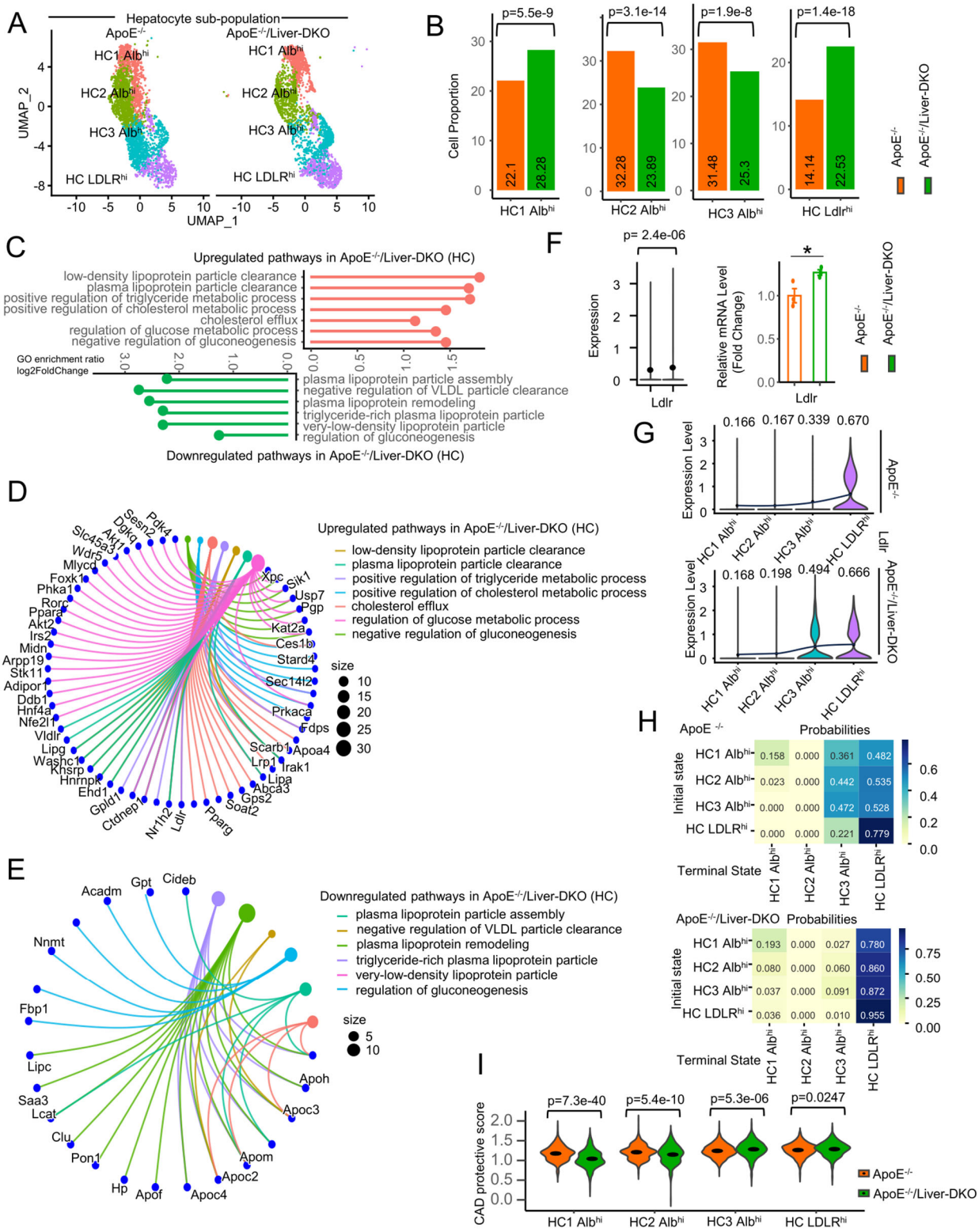
A
Hepatocyte sub-population
ApoE-/-
ApoE-/-/Liver-DKO
HC1 Alb^hi
HC2 Alb^hi
HC3 Alb^hi
HC LDLR^hi
UMAP_2
UMAP_1
B
p=5.5e-9
p=3.1e-14
p=1.9e-8
p=1.4e-18
Cell Proportion
22.1
28.28
32.28
23.89
31.48
25.3
14.14
22.53
HC1 Alb^hi
HC2 Alb^hi
HC3 Alb^hi
HC Ldlr^hi
ApoE-/-
ApoE-/-/Liver-DKO
C
Upregulated pathways in ApoE-/-/Liver-DKO (HC)
low-density lipoprotein particle clearance
plasma lipoprotein particle clearance
positive regulation of triglyceride metabolic process
positive regulation of cholesterol metabolic process
cholesterol efflux
regulation of glucose metabolic process
negative regulation of gluconeogenesis
GO enrichment ratio
log2FoldChange
plasma lipoprotein particle assembly
negative regulation of VLDL particle clearance
plasma lipoprotein remodeling
triglyceride-rich plasma lipoprotein particle
very-low-density lipoprotein particle
regulation of gluconeogenesis
Downregulated pathways in ApoE-/-/Liver-DKO (HC)
F
p= 2.4e-06
Expression
Ldlr
Relative mRNA Level (Fold Change)
*
ApoE-/-
ApoE-/-/Liver-DKO
D
Upregulated pathways in ApoE-/-/Liver-DKO (HC)
low-density lipoprotein particle clearance
plasma lipoprotein particle clearance
positive regulation of triglyceride metabolic process
positive regulation of cholesterol metabolic process
cholesterol efflux
regulation of glucose metabolic process
negative regulation of gluconeogenesis
size
10
15
20
25
30
Pdk4
Seesn2
Dgkq
Akt1
Slc45a3
Wdr5
Mlycd
Foxk1
Phka1
Rorc
Ppara
Akt2
Irs2
Midn
Arpp19
Stk11
Adipor1
Ddb1
Hnf4a
Nfe2l1
Vldlr
Lipg
Washc1
Khsrp
Hnrnpk
Ehd1
Gpld1
Ctdnep1
Nr1h2
Ldlr
Pparg
Soat2
Gps2
Abca3
Lipa
Irak1
Lrp1
Apoa4
Scarb1
Fdps
Prkaca
Sec14l2
Stard4
Ces1b
Kat2a
Pgp
Usp7
Sik1
Xpc
G
Expression Level
0.166
0.167
0.339
0.670
0.168
0.198
0.494
0.666
HC1 Alb^hi
HC2 Alb^hi
HC3 Alb^hi
HC LDLR^hi
Ldlr
ApoE-/-
ApoE-/-/Liver-DKO
H
ApoE -/-
Probabilities
Initial state
Terminal State
HC1 Alb^hi 0.158 0.000 0.361 0.482
HC2 Alb^hi 0.023 0.000 0.442 0.535
HC3 Alb^hi 0.000 0.000 0.472 0.528
HC LDLR^hi 0.000 0.000 0.221 0.779
ApoE-/-/Liver-DKO Probabilities
HC1 Alb^hi 0.193 0.000 0.027 0.780
HC2 Alb^hi 0.080 0.000 0.060 0.860
HC3 Alb^hi 0.037 0.000 0.091 0.872
HC LDLR^hi 0.036 0.000 0.010 0.955
E
Downregulated pathways in ApoE-/-/Liver-DKO (HC)
plasma lipoprotein particle assembly
negative regulation of VLDL particle clearance
plasma lipoprotein remodeling
triglyceride-rich plasma lipoprotein particle
very-low-density lipoprotein particle
regulation of gluconeogenesis
size
5
10
Acadm
Gpt
Cideb
Nnmt
Fbp1
Lipc
Saa3
Lcat
Clu
Pon1
Hp
Apof
Apoc4
Apoc2
Apom
Apoc3
Apoh
I
p=7.3e-40
p=5.4e-10
p=5.3e-06
p=0.0247
CAD protective score
HC1 Alb^hi
HC2 Alb^hi
HC3 Alb^hi
HC LDLR^hi
ApoE-/-
ApoE-/-/Liver-DKO

Figure 3: Single-cell RNA sequencing reveals increased Ldlr^{hi} hepatocytes proportion and elevated LDLR expression in the livers in ApoE$^{-/-}$ /Liver-DKO mice compared to ApoE$^{-/-}$ controls. A: UMAP visualization illustrating the heterogeneity of hepatocyte cell populations, indicating distinct clustering patterns of hepatocytes in ApoE$^{-/-}$/Liver-DKO mice compared to ApoE$^{-/-}$ controls. B: Bar plots of cell proportion of hepatocyte subclusters. There was a relatively high proportion of HC Ldlr^{hi} hepatocytes in the livers of ApoE$^{-/-}$/Liver-DKO mice compared with ApoE$^{-/-}$ controls. C: Gene Ontology (GO) analysis showing significantly enriched pathways of regulation of low-density lipoprotein particle clearance signaling pathways are upregulated in hepatocytes (HC) (top) and downregulated pathways of lipoprotein assembly and lipogenesis in hepatocytes (HC) (bottom) in ApoE$^{-/-}$/Liver-DKO mice relative to ApoE$^{-/-}$ controls. D: Circular cnetplot illustrating significantly upregulated pathways and corresponding genes in hepatocytes (HC). E: Circular cnetplot representing downregulated pathways and corresponding genes in hepatocytes (HC). F: Elevated expression of Ldlr in ApoE$^{-/-}$/Liver-DKO mice compared with ApoE$^{-/-}$ controls, shown through single-cell analysis (left) and real-time quantitative PCR (qPCR) (right). G: Violin plots of Ldlr expression in different hepatocyte subtypes, showing its upregulated expression in hepatocytes in ApoE$^{-/-}$/Liver-DKO mice compared to ApoE$^{-/-}$ controls. The mean expression levels of Ldlr are highlighted in the violin plots ($p<0.05$). H: CellRank analysis illustrating an increased propensity of differentiation from HC Alb ^{hi} towards HC Ldlr ^{hi} in ApoE$^{-/-}$/Liver-DKO mice relative to ApoE$^{-/-}$ controls. I: Coronary artery disease (CAD) protective score comparing ApoE$^{-/-}$/Liver-DKO with ApoE$^{-/-}$, showing it positively correlated to the expression of Ldlr ($n=3$, $*p<0.05$). Statistical analysis (B, F, G, I) in ApoE$^{-/-}$ and ApoE$^{-/-}$/Liver-DKO comparison is conducted by the Student's t-test.

Figure.4

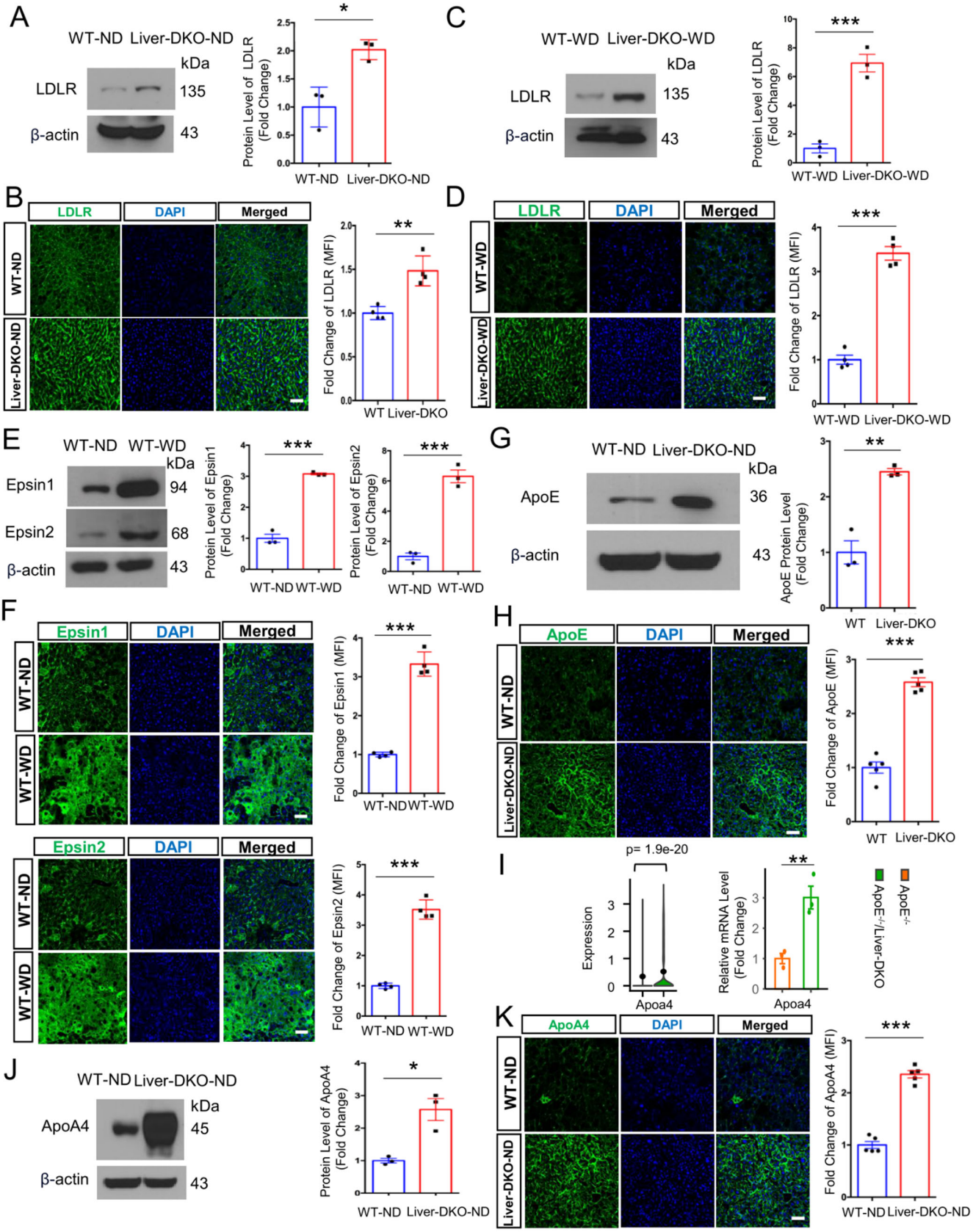
A
WT-ND Liver-DKO-ND
kDa
LDLR
135
β-actin
43
Protein Level of LDLR (Fold Change)
WT-ND Liver-DKO-ND
C
WT-WD Liver-DKO-WD
Protein Level of LDLR (Fold Change)
WT-WD Liver-DKO-WD
B
LDLR
DAPI
Merged
WT-ND
Liver-DKO-ND
Fold Change of LDLR (MFI)
WT Liver-DKO
D
WT-WD
Liver-DKO-WD
Fold Change of LDLR (MFI)
WT-WD Liver-DKO-WD
E
WT-ND WT-WD
Epsin1
94
Epsin2
68
Protein Level of Epsin1 (Fold Change)
Protein Level of Epsin2 (Fold Change)
G
WT-ND Liver-DKO-ND
ApoE
36
ApoE Protein Level (Fold Change)
WT Liver-DKO
F
Epsin1
Fold Change of Epsin1 (MFI)
Epsin2
Fold Change of Epsin2 (MFI)
H
ApoE
Fold Change of ApoE (MFI)
I
p= 1.9e-20
Expression
Apoa4
Relative mRNA Level (Fold Change)
ApoE-/-/Liver-DKO
ApoE-/-
J
ApoA4
45
Protein Level of ApoA4 (Fold Change)
K
ApoA4
Fold Change of ApoA4 (MFI)

Figure 4: Elevated LDLR, ApoE and ApoA4 expression in the liver of liver-specific epsins deficiency mice and elevated Epsin1 and Epsin2 in the liver of WD-fed mice. A: Western blot (WB) analysis of liver tissue harvested from WT and Liver-DKO mice (normal diet, ND) revealed elevated LDLR expression in Liver-DKO mice (left). Data quantification of LDLR expression (right) (n=3, ***p< 0.001). B: Immunofluorescence (IF) analysis of LDLR expression level in liver cryosections from ND-fed WT, Liver-DKO mice (left), demonstrating elevated LDLR protein level in the livers of Liver-DKO. Mean fluorescence intensity (MFI) quantification of LDLR under ND (right) (n=4, ***p<0.001). Scale bar, 50 µm. C: Western blot (WB) analysis of liver tissue harvested from WT and Liver-DKO (western diet, WD) mice showed elevated LDLR expression in WD-fed Liver-DKO mice (left). Data quantification of LDLR expression (right) (n=3, ***p<0.001). D: Immunofluorescence (IF) analysis of LDLR expression in liver cryosections from WD-fed WT and Liver-DKO mice (left), demonstrating that elevated LDLR protein level in WD-fed Liver-DKO mice. Mean fluorescence intensity (MFI) quantification of LDLR under WD (right) (n=4, ***p<0.001). Scale bar,50 µm. E: Western blot (WB) analysis of liver tissue harvested from WT (normal diet, ND) and WT (western diet, WD) mice showed elevated epsin1 and epsin2 expression in WD-fed WT mice (left). Data quantification of Epsin1 and Epsin2 expression (right) (n=3, ***p<0.001). F: Immunofluorescence (IF) analysis of Epsin1 and Epsin2 expression in liver cryosections from ND-fed WT and WD-fed WT mice (left), demonstrating that both Epsin1 and Epsin2 are significantly induced in WD-fed WT mice. Mean fluorescence intensity (MFI) quantification of Epsin1 and Epsin2 under WD (right) (n=4, ***p<0.001). Scale bar,50 µm. G: Western blot analysis for the evaluation of ApoE expression in the livers in both ND-fed WT and Liver-DKO mice (left). Data quantification of ApoE expression (right) (n=3, ** p < 0.01). H: Immunofluorescence (IF) analysis of ApoE expression in liver cryosections from both ND-fed WT and Liver-DKO mice (left). Mean fluorescence intensity (MFI) quantification of ApoE between WT and Liver-DKO mice (right) (n=5, *** p < 0.001). Scale bar, 50 µm. I: Violin plot of Apoa4 by single cell analysis (left) and RT-qPCR evaluation of Apoa4 mRNA expression between $ApoE^{-/-}$ controls and $ApoE^{-/-}$ /Liver-DKO mice (n=3, **p<0.01). J: Western blot of ApoA4 for the liver lysates from ND-fed WT and Liver-DKO, β-actin is used as an internal reference (left), quantification data of ApoA4 protein level (right) (n=3, *p<0.05). K: Immunofluorescence (IF) analysis of ApoA4 in the livers of both ND-fed WT and Liver-DKO mice (left). Quantification of mean fluorescence intensity (MFI) of ApoA4 protein level (right). Scale bar, 50 µm. All statistical analysis (A-K) in WT-ND and Liver-DKO-ND comparison or WT-WD and Liver-DKO-WD comparison or WT-ND and WT-WD comparison is conducted by the Student's t-test.

Figure.5

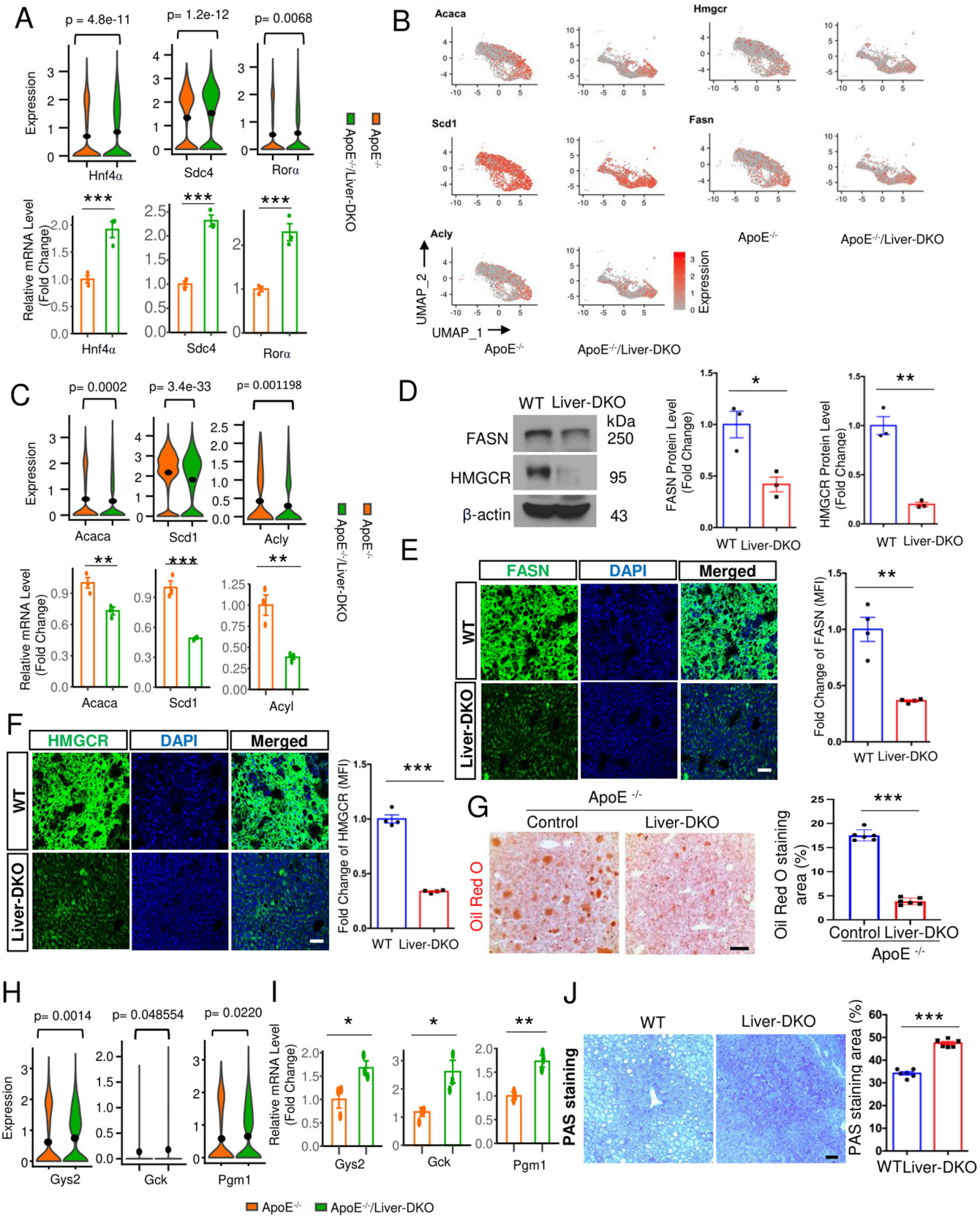
A
p = 4.8e-11
p= 1.2e-12
p= 0.0068
Expression
Hnf4α
Sdc4
Rorα
Relative mRNA Level (Fold Change)
***
ApoE-/-/Liver-DKO
ApoE-/-
B
Acaca
Hmgcr
Scd1
Fasn
Acly
UMAP_2
UMAP_1
Expression
ApoE-/-
ApoE-/-/Liver-DKO
C
p= 0.0002
p= 3.4e-33
p= 0.001198
Acaca
Scd1
Acly
Acyl
**
D
WT Liver-DKO
kDa
FASN
250
HMGCR
95
β-actin
43
FASN Protein Level (Fold Change)
HMGCR Protein Level (Fold Change)
*
E
FASN
DAPI
Merged
WT
Liver-DKO
Fold Change of FASN (MFI)
F
HMGCR
Fold Change of HMGCR (MFI)
G
ApoE -/-
Control
Liver-DKO
Oil Red O
Oil Red O staining area (%)
H
p= 0.0014
p= 0.048554
p= 0.0220
Gys2
Gck
Pgm1
I
Relative mRNA Level (Fold Change)
J
WT
Liver-DKO
PAS staining
PAS staining area (%)

Figure 5: Diminished lipogenic gene expression in the liver of liver-specific epsins deficiency mice resulted in lower hepatic lipid accumulation and elevated glycogenic gene expression in the liver of Liver-DKO mice that induced higher hepatic glycogen. A: Violin plots revealed elevated expression of genes that suppression of lipogenesis (Hnf4α, Sdc4, Rorα) in ApoE$^{-/-}$/Liver-DKO as compared to ApoE$^{-/-}$, shown through single-cell analysis (left). Validation of Hnf4α, Sdc4, Rorα gene expression involved in inhibition of lipogenesis by real-time quantitative PCR (qPCR) in the livers from both ApoE$^{-/-}$ and ApoE$^{-/-}$/Liver-DKO mice (right) (n=3, *** p<0.001). B: Feature plots show diminished expression of lipogenic genes in ApoE$^{-/-}$/Liver-DKO mice compared with ApoE$^{-/-}$ mice, such as *Acaca*, *Scd1*, *Acly*, *Hmgcr*, *Fasn*. C: Violin plots of gene expression related to lipogenesis (*Acaca*, *Scd1*, *Acly*) in ApoE$^{-/-}$/Liver-DKO as compared to ApoE$^{-/-}$, shown through single-cell analysis (left). Validation of *Acaca*, *Scd1* and *Acly* gene expression involved in lipogenesis by real-time quantitative PCR (qPCR) in the livers from both ApoE$^{-/-}$ and ApoE$^{-/-}$/Liver-DKO mice (right) (n=3, **p<0.01, *** p<0.001). D: Western blotting analysis of FASN and HMGCR proteins in the liver lysates from WT and Liver-DKO mice (left), and the relative expression of FASN and HMGCR proteins in the liver of WT and Liver-DKO mice are quantified (right) (n=3, * p<0.05, **p<0.01). Diminished FASN and HMGCR protein levels in the liver lysates in Liver-DKO mice. E-F: Immunofluorescence analysis of FASN (E) and HMGCR (F) expression in the livers of both WT and Liver-DKO mice (left). MFIs of FASN and HMGCR are quantified (right) (n=4, **p<0.01, *** p<0.001). Diminished expression of FASN and HMGCR in the liver cryosections in Liver-DKO mice. Scale bar, 50 μm. G: ORO staining of the livers (left) from ApoE$^{-/-}$ or ApoE$^{-/-}$ / Liver-DKO mice fed a WD, and unpaired t-test (right) for lipid-stained areas (n=5, ***p< 0.001). Scale bar, 500 μm. H: Violin plots of gene expression related to glycogenesis (*Gys2*, *Gck*, *Pgm1*) in ApoE$^{-/-}$/Liver-DKO as compared to ApoE$^{-/-}$, shown through single-cell analysis. I: Validation of *Gys2*, *Gck* and *Pgm1*gene expression involved in glycogenesis by real-time quantitative PCR (qPCR) in the liver from both ApoE$^{-/-}$ and ApoE$^{-/-}$/Liver-DKO mice (n=3, * p <0.05, ** p<0.01). J: Periodic acid-Schiff's (PAS) staining of the livers (left) from WT and Liver-DKO mice, and unpaired t-test (right) for glycogen-stained areas (n=6, ***p<0.001). Scale bar, 200 μm. Statistical analysis (A and C-J) in WT and Liver-DKO comparison or ApoE$^{-/-}$ controls and ApoE$^{-/-}$/Liver-DKO mice comparison is conducted by the Student's t-test.

Figure.6

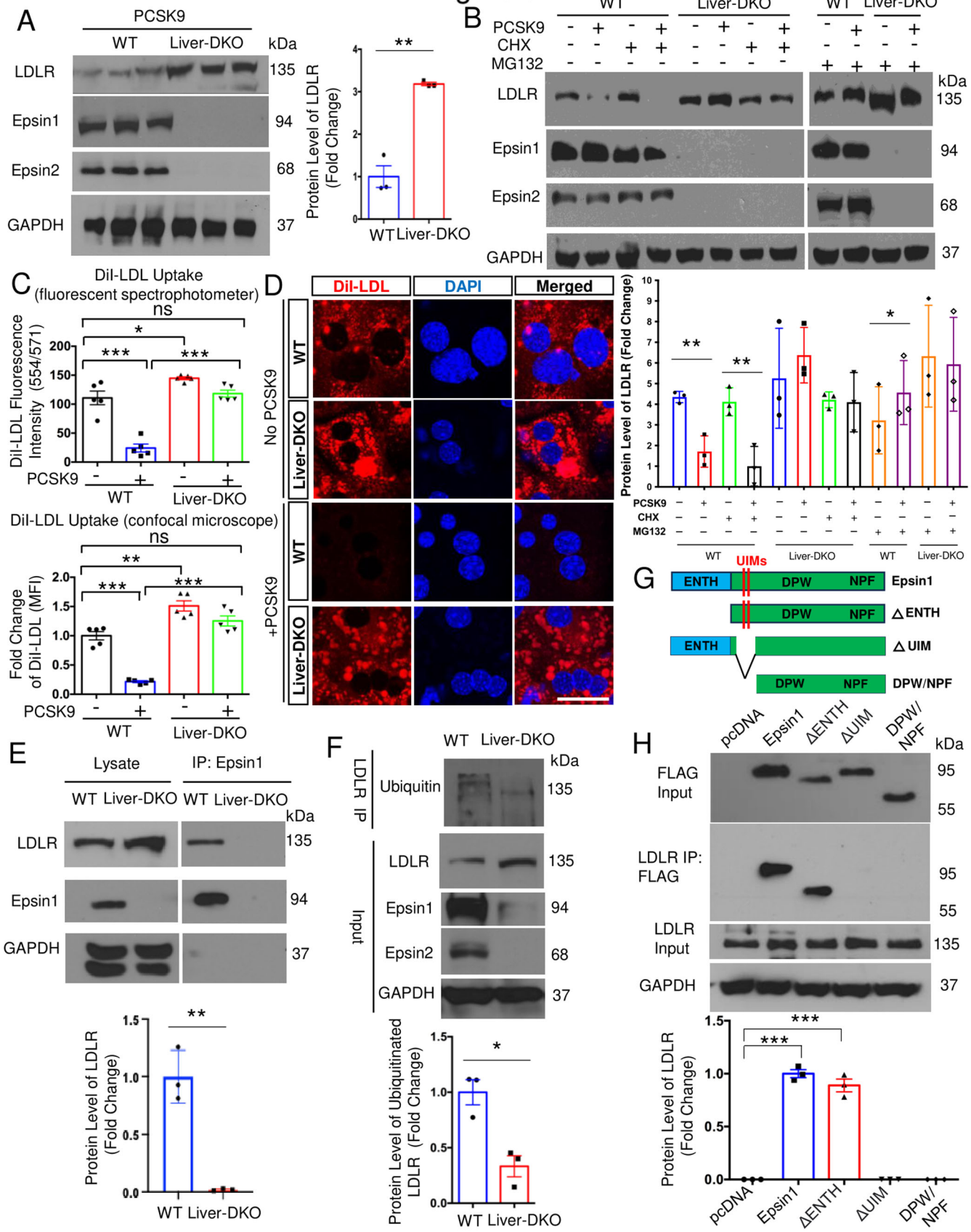
A
PCSK9
WT
Liver-DKO
kDa
LDLR
Epsin1
Epsin2
GAPDH
135
94
68
37
Protein Level of LDLR (Fold Change)
WT Liver-DKO
B
PCSK9
CHX
MG132
C
DiI-LDL Uptake (fluorescent spectrophotometer)
DiI-LDL Fluorescence Intensity (554/571)
ns
DiI-LDL Uptake (confocal microscope)
Fold Change of DiI-LDL (MFI)
D
DiI-LDL
DAPI
Merged
No PCSK9
+PCSK9
Protein Level of LDLR (Fold Change)
UIMs
G
ENTH
DPW
NPF
Epsin1
ΔENTH
ΔUIM
DPW/NPF
E
Lysate
IP: Epsin1
F
LDLR IP
Ubiquitin
Input
Protein Level of Ubiquitinated LDLR (Fold Change)
H
pcDNA
Epsin1
ΔENTH
ΔUIM
DPW/NPF
FLAG Input
LDLR IP: FLAG
LDLR Input

Figure 6: LDLR is Resistant to PCSK9-induced Proteasomal Degradation Results in Elevated LDL Uptake in Liver-DKO mice and LDLR Directly Binds to Epsin1 UIM Domain.

A: Western blot (WB) analysis of liver tissue harvested from WT and Liver-DKO mice injected with PCSK9-AAV8 virus revealed PCSK9-triggered LDLR degradation is inhibited in Liver-DKO mice (left). Data quantification (right) (n=3, **p<0.01). B: WB analysis of lysates from primary hepatocytes isolated from WT and Liver-DKO mice, treated with PCSK9, cycloheximide (CHX) and MG132 showed PCSK9-induced LDLR degradation occurred independent of new protein synthesis (in the presence of CHX) but was blocked by either loss of epsins or proteasomal inhibitor MG132 (top). Data quantification (bottom) (n=3, **p<0.01 vs lane 1, *p<0.05 vs lane 2). C: DiI-LDL uptake assay for the hepatocytes isolated from WT and Liver-DKO mice with or without PCSK9 treatment by measuring the DiI-LDL fluorescence intensity using a fluorescent spectrophotometer (ex 554/ em 571). Diminished mean DiI-LDL fluorescence intensity is detected in WT hepatocytes under PCSK9 treatment, while PCSK9-induced hepatocytes from Liver-DKO mice maintain high levels of mean DiI-LDL fluorescence intensity (n=5, * p < 0.05, *** p < 0.001). D: DiI-LDL uptake assay for the hepatocytes isolated from WT and Liver-DKO mice with or without PCSK9 treatment by taking DiI-LDL fluorescence images using confocal microscope. The mean fluorescence intensity (MFI) of different groups was quantified (lower-left corner). PCSK9-treated WT hepatocytes exhibited significantly diminished MFI of DiI-LDL compared with WT hepatocyte controls, while PCSK9-treated Liver-DKO hepatocytes maintained high levels of MFI of DiI-LDL compared with WT hepatocyte controls (n=5, ** p < 0.01, *** p < 0.001). Scale bar, 50 μm. E: Epsin1 antibody immunoprecipitation with lysates from liver tissue in both WT and Liver-DKO mice, anti-LDLR antibody was used to detect the LDLR expression between WT and Liver-DKO mice after IP assay. Liver lysates from both WT and Liver-DKO mice were also used as input control for testing anti-LDLR, Epsin1, and GAPDH antibodies (top). Data quantification of IP assay (bottom) (n=3, **p<0.01). Anti-epsin1 co-IPs showed LDLR directly binds Epsin 1 in WT, but not in Liver-DKO mice. F: LDLR antibody immunoprecipitation with lysates from liver tissue in both WT and Liver-DKO mice, anti-Ubiquitin antibody was used to detect the ubiquitinated LDLR between WT and Liver-DKO mice. Liver lysates from both WT and Liver-DKO mice were also used as input control for testing anti-LDLR, Epsin1, Epsin2, and GAPDH antibodies (top). Data quantification of IP assay (bottom) (n=3, *p<0.05). G: Schematic of Epsin 1 deletion mutants and individual protein domains, including full-length epsin1, ΔENTH, ΔUIM, DPW/NPF plasmids. H: LDLR antibody immunoprecipitation with lysates from HepG2 cells that transfected with FLAG-fused plasmids mentioned above. An anti-FLAG antibody was used to detect FLAG expression. HepG2 cell lysates that transfected with different FLAG-fused plasmids were also used as input control for testing anti-FLAG, LDLR, and GAPDH antibodies (top). Data quantification of IP assay (bottom) (n=3, ***p<0.001). Statistical analysis (A, E, F, H) is conducted by the Student's t-test, and statistical analysis (B, C, D) is conducted by two-way ANOVA with post hoc test.

Figure.7

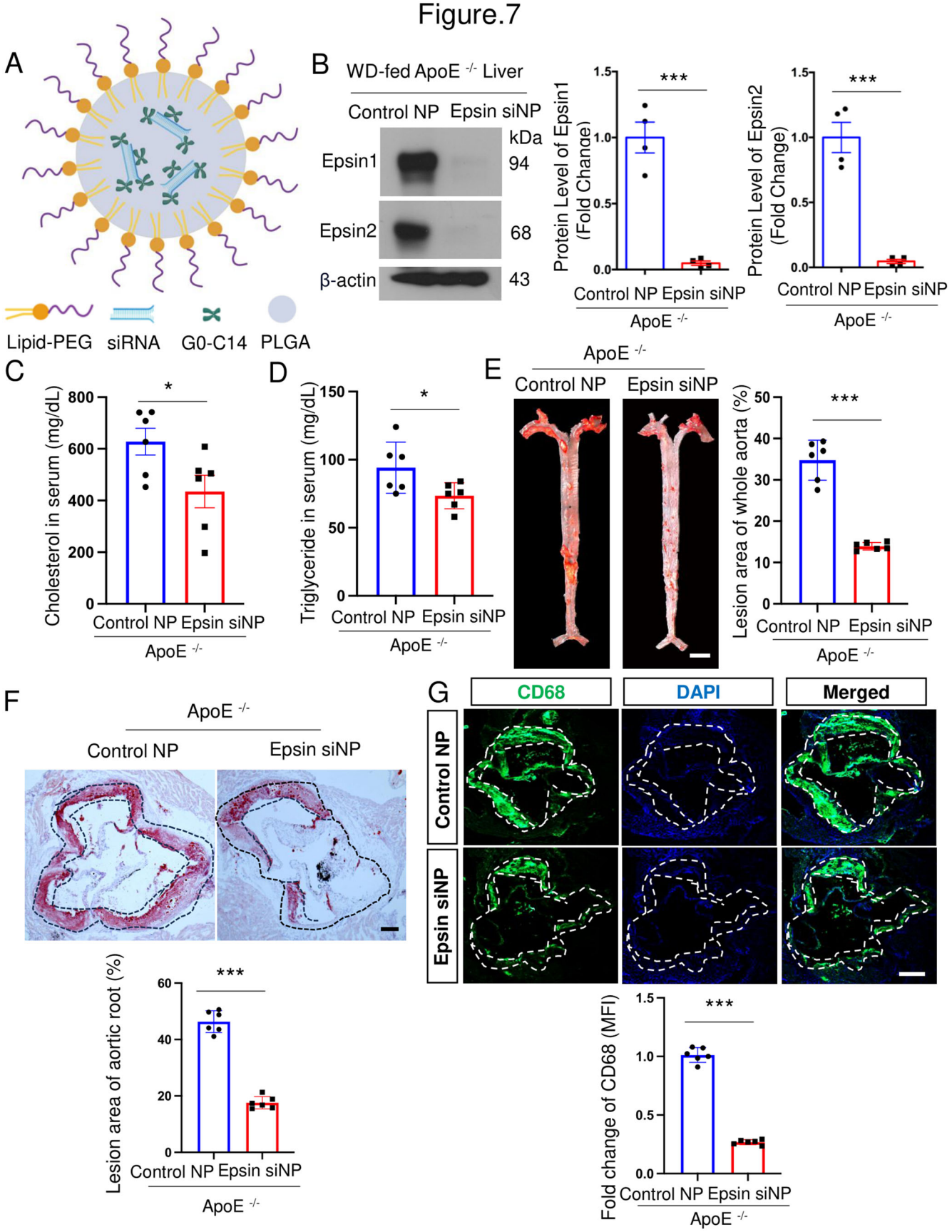
A
Lipid-PEG
siRNA
G0-C14
PLGA
B
WD-fed ApoE -/- Liver
Control NP
Epsin siNP
kDa
Epsin1
94
Epsin2
68
β-actin
43
Protein Level of Epsin1 (Fold Change)
Protein Level of Epsin2 (Fold Change)
***
Control NP Epsin siNP
ApoE -/-
C
Cholesterol in serum (mg/dL)
*
Control NP Epsin siNP
ApoE -/-
D
Triglyceride in serum (mg/dL)
*
Control NP Epsin siNP
ApoE -/-
E
ApoE -/-
Control NP
Epsin siNP
Lesion area of whole aorta (%)
***
Control NP Epsin siNP
ApoE -/-
F
ApoE -/-
Control NP
Epsin siNP
Lesion area of aortic root (%)
***
Control NP Epsin siNP
ApoE -/-
G
CD68
DAPI
Merged
Control NP
Epsin siNP
Fold change of CD68 (MFI)
***
Control NP Epsin siNP
ApoE -/-

Figure 7: Nanoparticles (NPs) with epsin1/2 siRNA inhibit lesion formation and macrophage accumulation. A: Schematic of the siRNA encapsulated lipid nanoparticles (LNP) platform composed of a lipid-PEG shell with a PLGA core containing G0-C14/siRNA complexes. B: Western blots of liver lysates were isolated from WD-fed ApoE$^{-/-}$ mice (8 weeks) and treated with control or epsin siRNA NPs (1 nmoles) for 3 weeks (2 doses/week) (left). The protein expression of Epsin1 and Epsin2 under control or epsin siRNA NPs treatment was quantified (right) (n=4, *** $p<0.001$). C-D: Plasma cholesterol (C) and triglyceride (TG) levels (D) in WD-fed ApoE$^{-/-}$ (WT) and epsin siRNA-nanoparticle (NP)-treated mice (n=6, *$p<0.05$). E: *En face* ORO staining of aortas (left) from control siRNA NP-treated ApoE$^{-/-}$ or epsin1/2 siRNA NP-treated ApoE$^{-/-}$ mice fed a WD, and unpaired t-test (right) for lesion areas (n=6, ***$p<0.001$). Scale bar, 5mm. F: Aortic roots from control siRNA NP-treated ApoE$^{-/-}$ or epsin1/2 siRNA NP-treated ApoE$^{-/-}$ mice were stained with ORO (top), and quantification of aortic root lesion areas (bottom) (n=6, ***$p<0.001$). Scale bar, 200 µm. G: Aortic roots from control siRNA NP-treated ApoE$^{-/-}$ or epsin1/2 siRNA NP-treated ApoE$^{-/-}$ mice were stained by macrophage marker, CD68 antibody (top), and the mean fluorescence intensity (MFI) of CD68 is quantified (bottom) (n=6, ***$p<0.001$). Scale bar, 300 µm. Statistical analysis (B-G) in Control NP and Epsin siNP comparison is conducted by the Student's t-test.

Figure.8

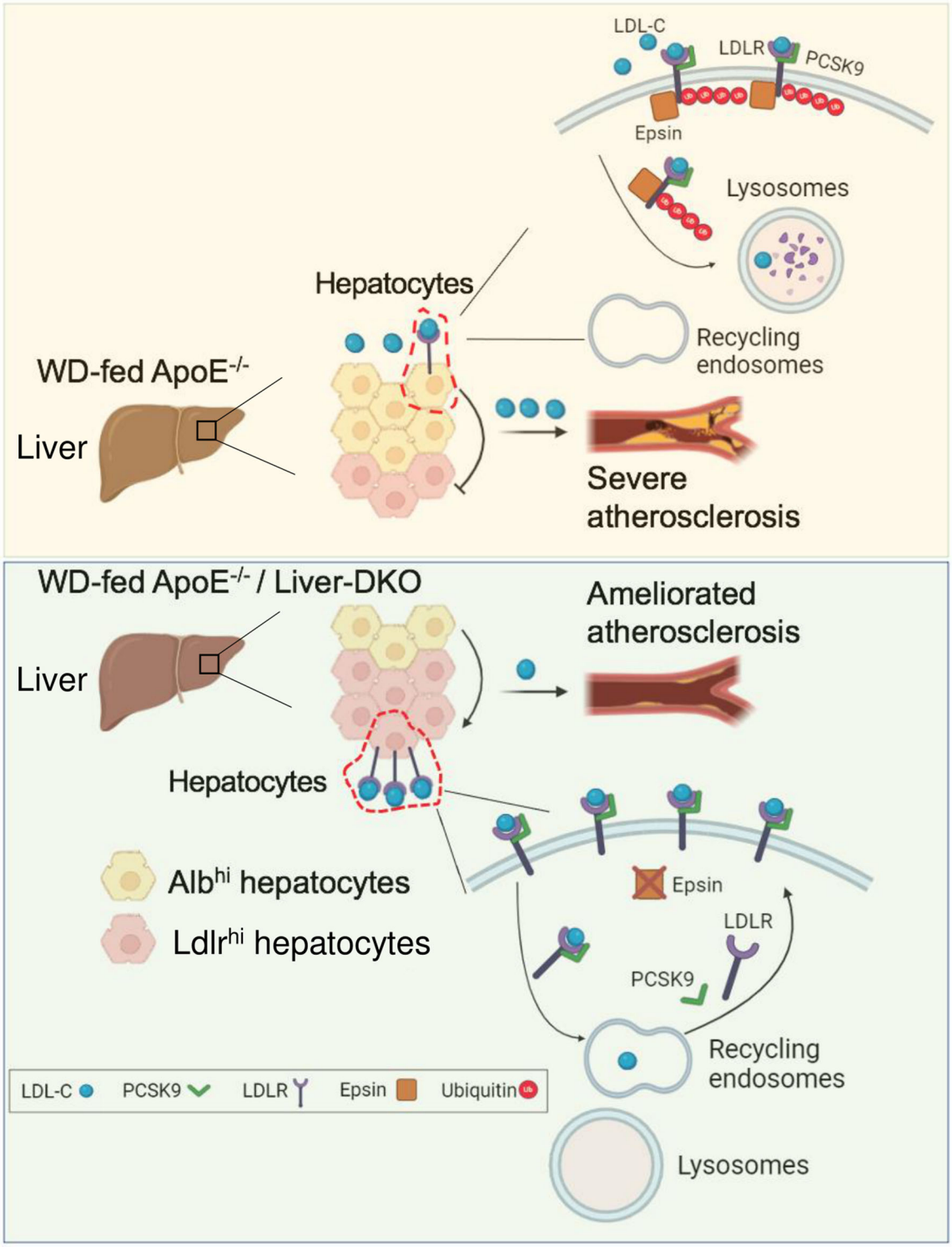
LDL-C
LDLR
PCSK9
Epsin
Lysosomes
Hepatocytes
Recycling endosomes
WD-fed ApoE-/-
Liver
Severe atherosclerosis
WD-fed ApoE-/- / Liver-DKO
Ameliorated atherosclerosis
Liver
Hepatocytes
Albhi hepatocytes
Ldlrhi hepatocytes
Epsin
LDLR
PCSK9
Recycling endosomes
Lysosomes
LDL-C
PCSK9
LDLR
Epsin
Ubiquitin

Figure 8: Western diet (WD)-fed ApoE$^{-/-}$/Liver-DKO mice have elevated low-density lipoprotein cholesterol (LDL-C) clearance compared with WD-fed ApoE$^{-/-}$ mice is attributable to their lower Alb^{hi} lipogenic hepatocytes and higher Ldlr ^{hi} glycogenic hepatocytes proportions. In the liver, glycogenesis inhibits lipogenesis. Consequently, the progression of atherosclerotic plaques is significantly ameliorated in WD-fed ApoE$^{-/-}$ /Liver-DKO mice. Mechanistically, loss of epsins protein in the liver prevents ubiquitination-driven LDLR degradation. The expressed LDLR in hepatocyte cell membrane uptakes LDL-C from the circulation. In the presence of epsins protein in the liver (top), in WT mice, PCSK9 binds to LDLR, epsins protein mediates LDLR ubiquitination, and the ubiquitinated LDLR is directed to lysosomes for protein degradation. Consequently, elevated circulating LDL-C due to PCSK9-mediated LDLR degradation. In the absence of epsins protein in the liver (bottom), in epsin1/2 Liver-DKO mice, PCSK9 binds to LDLR, but the LDLR ubiquitination is abolished thanks to the deficiency of epsins protein. The LDLR is directed to recycling endosomes, and LDLR protein can be recycled and back to the plasma membrane of the hepatocytes to bind more LDL in the circulation and lower blood LDL-C levels.

Supplemental Figures

Figure.S1

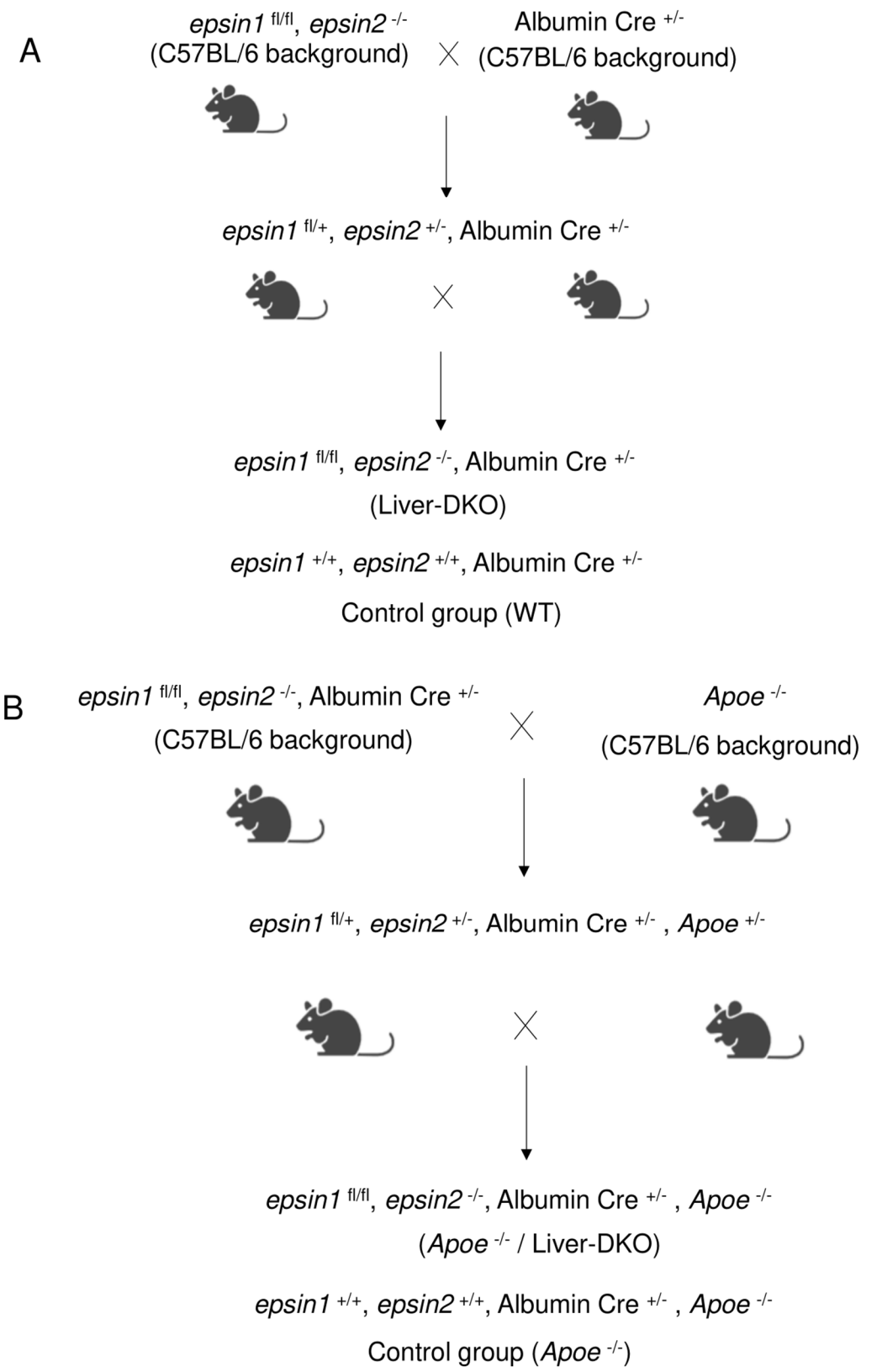

Figure S1: Overview of animal models. A: Workflow of generation of *epsin1* $^{fl/fl}$, *epsin2* $^{-/-}$, Albumin Cre $^{+/-}$ (Liver-DKO), *epsin1* $^{+/+}$, and *epsin2* $^{+/+}$, Albumin Cre $^{+/-}$ as control group (WT). B: Workflow of generation of *epsin1* $^{fl/fl}$, *epsin2* $^{-/-}$, Albumin Cre $^{+/-}$, *Apoe*$^{-/-}$ (*Apoe* $^{-/-}$ /Liver-DKO), and *epsin1* $^{+/+}$, *epsin2* $^{+/+}$, Albumin Cre $^{+/-}$, *Apoe*$^{-/-}$ as control group (*Apoe*$^{-/-}$).

Figure.S2

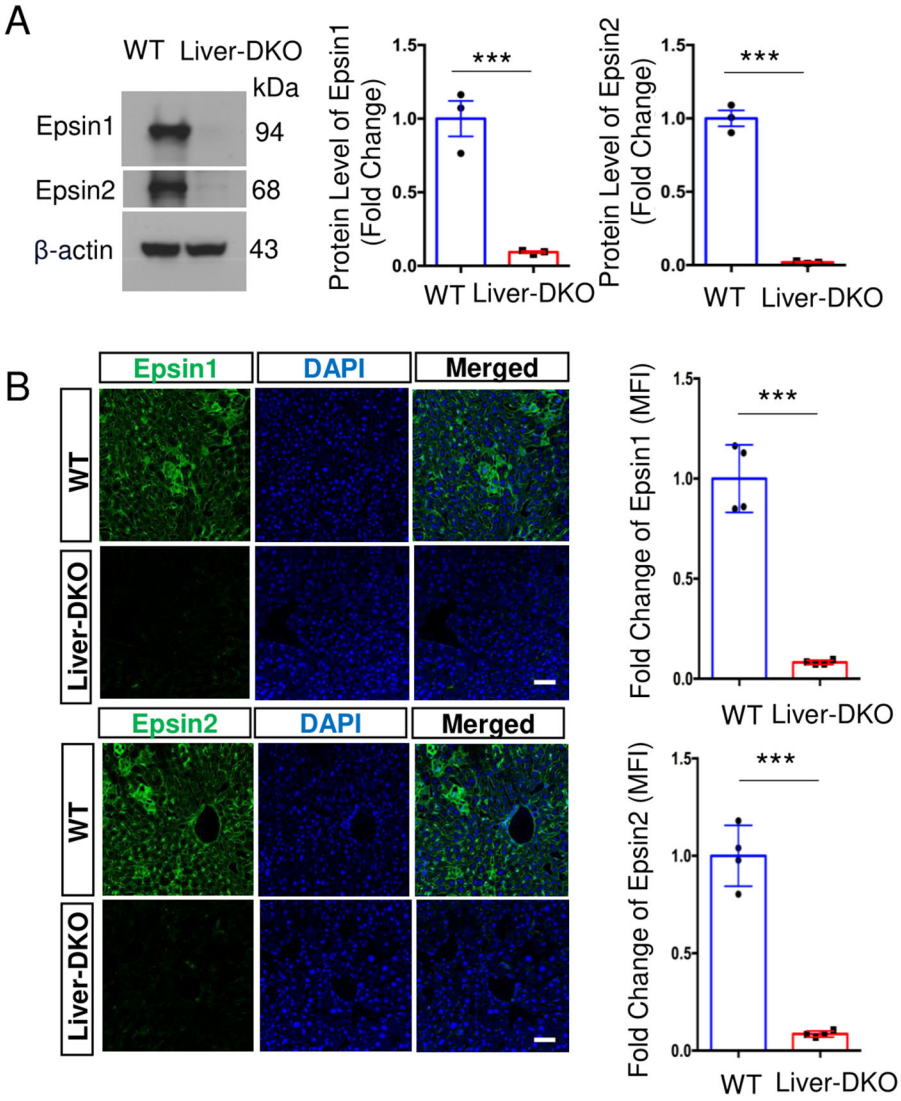
A
WT
Liver-DKO
kDa
Epsin1
94
Epsin2
68
β-actin
43
Protein Level of Epsin1 (Fold Change)
Protein Level of Epsin2 (Fold Change)
***
1.5
1.0
0.5
0.0
WT
Liver-DKO
B
Epsin1
DAPI
Merged
Epsin2
WT
Liver-DKO
Fold Change of Epsin1 (MFI)
Fold Change of Epsin2 (MFI)

Figure S2: Evidence of the deficiency of Epsin1 and Epsin2 in Liver-DKO mice. A:Western blot shows no protein expression of both Epsin1 and Epsin2 proteins in the liver lysates isolated from Liver-DKO mice (left). Quantification of Epsin1 and Epsin2 protein level (right) (n=3, *** $p<0.001$). B: Immunofluorescence analyses validate no Epsin1 and Epsin2 protein expression in the liver cryosection from Liver-DKO mice (left). Quantification of the MFI of Epsin1 and Epsin2 (right) (n=5, *** $p<0.001$). Statistical analysis (A and B) in WT and Liver-DKO mice comparison is conducted by the Student's t-test.

Figure.S3

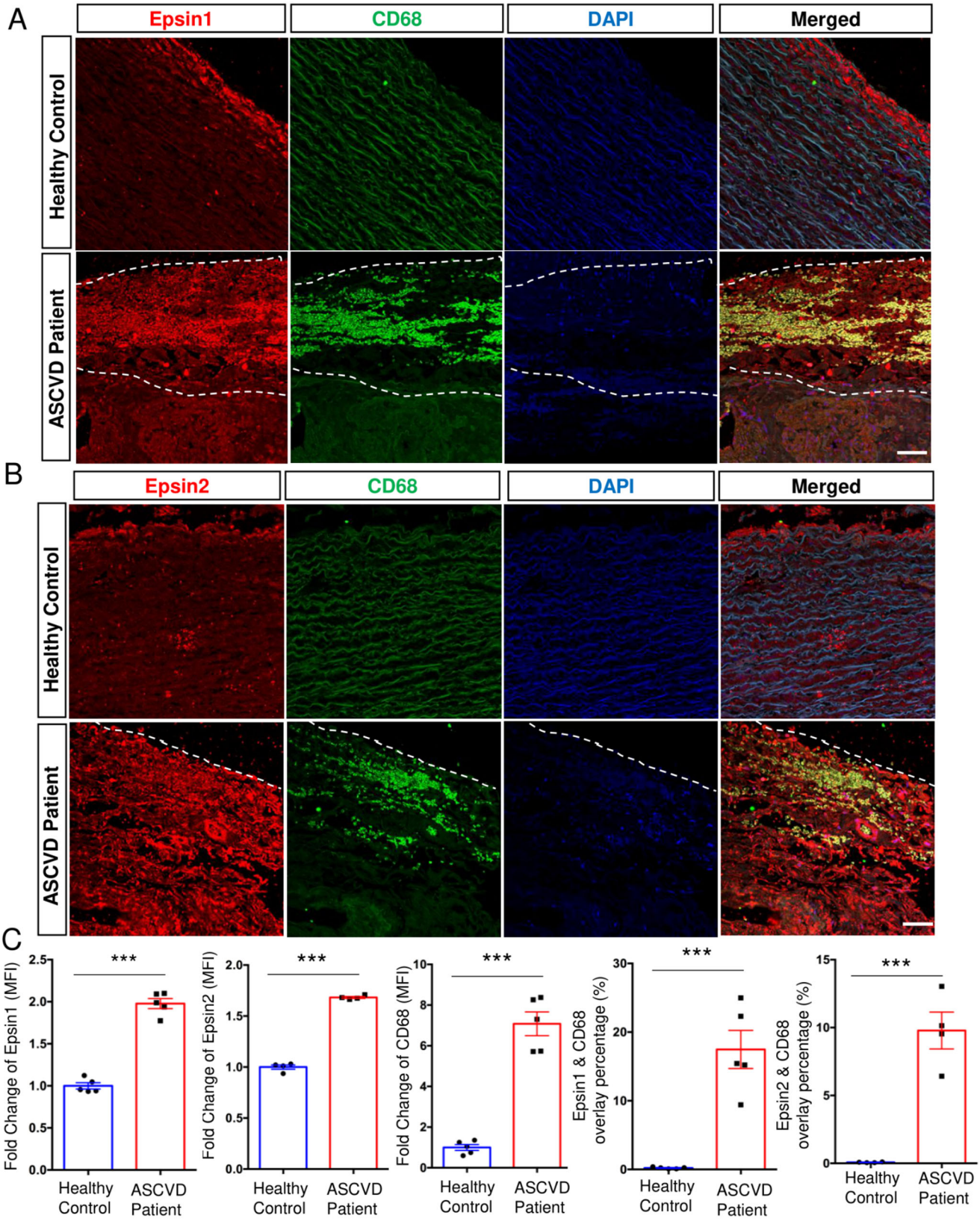
A
Epsin1
CD68
DAPI
Merged
Healthy Control
ASCVD Patient
B
Epsin2
CD68
DAPI
Merged
Healthy Control
ASCVD Patient
C
Fold Change of Epsin1 (MFI)
Fold Change of Epsin2 (MFI)
Fold Change of CD68 (MFI)
Epsin1 & CD68 overlay percentage (%)
Epsin2 & CD68 overlay percentage (%)
***
Healthy Control
ASCVD Patient

Figure S3: Elevated epsin1 and epsin2 expression in the aortic biopsies of ASCVD patients, and recruitment of CD68 positive macrophages in the aortas from ASCVD patients that colocalize with both epsin1 and epsin2. A: Immunofluorescence co-stain of Epsin1 and CD68 antibodies in the aortas of both healthy control and ASCVD patients. Epsin1 is red, CD68 is green, and DAPI is used for nuclear stains. The atherosclerotic lesion is encircled with a dashed line in ASCVD patients. Scale bar, 50 μm. B: Immunofluorescence co-stain of Epsin2 and CD68 antibodies in the aortas of both healthy control and ASCVD patients. Epsin2 is red, CD68 is green, and DAPI is used for nuclear stains. The atherosclerotic lesion is highlighted below the dashed line in ASCVD patients. Scale bar, 50 μm. C: Quantification of mean fluorescence intensity (MFI) of Epsin1, Epsin2 and CD68 proteins between healthy control and ASCVD patients. CD68 expression is highly colocalized with both Epsin1 and Epsin2 in ASCVD patients, and the overlay percentage between CD68 and Epsin1 or CD68 and Epsin2 are quantified (n=5, *** $p<0.001$). Statistical analysis (C) in healthy control and ASCVD patients' comparison is conducted by the Student's t-test.

Figure S4

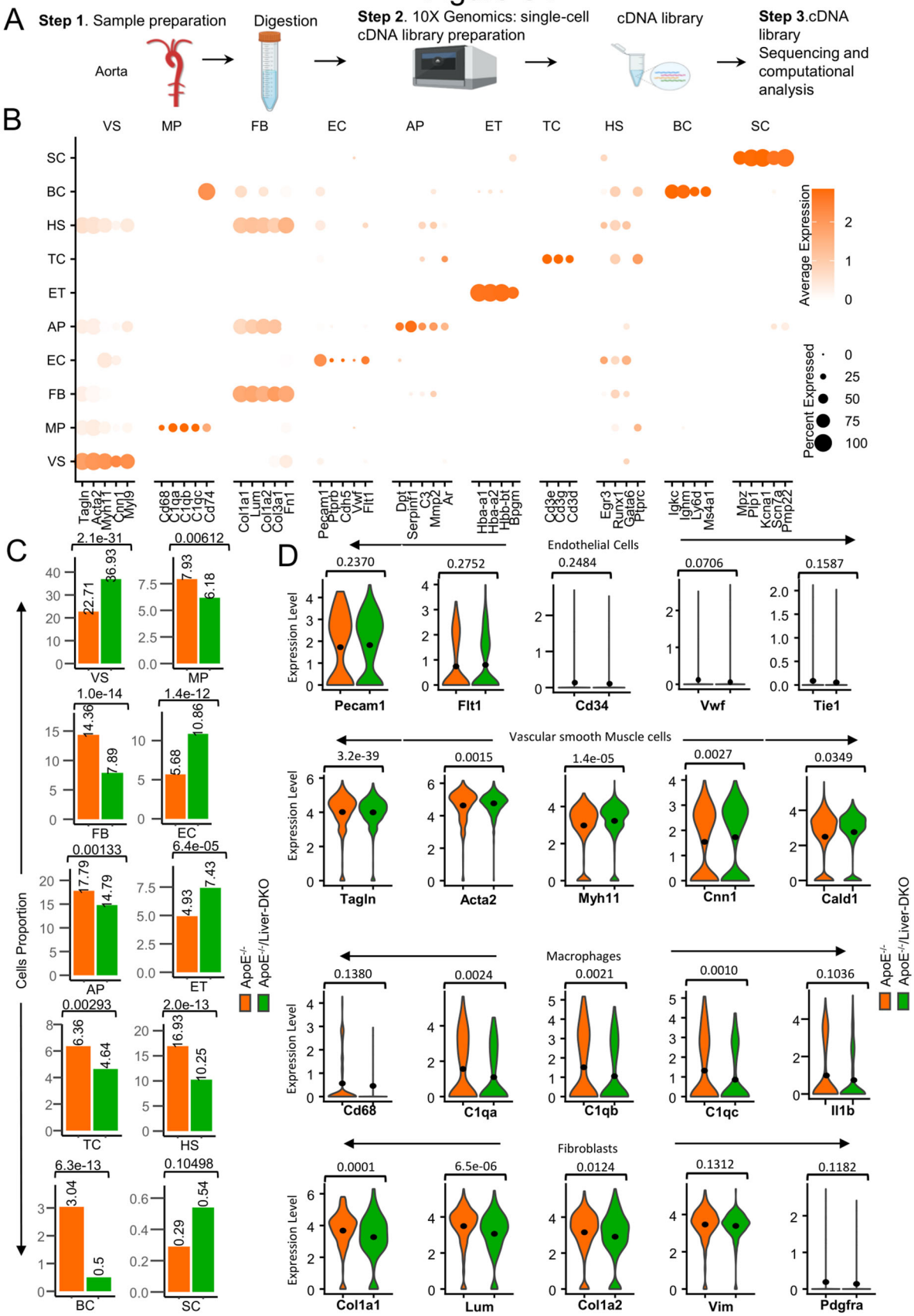
A
Step 1. Sample preparation
Aorta
Digestion
Step 2. 10X Genomics: single-cell cDNA library preparation
cDNA library
Step 3.cDNA library Sequencing and computational analysis
B
VS MP FB EC AP ET TC HS BC SC
Average Expression
Percent Expressed
Tagln Acta2 Myh11 Cnn1 Myl9 Cd68 C1qa C1qb C1qc Cd74 Col1a1 Lum Col1a2 Col3a1 Fn1 Pecam1 Ptprb Cdh5 Vwf Flt1 Dpt Serpinf1 C3 Mmp2 Ar Hba-a1 Hba-a2 Hbb-bt Bpgm Cd3e Cd3g Cd3d Egr3 Runx1 Gata6 Ptprc Igkc Ighm Ly6d Ms4a1 Mpz Plp1 Kcna1 Scn7a Pmp22
C
Cells Proportion
ApoE-/- ApoE-/-/Liver-DKO
D
Endothelial Cells
Vascular smooth Muscle cells
Macrophages
Fibroblasts
Expression Level
Pecam1 Flt1 Cd34 Vwf Tie1
Tagln Acta2 Myh11 Cnn1 Cald1
Cd68 C1qa C1qb C1qc Il1b
Col1a1 Lum Col1a2 Vim Pdgfra

Figure S4: Single-cell RNA-sequencing reveals different cell types in the aortas in both ApoE$^{-/-}$ controls and ApoE$^{-/-}$/Liver-DKO mice. A: Schematic representation of the single-cell RNA-sequencing (scRNA-seq) process performed on aortas from ApoE$^{-/-}$ and ApoE$^{-/-}$/Liver-DKO mice. B: Dot plot illustrates the percentage of cells expressing each gene marker corresponding to specific cell types in ApoE$^{-/-}$/Liver-DKO and ApoE$^{-/-}$ mice. The size of the dots represents the proportion of cells expressing the marker, while the color intensity indicates the expression level of the gene marker in each cell type. C: Bar plots showing the cell proportions of different sub-cell types in the aortas of ApoE$^{-/-}$ and ApoE$^{-/-}$ /Liver-DKO mice. A relatively higher proportion of VS, EC and a relatively lower proportion of MP, FB in the aortas of ApoE$^{-/-}$/Liver-DKO than ApoE$^{-/-}$ controls. D: Violin plots of markers of different cell types, including endothelial cells, vascular smooth muscle cells, macrophages, and fibroblasts. Endothelial cell markers: *Pecam1*, *Flt1*, *CD34*, *Vwf*, *Tei1*. Vascular smooth muscle cell makers: *Tagln*, *Acta2*, *Myh11*, *Cnn1*, and *Cald1*. Macrophage markers: *Cd68*, *C1qa*, *C1qb*, *C1qc*, *Il1b*. Fibroblast markers: *Col1a1*, *Lum*, *Col1a2*, *Vim*, *Pdgfra*. All p values of violin plots are labeled above. Statistical analysis (C, D) in ApoE$^{-/-}$ and ApoE$^{-/-}$/Liver-DKO comparison is conducted by the Student's t-test.

Figure S5

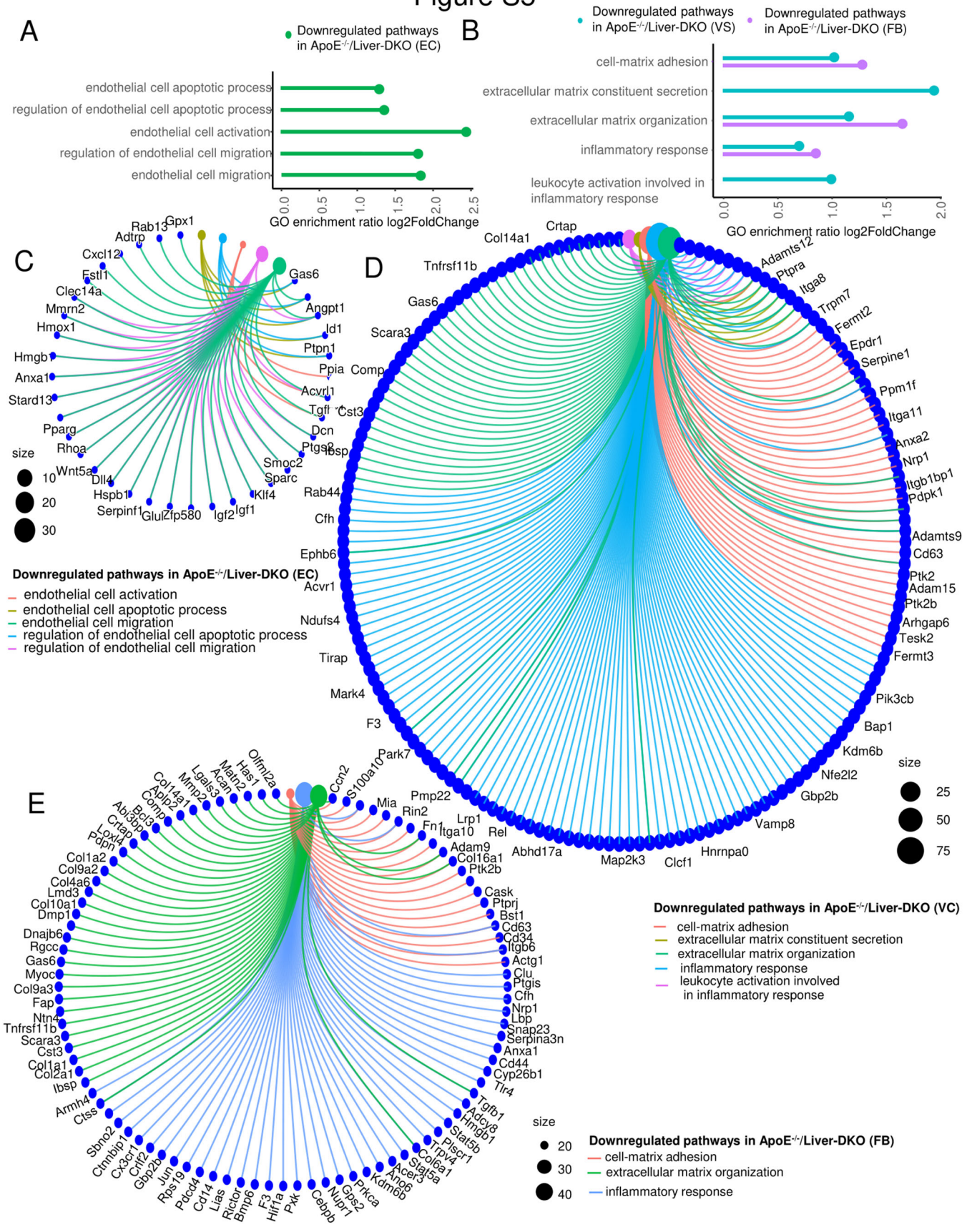
A
Downregulated pathways in ApoE-/-/Liver-DKO (EC)
endothelial cell apoptotic process
regulation of endothelial cell apoptotic process
endothelial cell activation
regulation of endothelial cell migration
endothelial cell migration
0.0
0.5
1.0
1.5
2.0
2.5
GO enrichment ratio log2FoldChange
B
Downregulated pathways in ApoE-/-/Liver-DKO (VS)
Downregulated pathways in ApoE-/-/Liver-DKO (FB)
cell-matrix adhesion
extracellular matrix constituent secretion
extracellular matrix organization
inflammatory response
leukocyte activation involved in inflammatory response
0.0
0.5
1.0
1.5
2.0
GO enrichment ratio log2FoldChange
C
size
10
20
30
Downregulated pathways in ApoE-/-/Liver-DKO (EC)
endothelial cell activation
endothelial cell apoptotic process
endothelial cell migration
regulation of endothelial cell apoptotic process
regulation of endothelial cell migration
D
size
25
50
75
Downregulated pathways in ApoE-/-/Liver-DKO (VC)
cell-matrix adhesion
extracellular matrix constituent secretion
extracellular matrix organization
inflammatory response
leukocyte activation involved in inflammatory response
E
size
20
30
40
Downregulated pathways in ApoE-/-/Liver-DKO (FB)
cell-matrix adhesion
extracellular matrix organization
inflammatory response

Figure S5: Single-cell RNA sequencing reveals upregulated or downregulated pathways in different cell types in the aortas in both ApoE$^{-/-}$ controls and ApoE$^{-/-}$/Liver-DKO mice. A-B: Gene Ontology (GO) analysis showing downregulated enriched pathways of regulation of endothelial cell apoptosis, endothelial cell activation, and endothelial cell migration in endothelial cells (A) and downregulated enriched pathways of regulation of cell-matrix adhesion, inflammatory response in both vascular smooth muscle cells and fibroblasts (B) in ApoE$^{-/-}$/Liver-DKO mice relative to ApoE$^{-/-}$ controls. C: Circular cnetplot illustrating significantly downregulated pathways and corresponding genes in endothelial cells (EC), such as endothelial cell activation, migration, and apoptotic process. D: Circular cnetplot representing downregulated pathways and corresponding genes in vascular smooth muscle cells (VS), including cell-matrix adhesion, extracellular matrix organization, and inflammatory response. E: Circular cnetplot representing downregulated pathways and corresponding genes in fibroblasts (FB), such as cell-matrix adhesion, extracellular matrix organization, and inflammatory response.

Figure S6

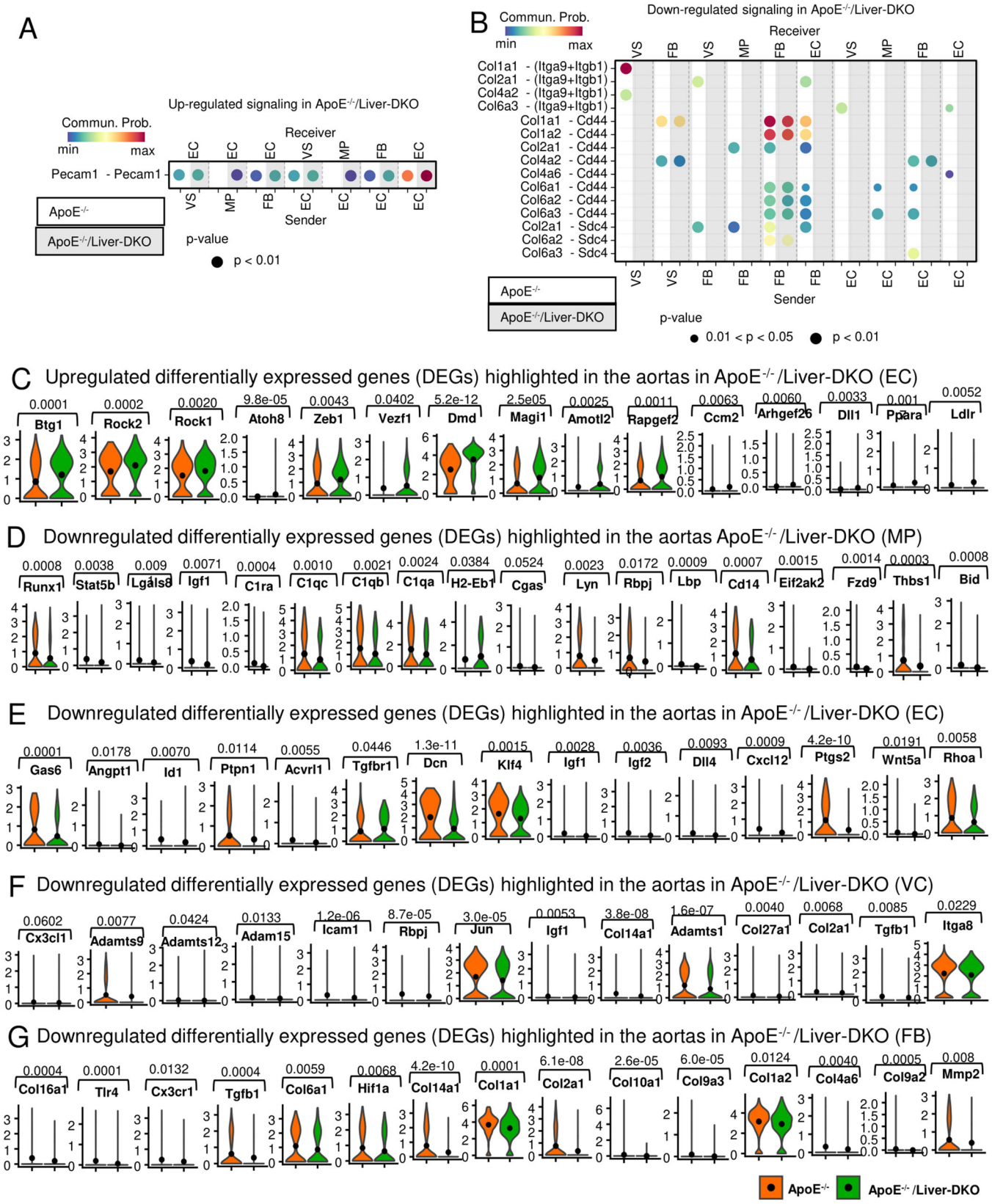
A
Up-regulated signaling in ApoE-/-/Liver-DKO
Commun. Prob.
min
max
Receiver
Pecam1 - Pecam1
Sender
ApoE-/-
ApoE-/-/Liver-DKO
p-value
p < 0.01
B
Down-regulated signaling in ApoE-/-/Liver-DKO
Col1a1 - (Itga9+Itgb1)
Col2a1 - (Itga9+Itgb1)
Col4a2 - (Itga9+Itgb1)
Col6a3 - (Itga9+Itgb1)
Col1a1 - Cd44
Col1a2 - Cd44
Col2a1 - Cd44
Col4a2 - Cd44
Col4a6 - Cd44
Col6a1 - Cd44
Col6a2 - Cd44
Col6a3 - Cd44
Col2a1 - Sdc4
Col6a2 - Sdc4
Col6a3 - Sdc4
0.01 < p < 0.05
p < 0.01
C Upregulated differentially expressed genes (DEGs) highlighted in the aortas in ApoE-/-/Liver-DKO (EC)
Btg1 Rock2 Rock1 Atoh8 Zeb1 Vezf1 Dmd Magi1 Amotl2 Rapgef2 Ccm2 Arhgef26 Dll1 Ppara Ldlr
D Downregulated differentially expressed genes (DEGs) highlighted in the aortas ApoE-/-/Liver-DKO (MP)
Runx1 Stat5b Lgals8 Igf1 C1ra C1qc C1qb C1qa H2-Eb1 Cgas Lyn Rbpj Lbp Cd14 Eif2ak2 Fzd9 Thbs1 Bid
E Downregulated differentially expressed genes (DEGs) highlighted in the aortas in ApoE-/-/Liver-DKO (EC)
Gas6 Angpt1 Id1 Ptpn1 Acvrl1 Tgfbr1 Dcn Klf4 Igf1 Igf2 Dll4 Cxcl12 Ptgs2 Wnt5a Rhoa
F Downregulated differentially expressed genes (DEGs) highlighted in the aortas in ApoE-/-/Liver-DKO (VC)
Cx3cl1 Adamts9 Adamts12 Adam15 Icam1 Rbpj Jun Igf1 Col14a1 Adamts1 Col27a1 Col2a1 Tgfb1 Itga8
G Downregulated differentially expressed genes (DEGs) highlighted in the aortas in ApoE-/-/Liver-DKO (FB)
Col16a1 Tlr4 Cx3cr1 Tgfb1 Col6a1 Hif1a Col14a1 Col1a1 Col2a1 Col10a1 Col9a3 Col1a2 Col4a6 Col9a2 Mmp2
ApoE-/-
ApoE-/-/Liver-DKO

Figure S6: Single-cell RNA-sequencing upregulated and downregulated pathways in ApoE$^{-/-}$/Liver-DKO, and violin plots highlighted the differentially expressed genes presented in cnet plots. A-B: Illustration of enhanced Pecam1-associated communication pathway (A) and inhibited Collagen-associated communication pathways (B) in ApoE$^{-/-}$/Liver-DKO relative to ApoE$^{-/-}$ controls, indicating diminished collagen synthesis in the aortas in ApoE$^{-/-}$/Liver-DKO mice. C-G:
Violin plots of differentially expressed genes (DEGs) that are highlighted in cnet plots of upregulated pathways in endothelial cells (EC) (C), downregulated pathways in macrophages (MP) (D), downregulated pathways in endothelial cells (EC) (E), downregulated pathways in vascular smooth muscle cells (VC) (F), and downregulated pathways in fibroblasts (FB) (G) in the aortas in ApoE$^{-/-}$/Liver-DKO mice. Statistical analysis (C-G) in ApoE$^{-/-}$ and ApoE$^{-/-}$/Liver-DKO comparison is conducted by the Student's t-test.

Figure S7

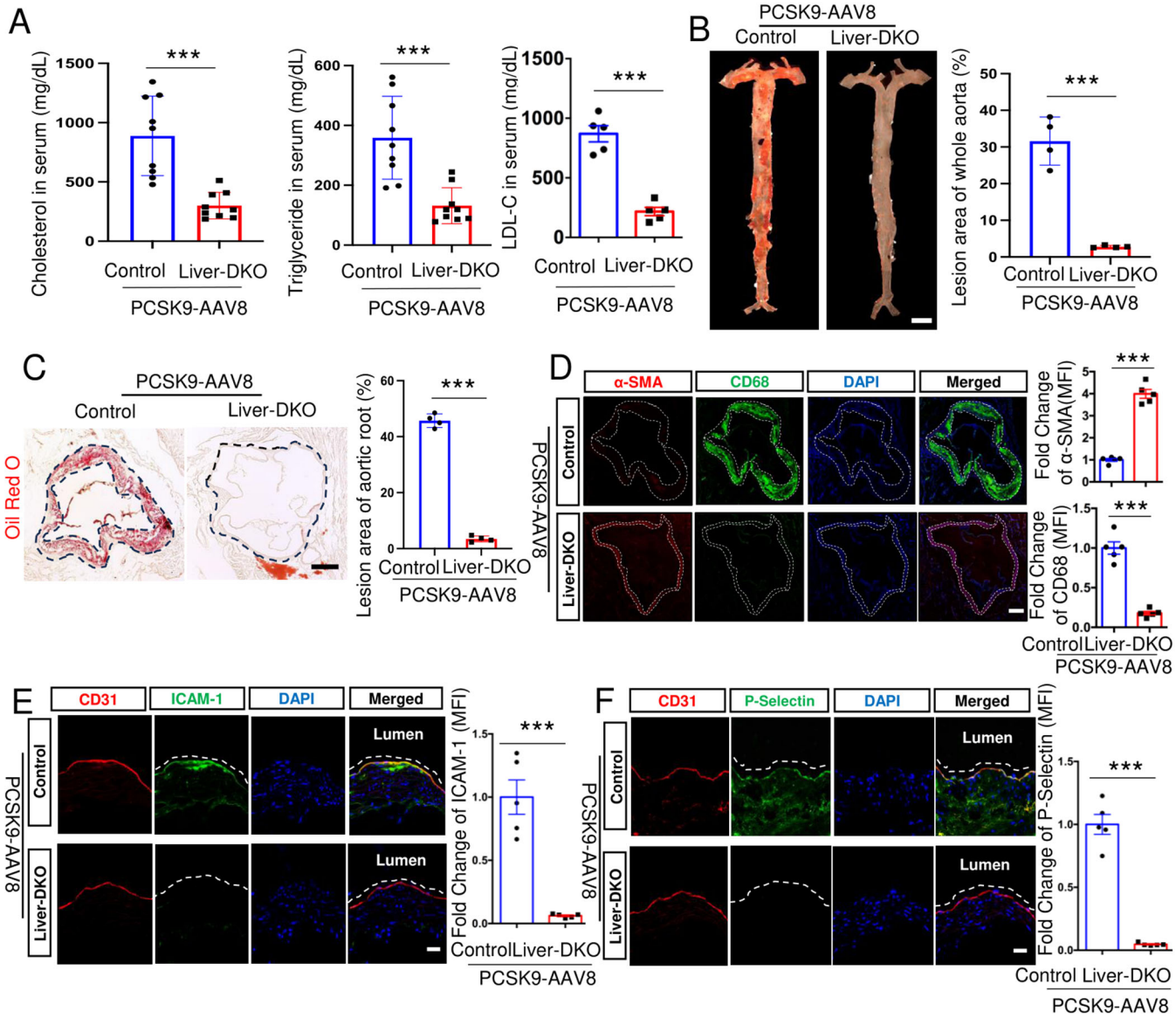
A
Cholesterol in serum (mg/dL)
Triglyceride in serum (mg/dL)
LDL-C in serum (mg/dL)
***
Control
Liver-DKO
PCSK9-AAV8
B
PCSK9-AAV8
Control
Liver-DKO
Lesion area of whole aorta (%)
C
Oil Red O
Lesion area of aortic root (%)
D
α-SMA
CD68
DAPI
Merged
Control
Liver-DKO
Fold Change of α-SMA(MFI)
Fold Change of CD68 (MFI)
E
CD31
ICAM-1
Lumen
Fold Change of ICAM-1 (MFI)
F
P-Selectin
Fold Change of P-Selectin (MFI)

Figure S7: Depletion of epsins in the liver negates the effects of PCSK9 overexpression on atherosclerotic lesion formation, macrophage accumulation, and plasma lipid levels. A: Serum cholesterol, triglyceride, and low-density lipoprotein cholesterol (LDL-C) levels in WD-fed WT and Liver-DKO mice treated with PCSK9-AAV8 after 20 weeks on a WD (n=5-9, p***<0.001). B: *En face* ORO staining of aortas (left) from PCSK9-AAV8 injected WT or Liver-DKO mice fed a WD, and unpaired t-test (right) for the lesion areas (n=4, ***p< 0.001). Scale bar, 5 mm. C: Aortic roots from WD-fed PCSK9-AAV8 injected WT or Liver-DKO mice stained with ORO (left), and unpaired t-test (right) for the lesion areas (n=4, ***p< 0.001). Scale bar, 500 µm. D: Aortic roots from WD-fed PCSK9-AAV8 injected WT or Liver-DKO mice stained with CD68 macrophage marker and α-SMA vascular smooth muscle marker (left), and unpaired t-test (right) for quantification of the mean fluorescence intensity (MFI) (n=5, ***p< 0.001). Scale bar, 200 µm. E-F: IF staining of endothelial cell marker CD31 and endothelial cell adhesion molecules, such as ICAM-1 (E) and P-Selectin (F) (left), in the aortas between WD-fed PCSK9-AAV8 injected WT or Liver-DKO mice. The fold changes of ICAM-1 (MFI) and P-Selectin (MFI) were quantified (right) (n=5, ***p<0.001). Scale bar, 20 µm. Diminished expression of ICAM-1 and P-Selectin proteins in the aortas in WD-fed PCSK9-AAV8-induced Liver-DKO. All statistical analysis (A-F) in PCSK9-AAV8 injected WT and PCSK9-AAV8-induced Liver-DKO comparison is conducted by the Student's t-test.

Figure.S8

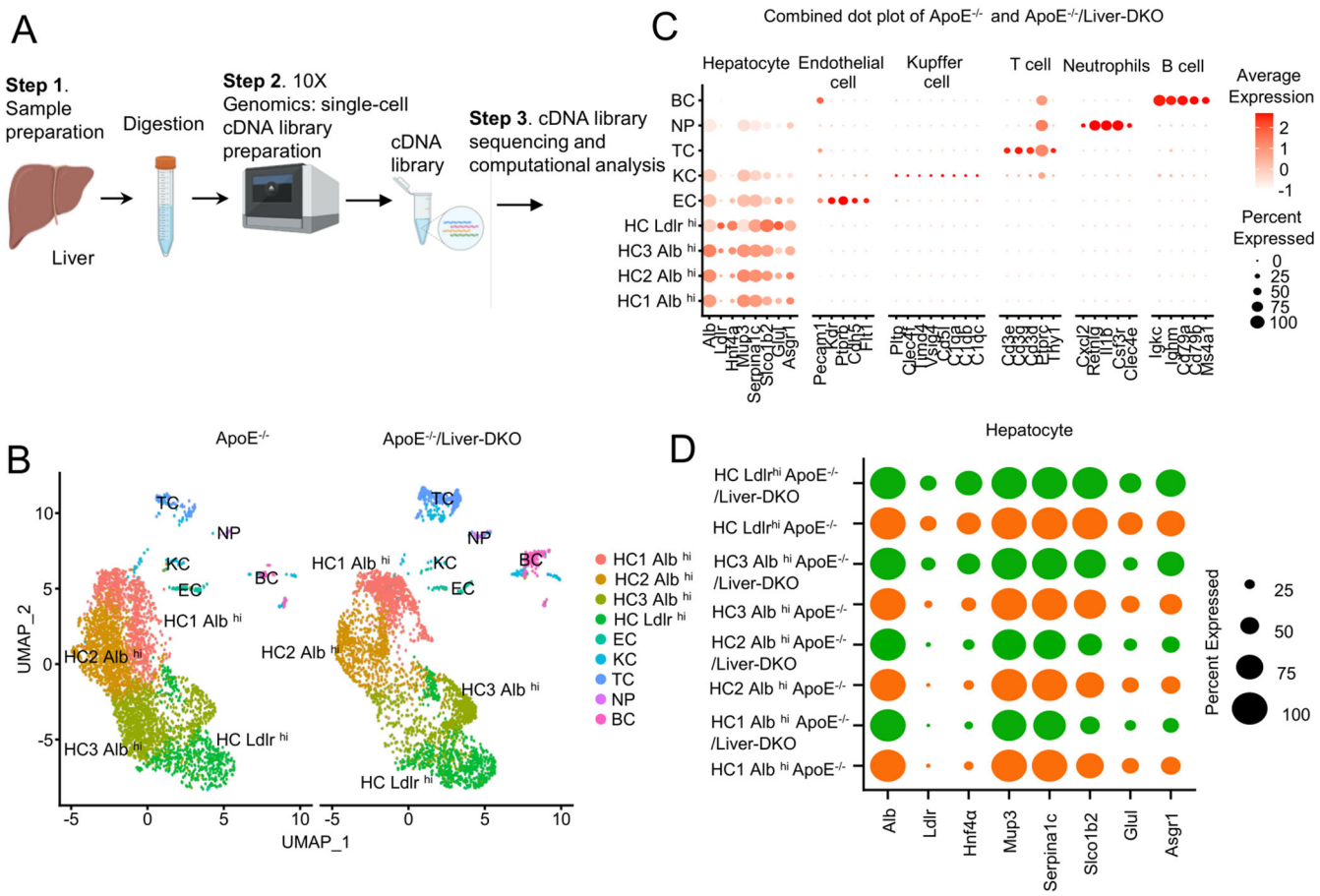
A
Step 1. Sample preparation
Digestion
Step 2. 10X Genomics: single-cell cDNA library preparation
cDNA library
Step 3. cDNA library sequencing and computational analysis
Liver
B
ApoE-/-
ApoE-/-/Liver-DKO
UMAP_2
UMAP_1
TC
NP
KC
EC
BC
HC1 Alb hi
HC2 Alb hi
HC3 Alb hi
HC Ldlr hi
C
Combined dot plot of ApoE-/- and ApoE-/-/Liver-DKO
Hepatocyte
Endothelial cell
Kupffer cell
T cell
Neutrophils
B cell
Average Expression
Percent Expressed
D
Hepatocyte
HC Ldlrhi ApoE-/-/Liver-DKO
HC Ldlrhi ApoE-/-
HC3 Alb hi ApoE-/-/Liver-DKO
HC3 Alb hi ApoE-/-
HC2 Alb hi ApoE-/-/Liver-DKO
HC2 Alb hi ApoE-/-
HC1 Alb hi ApoE-/-/Liver-DKO
HC1 Alb hi ApoE-/-
Percent Expressed

Figure S8: Single-cell RNA-sequencing reveals different hepatocyte subtypes in the livers of ApoE$^{-/-}$ and ApoE$^{-/-}$/Liver-DKO mice. A: Schematic representation of the single-cell RNA-sequencing (scRNA-seq) process performed on the livers of ApoE$^{-/-}$ and ApoE$^{-/-}$/Liver-DKO mice. B: UMAP visualization of whole cell populations in ApoE$^{-/-}$/Liver-DKO and ApoE$^{-/-}$ mice. C: Dot plot illustrates the percentage of cells expressing each gene marker corresponding to specific cell types in ApoE$^{-/-}$/Liver-DKO and ApoE$^{-/-}$ mice. The size of the dots represents the proportion of cells expressing the marker, while the color intensity indicates the expression level of the gene marker in each cell type. D: Dot plot of subclusters of hepatocytes according to the expression of hepatocyte markers, such as Albumin and Ldlr, in ApoE$^{-/-}$/Liver-DKO and ApoE$^{-/-}$ mice. HC1 Alb ^{hi}, HC2 Alb^{hi}, HC3 Alb^{hi}, and HC Ldlr^{hi} hepatocytes are clustered.

Figure S9

A Upregulated differentially expressed genes (DEGs) involved in enhancing lipoprotein clearance and lipogenesis suppression highlighted in the livers in ApoE$^{-/-}$/Liver-DKO (HC)

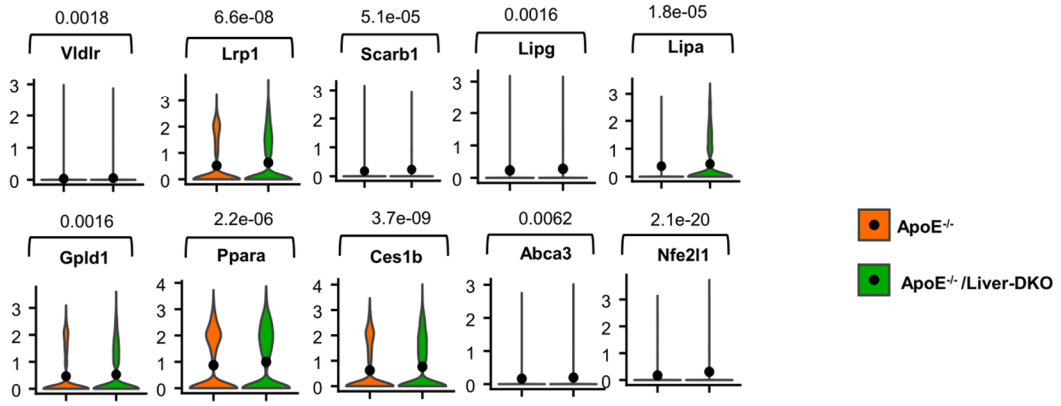

B Downregulated differentially expressed genes (DEGs) involved in plasma lipoprotein remodeling and increasing lipogenesis highlighted in the livers in ApoE$^{-/-}$/Liver-DKO (HC)

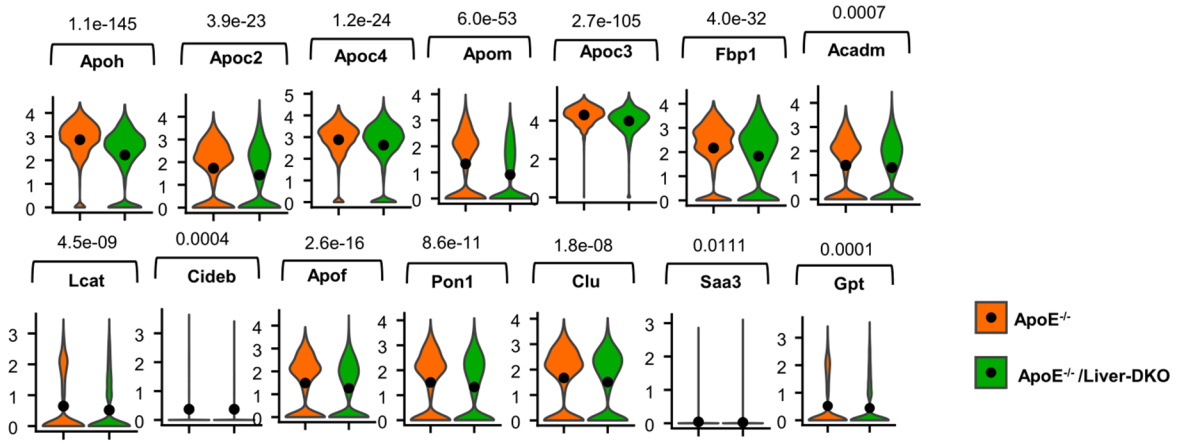

C

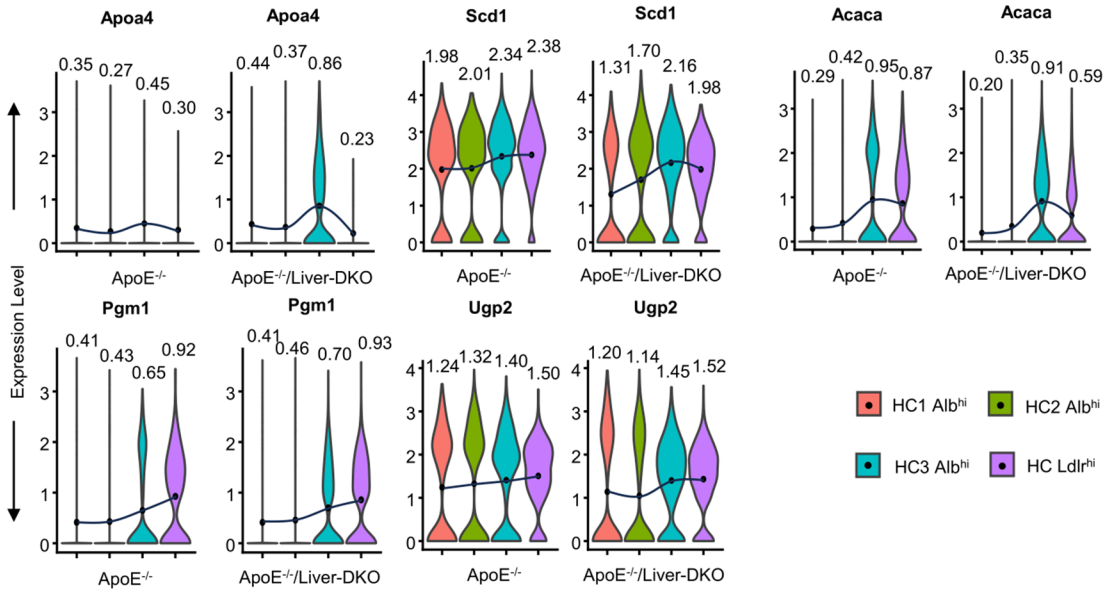

Figure S9: Elevated differentially expression genes (DEGs) that enhance low-density lipoprotein particle clearance, glycogenesis and lipogenesis suppression and diminished DEGs that facilitate hepatic lipogenesis and plasma lipoprotein particle assembly in the livers of ApoE$^{-/-}$/Liver-DKO mice. A: Upregulated DEGs that increase low-density lipoprotein particle clearance and/or reduce lipogenesis in hepatocytes from ApoE$^{-/-}$ /Liver-DKO mice. B: Downregulated DEGs that mediate plasma lipoprotein particle remodeling and hepatic lipogenesis are highlighted in hepatocytes from ApoE$^{-/-}$ /Liver-DKO mice. C: Downregulated expression levels of lipogenic genes, such as *Scd1* and *Acaca*, and upregulated expression of *Apoa4* gene in the hepatocyte subpopulations from ApoE$^{-/-}$/Liver-DKO mice, indicate diminished lipogenesis in the liver of ApoE$^{-/-}$/Liver-DKO mice. Upregulated expression levels of glycogenic genes, such as *Pgm1* and *Ugp2*, in different clustered hepatocytes in the liver of ApoE$^{-/-}$ /Liver-DKO mice reveal elevated glycogenesis in the liver of ApoE$^{-/-}$/Liver-DKO mice. The mean expression levels of genes are highlighted in the violin plots ($p<0.05$). All statistical analysis (A-C) in ApoE$^{-/-}$ and ApoE$^{-/-}$/Liver-DKO comparison is conducted by the Student's t-test.

Figure.S10

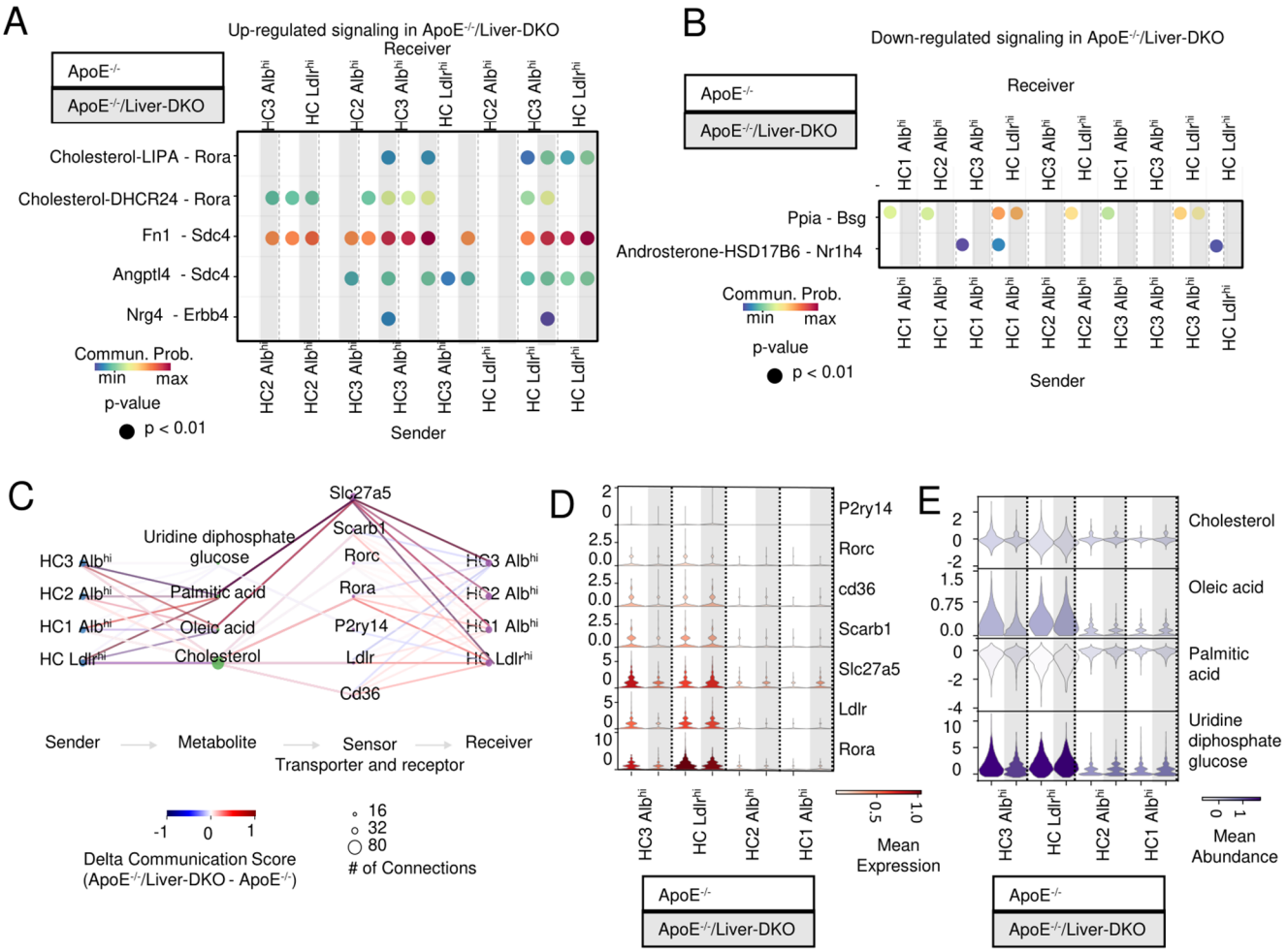
A
Up-regulated signaling in ApoE-/-/Liver-DKO
Receiver
ApoE-/-
ApoE-/-/Liver-DKO
Cholesterol-LIPA - Rora
Cholesterol-DHCR24 - Rora
Fn1 - Sdc4
Angptl4 - Sdc4
Nrg4 - Erbb4
Commun. Prob.
min max
p-value
p < 0.01
Sender
B
Down-regulated signaling in ApoE-/-/Liver-DKO
Receiver
Ppia - Bsg
Androsterone-HSD17B6 - Nr1h4
Commun. Prob.
min max
p-value
p < 0.01
Sender
C
Slc27a5
Scarb1
Rorc
Rora
P2ry14
Ldlr
Cd36
Uridine diphosphate glucose
Palmitic acid
Oleic acid
Cholesterol
HC3 Alb
HC2 Alb
HC1 Alb
HC Ldlr
Sender
Metabolite
Sensor
Receiver
Transporter and receptor
Delta Communication Score (ApoE-/-/Liver-DKO - ApoE-/-)
# of Connections
D
P2ry14
Rorc
cd36
Scarb1
Slc27a5
Ldlr
Rora
Mean Expression
ApoE-/-
ApoE-/-/Liver-DKO
E
Cholesterol
Oleic acid
Palmitic acid
Uridine diphosphate glucose
Mean Abundance
ApoE-/-
ApoE-/-/Liver-DKO

Figure S10: Enhanced LDL particle clearance and LDLR-cholesterol communication elucidate improved LDL-C clearance in ApoE$^{-/-}$/Liver-DKO mice. A-B: Enhanced Rorα-cholesterol and Sdc4-Fn1 communication pathways (A) and diminished Bsg-Ppia and Nr1h4-AndrosteroneHSD17B6 communication pathways (B) in ApoE$^{-/-}$/Liver-DKO hepatocytes. C: Quantitative analysis demonstrates metabolite communication score in ApoE$^{-/-}$/Liver-DKO mice compared with ApoE$^{-/-}$ controls, showing elevated communication score between cholesterol and Ldlr in ApoE$^{-/-}$/Liver-DKO mice. D: Relative receptor expression in ApoE$^{-/-}$/Liver-DKO mice compared with ApoE$^{-/-}$ controls. E: Relative metabolite abundance in ApoE$^{-/-}$/Liver-DKO mice compared with ApoE$^{-/-}$ controls.

Figure.S11

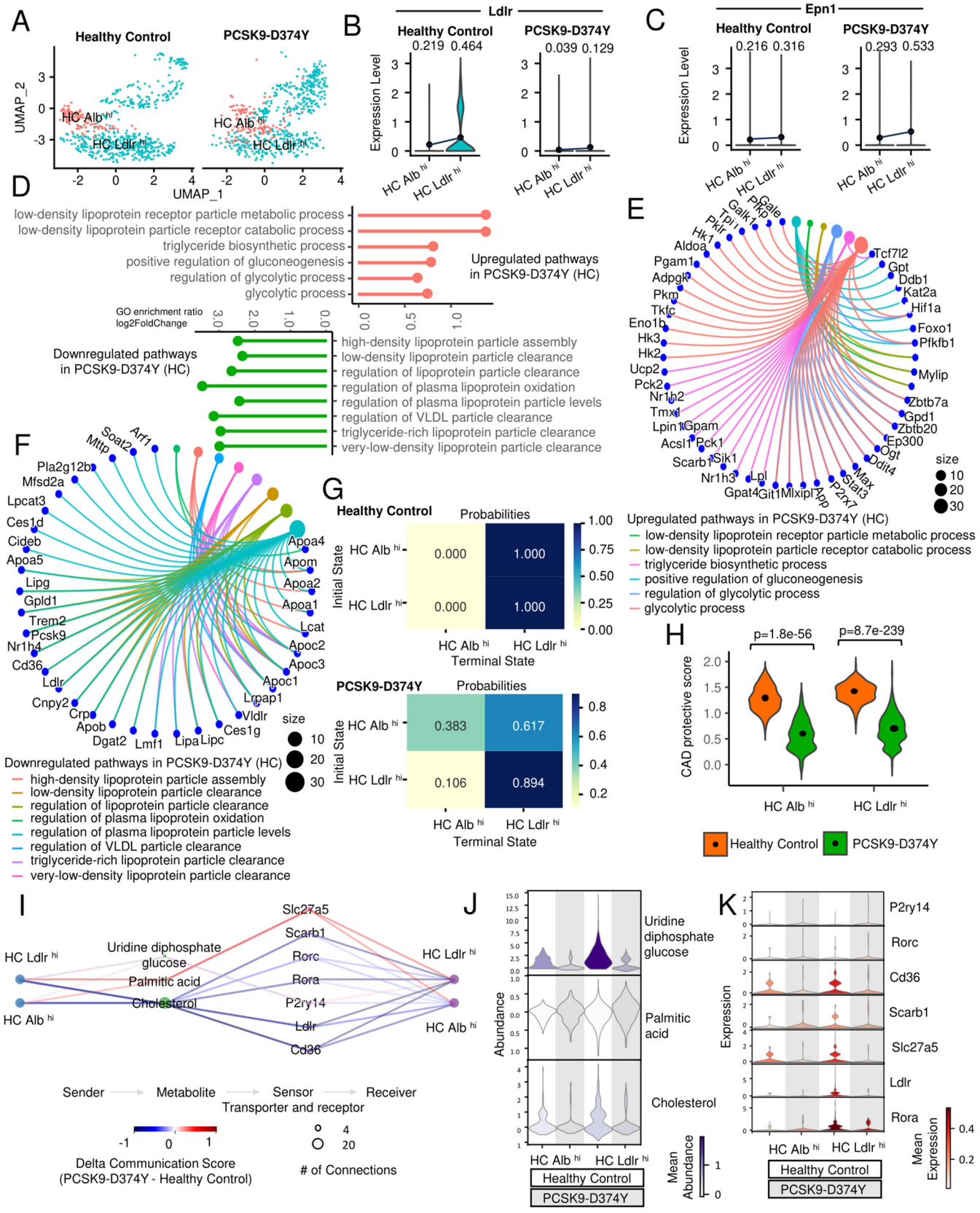
A
Healthy Control
PCSK9-D374Y
UMAP_2
UMAP_1
HC Alb hi
HC Ldlr hi
B
Ldlr
Healthy Control
PCSK9-D374Y
0.219 0.464
0.039 0.129
Expression Level
C
Epn1
Healthy Control
PCSK9-D374Y
0.216 0.316
0.293 0.533
D
low-density lipoprotein receptor particle metabolic process
low-density lipoprotein particle receptor catabolic process
triglyceride biosynthetic process
positive regulation of gluconeogenesis
regulation of glycolytic process
glycolytic process
Upregulated pathways in PCSK9-D374Y (HC)
GO enrichment ratio
log2FoldChange
Downregulated pathways in PCSK9-D374Y (HC)
high-density lipoprotein particle assembly
low-density lipoprotein particle clearance
regulation of lipoprotein particle clearance
regulation of plasma lipoprotein oxidation
regulation of plasma lipoprotein particle levels
regulation of VLDL particle clearance
triglyceride-rich lipoprotein particle clearance
very-low-density lipoprotein particle clearance
E
size
10
20
30
Upregulated pathways in PCSK9-D374Y (HC)
low-density lipoprotein receptor particle metabolic process
low-density lipoprotein particle receptor catabolic process
triglyceride biosynthetic process
positive regulation of gluconeogenesis
regulation of glycolytic process
glycolytic process
F
size
10
20
30
Downregulated pathways in PCSK9-D374Y (HC)
high-density lipoprotein particle assembly
low-density lipoprotein particle clearance
regulation of lipoprotein particle clearance
regulation of plasma lipoprotein oxidation
regulation of plasma lipoprotein particle levels
regulation of VLDL particle clearance
triglyceride-rich lipoprotein particle clearance
very-low-density lipoprotein particle clearance
G
Healthy Control
Probabilities
Initial State
Terminal State
HC Alb hi
HC Ldlr hi
0.000
1.000
0.000
1.000
PCSK9-D374Y
0.383
0.617
0.106
0.894
H
p=1.8e-56
p=8.7e-239
CAD protective score
HC Alb hi
HC Ldlr hi
Healthy Control
PCSK9-D374Y
I
HC Ldlr hi
HC Alb hi
Uridine diphosphate glucose
Palmitic acid
Cholesterol
Slc27a5
Scarb1
Rorc
Rora
P2ry14
Ldlr
Cd36
Sender
Metabolite
Sensor
Receiver
Transporter and receptor
Delta Communication Score
(PCSK9-D374Y - Healthy Control)
# of Connections
J
Uridine diphosphate glucose
Palmitic acid
Cholesterol
Abundance
Mean Abundance
HC Alb hi
HC Ldlr hi
Healthy Control
PCSK9-D374Y
K
P2ry14
Rorc
Cd36
Scarb1
Slc27a5
Ldlr
Rora
Expression
Mean Expression
HC Alb hi
HC Ldlr hi
Healthy Control
PCSK9-D374Y

Figure S11: Single-cell RNA-sequencing reveals diminished expression of LDLR in the livers in PCSK9-D374Y mutated mice. A: UMAP visualization illustrating the heterogeneity of hepatocyte cell populations, showing distinct clustering patterns of hepatocytes in healthy control mice compared with PCSK9-D374Y mutants. B: Downregulated Ldlr expression in hepatocytes in PCSK9-D374Y mutant compared to healthy control. The mean expression levels of Ldlr are highlighted in the violin plots ($p<0.05$). C: Upregulated Epn1 expression in hepatocytes in PCSK9-D374Y mutant compared to healthy control. The mean expression levels of Epn1 are highlighted in the violin plots ($p<0.05$). D: Gene Ontology (GO) analysis showing significantly enriched pathways for upregulated glycolytic process and downregulated LDL particle clearance in PCSK9-D374Y mutants relative to healthy control. E: Circular cnetplot representing upregulated pathways and corresponding genes in PCSK9-D374Y hepatocytes (HC). F: Circular cnetplot illustrating significantly downregulated pathways and corresponding genes in PCSK9-D374Y hepatocytes (HC). G: CellRank analysis illustrating inhibited propensity from Alb^{hi} hepatocytes to $Ldlr^{hi}$ hepatocytes in PCSK9-D374Y mutants compared to healthy controls. H: Coronary artery disease (CAD) protective score comparing PCSK9-D374Y mutant with healthy control, showing a lower CAD protective score in PCSK9-D374Y mutant than healthy control. I: Quantitative analysis demonstrating metabolite communication scores in PCSK9-D374Y-mutated mice compared with healthy controls, showing diminished communication scores between cholesterol and Ldlr in PCSK9-D374Y mutants. J: Relative metabolite expression abundance in PCSK9-D374Y mutant compared to healthy control, showing downregulated expression of uridine diphosphate glucose (UDPG) in PCSK9-D374Y mutant compared to healthy control. K: Relative metabolite receptor expression abundance in PCSK9-D374Y mutant compared with healthy control, revealing diminished expression of Ldlr in PCSK9-D374Y mutant compared to healthy control. Statistical analysis (B, C, H) in Healthy Control and PCSK9-D374Y comparison is conducted by the Student's t-test.

Figure S12

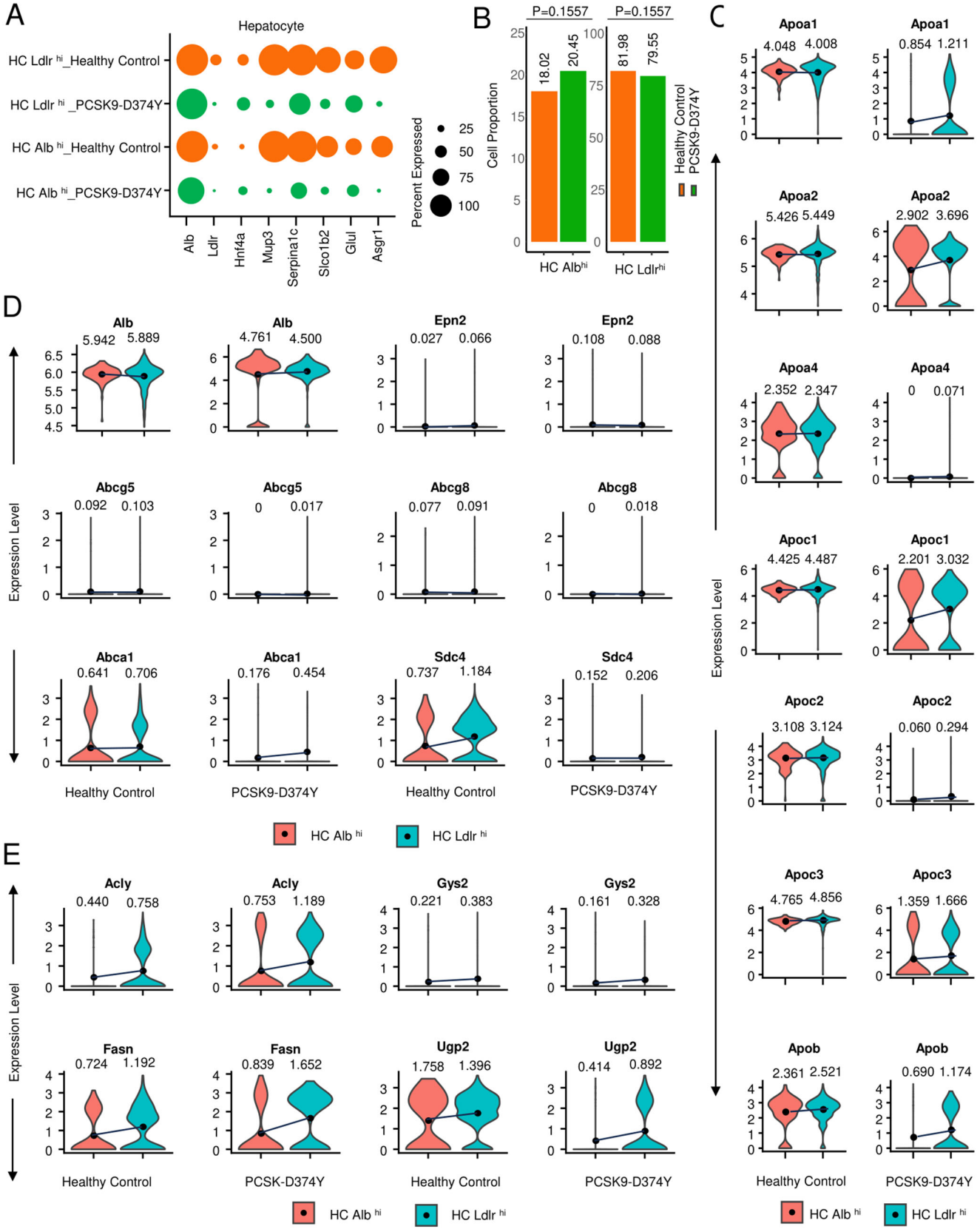
A
Hepatocyte
HC Ldlr hi_Healthy Control
HC Ldlr hi _PCSK9-D374Y
HC Alb hi_Healthy Control
HC Alb hi_PCSK9-D374Y
Alb
Ldlr
Hnf4a
Mup3
Serpina1c
Slco1b2
Glul
Asgr1
Percent Expressed
25
50
75
100
B
P=0.1557
P=0.1557
Cell Proportion
18.02
20.45
81.98
79.55
HC Alb hi
HC Ldlr hi
Healthy Control
PCSK9-D374Y
C
Apoa1
4.048 4.008
Apoa1
0.854 1.211
Apoa2
5.426 5.449
Apoa2
2.902 3.696
Apoa4
2.352 2.347
Apoa4
0 0.071
Apoc1
4.425 4.487
Apoc1
2.201 3.032
Apoc2
3.108 3.124
Apoc2
0.060 0.294
Apoc3
4.765 4.856
Apoc3
1.359 1.666
Apob
2.361 2.521
Apob
0.690 1.174
Expression Level
Healthy Control
PCSK9-D374Y
HC Alb hi
HC Ldlr hi
D
Alb
5.942 5.889
Alb
4.761 4.500
Epn2
0.027 0.066
Epn2
0.108 0.088
Abcg5
0.092 0.103
Abcg5
0 0.017
Abcg8
0.077 0.091
Abcg8
0 0.018
Abca1
0.641 0.706
Abca1
0.176 0.454
Sdc4
0.737 1.184
Sdc4
0.152 0.206
Expression Level
Healthy Control
PCSK9-D374Y
Healthy Control
PCSK9-D374Y
HC Alb hi
HC Ldlr hi
E
Acly
0.440 0.758
Acly
0.753 1.189
Gys2
0.221 0.383
Gys2
0.161 0.328
Fasn
0.724 1.192
Fasn
0.839 1.652
Ugp2
1.758 1.396
Ugp2
0.414 0.892
Expression Level
Healthy Control
PCSK-D374Y
Healthy Control
PCSK9-D374Y
HC Alb hi
HC Ldlr hi

Figure S12: Reduced Ldlr^{hi} hepatocytes in the liver, enhanced gene expression of lipogenesis and diminished expression of genes involved in glycogenesis in PCSK9-D374Y mutant compared with healthy control. A: Dot plot of subclusters of hepatocytes according to the expression of hepatocyte markers, such as Albumin and Ldlr, in healthy control and PCSK9-D374Y mice. B: A relatively low proportion of Ldlr^{hi} hepatocytes in the livers of PCSK9-D374Y mice compared with healthy control. C: Downregulated expression of apolipoprotein genes, such as *Apoa1*, *Apoa2*, *Apoa4*, *Apoc1*, *Apoc2*, *Apoc3* and *Apob*, in different clustered hepatocytes (HC Alb^{hi}, HC Ldlr^{hi}) in PCSK9-D374Y mutant compared with healthy control, indicates diminished low-density lipoprotein clearance in PCSK9-D374Y mutant. The mean expression levels of apolipoprotein genes are highlighted in the violin plots ($p<0.05$). D: Downregulated expression levels of genes involved in cholesterol efflux, such as *Abca1*, *Abcg5*, *Abcg8*, and genes that participate in fatty acid metabolism (*Sdc4*) in the different clustered hepatocytes in the liver from PCSK9-D374Y mutant, indicates the dyslipidemia in PCSK9-D374Y mutant. Diminished expression of *Alb* gene in the different clustered hepatocytes (HC Alb^{hi}, HC Ldlr^{hi}) in the liver in PCSK9-D374Y mutant. Elevated expression of *Epn2* in both Alb^{hi} and Ldlr^{hi} hepatocytes in the liver in PCSK9-D374Y mutant. The mean expression levels of genes are highlighted in the violin plots ($p<0.05$). E: Upregulated expression of genes involved in lipogenesis, such as *Acly* and *Fasn*, in the different clustered hepatocytes in the liver in PCSK9-D374Y mutant. Downregulated expression of genes that participate in glycogenesis, such as *Gys2* and *Ugp2*, in the different clustered hepatocytes in the liver in PCSK9-D374Y mutant. The mean expression levels of genes are highlighted in the violin plots ($p<0.05$). Statistical analysis (B, C, D, E) in Healthy Control and PCSK9-D374Y comparison is conducted by the Student's t-test.

Figure S13

A Upregulated differentially expressed genes (DEGs) involved in the glycolytic process highlighted in the livers in PCSK9-D374Y (HC)

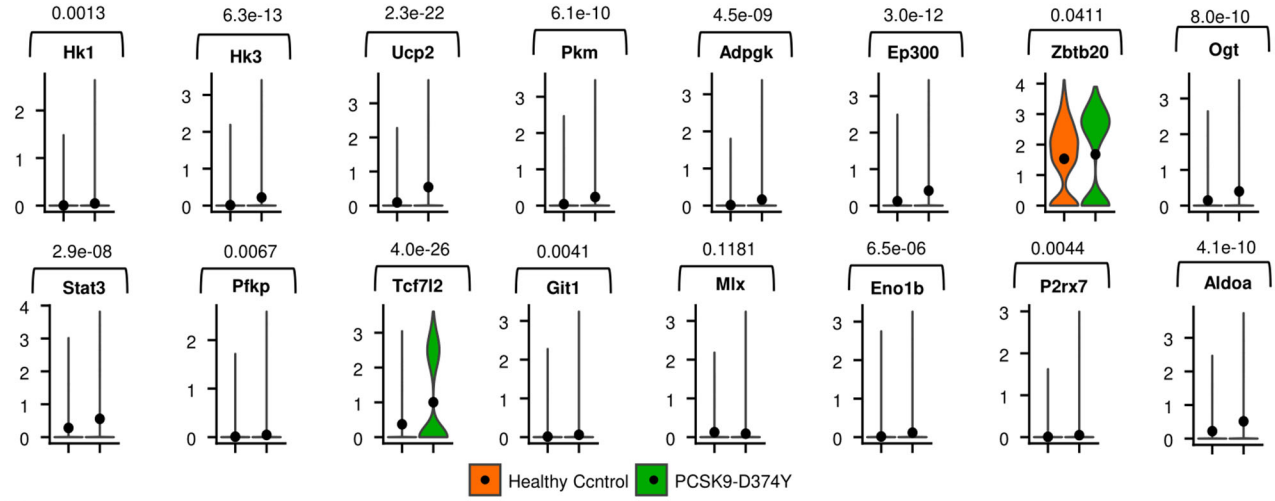

B Downregulated differentially expressed genes (DEGs) involved in low-density lipoprotein particle clearance highlighted in the livers in PCSK9-D374Y (HC)

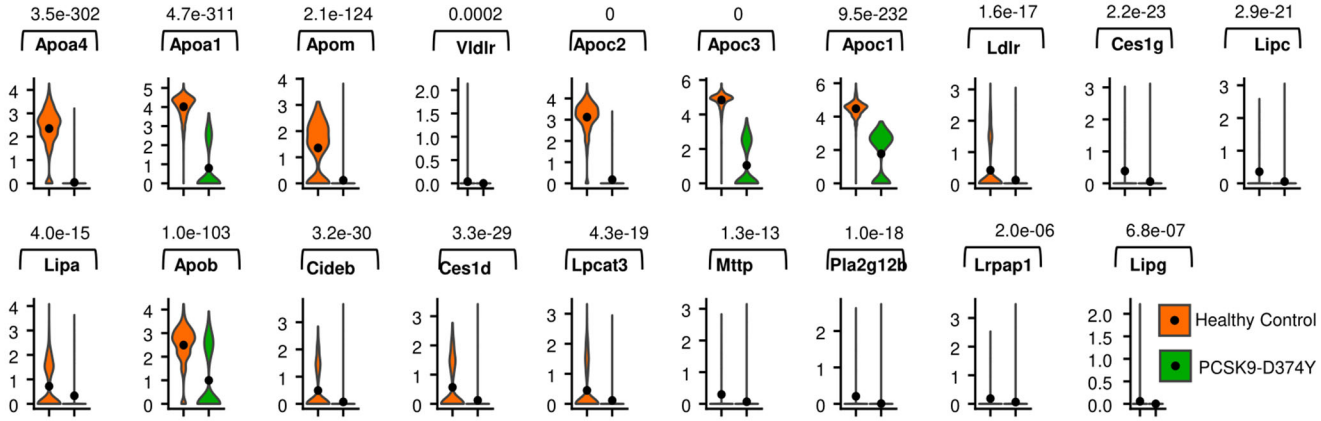

Figure S13: Elevated expression of genes involved in the glycolytic process, and diminished expression of genes responding to low-density lipoprotein particle clearance in PCSK9-D374Y mutant. A-B: Violin plots of differentially expressed genes (DEGs) that are highlighted in cnet plots of either upregulated glycolytic process pathways (A) or downregulated low-density lipoprotein particle clearance pathways (B) in the hepatocytes (HC) in PCSK9-D374Y mutant ($p<0.05$). All statistical analysis (A and B) in Healthy Control and PCSK9-D374Y comparison is conducted by the Student's t-test.

Figure S14

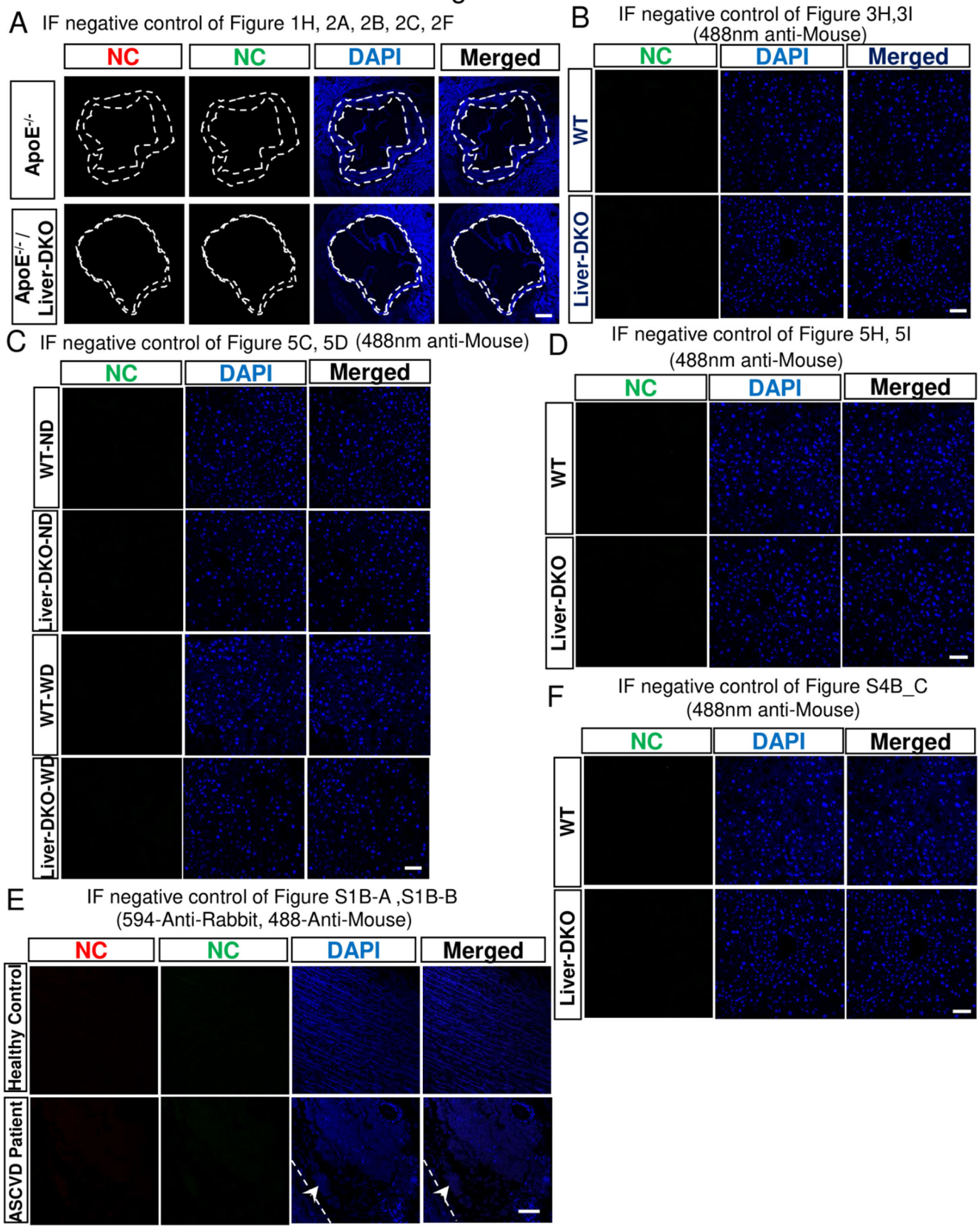
A
IF negative control of Figure 1H, 2A, 2B, 2C, 2F
NC
NC
DAPI
Merged
ApoE-/-
ApoE-/- / Liver-DKO
B
IF negative control of Figure 3H,3I (488nm anti-Mouse)
NC
DAPI
Merged
WT
Liver-DKO
C
IF negative control of Figure 5C, 5D (488nm anti-Mouse)
NC
DAPI
Merged
WT-ND
Liver-DKO-ND
WT-WD
Liver-DKO-WD
D
IF negative control of Figure 5H, 5I (488nm anti-Mouse)
NC
DAPI
Merged
WT
Liver-DKO
E
IF negative control of Figure S1B-A ,S1B-B (594-Anti-Rabbit, 488-Anti-Mouse)
NC
NC
DAPI
Merged
Healthy Control
ASCVD Patient
F
IF negative control of Figure S4B_C (488nm anti-Mouse)
NC
DAPI
Merged
WT
Liver-DKO

Figure S14: Negative controls of immunofluorescence (IF) images without primary antibody staining. A-F: the negative controls of mouse aortas (A) (scale bar, 200 μm), mouse livers (B, C, D, F) (scale bar, 50 μm), and human aortic samples (E) (scale bar, 50 μm), which are annotated as negative controls of either main IF figures or supplemental IF figures, respectively.

Table S1. Genes harboring variants for coronary artery disease (CAD) in ClinVar.

Phenotypes or Disorders	Genes
Abnormality of lipid metabolism	Apoe
Hypocholesterolemia	Apob, Ldlr
Hypobetalipoproteinemia	Apob
Familial hypoalphalipoproteinemia	Apoa1
Hyperalphalipoproteinemia	Apoc1
Hyperapobetalipoproteinemia	Lpl
Hyperlipoproteinemia	Lpl
Familial hypertriglyceridemia	Apoa5
Lysosomal acid lipase deficiency	Lipa
High density lipoprotein cholesterol level quantitative trait locus	Scarb1
Cholesteryl ester storage disease	Lipa
Wolman disease	Lipa
Sitosterolemia	Abcg5, Abcg8

Table S2. Human aorta samples for both coronary artery disease patients and healthy controls

Individual name	Gender	Tissue Source	Normal/ Diseased	Age	Specific Diagnosis	Disease Type
RA06-1040	M	Aorta	Diseased	62-83	Atherosclerosis	Atherosclerotic lesion
RA06-2816	M	Aorta	Diseased	62-83	Atherosclerosis	Atherosclerotic lesion
RA03-0422	F	Aorta	Diseased	62-83	Atherosclerosis	Atherosclerotic plaque with calcifications
RA02-0678	M	Aorta	Diseased	62-83	Atherosclerosis	Mild atherosclerotic change
RA03-0488	M	Aorta	Diseased	62-83	Atherosclerosis	Thrombus and atherosclerotic plaque severe
RA03-0857	F	Aorta	Diseased	62-83	Atherosclerosis	Atherosclerosis with subintimal hemorrhage
RA03-1686	M	Aorta	Normal	<20	Dissection	N/A
R14-0199	M	Aorta	Normal	62-83	Dissection	N/A
RA04-2408	F	Aorta	Normal	62-83	Degeneration	N/A